ANNUAL REPORT

Contract: 03-50-022-67, No. 5
Research Unit: 98
Reporting Period: 1 Ott - 31 Dec 1976
Number of Pages:

DYNAMICS OF NEAR SHORE ICE

Norbert Untersteiner
Professor of Atmospheric Sciences and Geophysics
AIDJEX Project Director

Max D. Coon
AIDJEX Research Coordinator

Division of Marine Resources
University of Washington
Seattle, Washington 98195

CONTENTS

I. SUMMARY

The objectives of NOAA Contract 03-5-022-67, task No. 5, RU 98, can be divided into two groups. First, the objective of the field program was to determine the kinematics of the ice in the Beaufort and Chukchi Seas by satellite tracking of data buoys. In addition to the position, some of these buoys gathered data on ocean currents and barometric pressures. These data are helpful in understanding the causes of the kinematics of the ice. The second objective of this work is to develop an understanding of the dynamics and thermodynamics of nearshore sea ice, which can be converted into computer models to study the forces, motions, and ice state, which will be useful in understanding the behavior of oil spills, sea ice interaction with its environment and manmade objects.

The data from the 20 buoys deployed and analyzed (eight additional buoys have been deployed in March 1977) show that this is a reliable and economical way of determining the trajectories of sea ice. During most of the year oil spilled in the Arctic will be trapped in sea ice and subsequently transported by it. These trajectories being developed by the tracking of data buoys will be the baseline information needed to judge how pollutants delivered to the ice will be transported. From the analysis of this OCS data and the related data from AIDJEX, it appears that during much of the summer the trajectories of ice could be computed from a knowledge of wind conditions only. However, during extended periods in fall, winter and spring the trajectories are influenced by the condition of "the pack ice and its internal stress. Model calculations indicate that ice velocities can be determined from the AIDJEX ice model when high quality wind data are available, together with some buoy positions to provide boundary conditions for the calculations. These calculations allow one to find trajectories when they are affected by other than wind conditions alone. In addition, the model calculations provide information about the stress transmitted through the pack ice. Because it is likely that these ice

stresses and severe ice conditions can be the cause of oil spills, the knowledge of ice conditions and ice stress will be important in determining times and locations for safe operations.

II. INTRODUCTION

A. General nature and scope of the study

The work reported here involves studying the dynamics and thermodynamics of nearshore ice along the north coast of Alaska. To understand the response of the ice requires observation of the kinematics of the ice cover in the Beaufort and Chukchi Seas. To this end we have determined the tracks of numerous data buoys drifting with the ice. In several cases ocean currents were measured also. The trajectories provide baseline information needed to find which pollutants could be advected by the moving ice. To develop an understanding of the causes and limitations of these motions also requires a mathematical model of the dynamic and thermodynamic interaction of sea ice with its environment. Solutions to the model we are using are obtained by numerical integration. We are thus able to simulate observed conditions to study the motion, deformation, stress and state of the ice cover. The buoy drift tracks and satellite imagery allow a direct test of the field of motion predicted by the model. These tests allow material parameters to be chosen and show that the model accurately represents ice response. These results will be useful in understanding the behavior of oil or other pollutants spilled into the ice, the interaction of ice with its environment, and the evaluation of the loads that ice may exert on marine structures.

B. Specific objectives

This work performed can be subdivided into three phases. First, drift data taken by four RAMS and sixteen ADRAMS buoys have been processed and analyzed to provide time series of the motion of each station. Second, the AIDJEX model has

used to simulate conditions observed near the north coast of Alaska during 27 January - 4 February, 1976. The results of the simulation have been analyzed to assess how well the model performed. Third, another set of ADRAMS buoys have been deployed in the Chukchi Sea (6) and near Prudhoe Bay (2) to allow determination of ice motions in these regions beginning about March 1977.

c. Relevance to problems in petroleum development

With the increase in oil drilling and shipping activities that are occurring on the North Slope of Alaska and the Mackenzie Bay area of Canada, we must count on the accidental release of oil or other pollutants into the marine environment. The effect of such a spill is one of the primary concerns of the OCSEAP project. The question that we address relates to the transport of the pollutant from the spill area into other regions of the Arctic and also *to* the forces that the ice may exert on a marine structure. Our efforts represent a multiple attack on the problem of determining the kinematic and kinetic response of the ice-ocean system under *a* variety of conditions. Although the observation of ice and water trajectories provides an important baseline of information, it is inadequate for describing the most probable conditions that might exist during the next five years, or for delineating the range of conditions that are expected to occur, or for identifying the extremes that could occur. Given 50 or so years we could establish such statistics of ice motions. But the problem of petroleum development is urgent. The only data sets for which such statistical measures exist are observations of barometric pressure and local surface winds. Therefore, we turn to modeling to learn how to relate ice drift to the winds, thereby allowing us to consider the necessarily wide variety of conditions. Fortunately, the AIDJEX model has been developed to the point where it can be used to make the analysis. Since the AIDJEX model has been based on the small-scale physical processes that allow the ice cover to deform, we are able to

understand the response of the model and also obtain important information in addition to ice drift--the deformation, ice thickness distribution, and the loads exerted by the ice. Since these forces cannot be measured without full-scale experiments (a prohibitively expensive project), the modeling effort is identified as a necessary part of the plan.

111. CURRENT STATE OF KNOWLEDGE

The state of development of air-droppable data buoys (ADRAMS) indicates that this is a fully developed technology which can be used to obtain data in arctic surroundings. The present data set from these ADRAMS buoys describes the conditions of ice motion in many locations in the Beaufort Sea for one season.

The AIDJEX ice model has been tested and, although further development will be needed, it appears that when sufficiently high-quality data are available, the motion, deformation, thickness distribution and stress in the arctic ice pack can be determined.

IV. STUDY AREA

The study area is the Beaufort and Chukchi Seas.

v. SOURCES, METHODS AND RATIONALE OF DATA COLLECTION

The data for *this* program *was* taken by three types of buoys in the OCS area of the Beaufort and Chukchi Seas.

The meteorological/oceanographic buoy is basically a short (18 ft.) spar buoy which is inserted into the ocean through a 10-inch hole drilled through the ice. Current sensors are suspended from the bottom of the buoy. After installation, the buoys become frozen into the ice but become free-floating in summer. The hulls are 9-inch diameter polyethylene tubes. The designed operating life is in excess of one year.

Data transmission and buoy tracking utilizes the Random Access Measurement System (RAMS) aboard the NIMBUS-6 satellite. Air pressure, air temperature, buoy heading, and ocean current speed and direction at two depths are sampled every three hours. Ten-minute averages are computed for all data. Twenty-four hours of data are contained in memory and transmitted to the satellite. Power is provided by air-cell primary batteries. The communications system is a specifically modified Buoy Transmit Terminal (BTT) developed by the National Data Buoy Office for buoy application.

The air-droppable buoys (ADRAMS) consists of a 22-inch diameter "lexan" sphere mounted on a 15-inch diameter, 12-inch high foam crash pad. The electronics and battery pack form a single unit inside the spere, which is free to rotate in any direction on its Teflon bearings. The electronics module contains a pendulous weight so that regardless of the final resting position of the sphere after deployment, the antenna will be properly oriented.

The system is powered by newly developed inorganic lithium batteries. These batteries allow operation down to the low temperature limit of the system, -50°C.

A rugged BTT (Buoy Transmit Terminal) was developed to survive the shock of an air drop, as well as the low temperatures of the arctic ice pack.

The third type of buoy is an ADRAMS buoy to which a pressure sensor has been added.

VI. RESULTS

Positions of the 20 drifting data buoys have been edited and interpolated to provide daily values. These results are presented in Appendix 1, titled “Measurements of Sea Ice Motion Determined from OCS Data Buoys - October 1975 *to* December 1976,” by A. S. Thorndike and J. Y. Cheung. This appendix discusses the techniques

used to analyze the raw position fixes. In it are also presented in graphical form the trajectory and the time history of velocity (speed and direction) of each station.

All drift station trajectories have been drawn on the Beaufort Sea and Chukchi Sea base maps supplied by the OCSEAP Project Office. These maps were supplied to Dr. Gunter Weller at the Barrow Synthesis Meeting, 7-11 February 1977.

The results of the oceanographic measurements from the RAMS buoys are presented in Appendix 2, titled "AIDJEX Met-Ocean Buoys--Interim Data Report" by M. G. McPhee, L. Mangum and P. Martin.

The results of the model calculations to simulate the nearshore sea ice dynamics are presented in Appendix 3, titled, "Winter Ice Dynamics in the Nearshore Beaufort Sea," by R. S. Pritchard, M. D. Coon, M. G. McPhee and E. Leavitt.

VII. DISCUSSION

The report in Appendix 3 describes the ice conditions and dynamics in the Beaufort Sea from 27 January through 3 February, 1976. We describe observed response of the atmosphere, ice, and ocean. The time period was chosen because the ice conditions and motion are very interesting and because there is a considerable amount of high quality data from the AIDJEX program taken during this period of time. The motion of the ice during this period is greatly influenced by the internal stress of the ice pack. A flaw lead is developed along the north coast of Alaska, extending from Pt. Barrow to the Mackenzie Delta. Shoreward of the flaw lead the ice showed little motion; seaward of this lead the ice moved appreciably. However, even in the regions where there is appreciable motion the amount and direction of it is greatly influenced by the internal stress.

A simulation of the ice dynamics for the nearshore region of the Beaufort Sea has been made using the AIDJEX ice model. During the simulation, part of the data

from AIDJEX stations are used to drive the model and the remaining data are used to verify the quality of the simulation.

There is no motion during the first two days. When motions begin, they are westward. The ice in the western part of the area moves first with the eastern portion responding later. In the nearshore a fast ice region exists that is separated from the moving pack by a discontinuity. These conditions are verified by NOAA satellite imagery and data from the drifting buoys. The model simulates these features accurately, including the velocity discontinuity. This test of the AIDJEX model shows that we understand how ice responds on the large scale *to* driving forces and we are able to describe this relationship at times when the ice stress exerts a dominant influence.

VIII . CONCLUSIONS

The technology for building and deploying air-droppable buoys to obtain information on ice trajectories has been developed to a point where it is reliable and economical. The ice trajectory data determined from the buoy motions will be useful in developing an understanding of the trajectory of pollutants spilled under or into the ice.

Thus far the data indicate that the pack ice outside the shear zone on the North Slope of Alaska would transport the oil to thewest and that if it were far enough north after moving west of Barrow, it would continue to go north and west. Some of this oil could be trapped in the Beaufort Gyre. Depending on degradation rates, this oil could be transported back to Canadian waters. The remaining oil would apparently enter the transpolar drift stream. However, oil remaining near shore could be transported south into the Chukchi Sea. The possibility of oil moving into the Bering Sea cannot be assessed at this point.

The AIDJEX model has been shown to provide a physically realistic simulation of the dynamic response of sea ice to winds during the winter when ice stress is significant. Furthermore, the motion is seen to compare extremely well with observed motions of buoys and manned camps. In the nearshore regions the plasticity model represents fast ice areas. These areas are separated from the moving pack ice by rapid variations or discontinuities. The location of the flaw lead agrees with satellite images. A close look at deformations and stress shows that we may improve some details of the response by changing the yield surface shape and we expect to pursue that work soon.

IX. NEEDS FOR FURTHER STUDY

The program of work that we are reporting on has been shown as crucial to understanding transport of oil by sea ice, and the upper layer of the ocean, also the forces that the ice may exert on marine structures. We have reported results that describe observed ice and ocean trajectories and have shown how a mathematical model (the AIDJEX model) relates ice motion to the wind field. However, because the OCSEAP program has been operational only for two years, the observed motion data in the nearshore Beaufort Sea are limited to the period from October 1975 to December 1976. Similarly, the modeling program, even when all results developed under the AIDJEX/NSF funding are included, covers only a limited range of time and space where simulations have been tested. In this section, we identify the work that must continue if we are to understand the role played by the ice cover in transporting oil and exerting forces. Our aims are to increase geographic coverage, to obtain data at different times of year, to determine season-to-season variations, to simplify the mathematical model, and to balance the levels of sophistication of ice and ocean models in the nearshore environment. It is obvious from the description that the state of the art of understanding ice motion has not advanced

uniformly. This is true because of the far greater complexity under some conditions. On one hand, in the summer conditions when the ice is wind driven (meaning no ice stress, not that ocean currents are negligible) (McPhee, to be published), we are ready to study the range of ice response using historical wind data. We note that the area-wide barometric pressure may control ocean currents. On the other hand, in the rest of the year when the marginal zone is ice covered, no effort has yet begun to understand the important interaction of ice and ocean on smaller scales.

A most alarming question arises as we consider that oil spilled near Reindeer Island at the end of October would be transported to the west of Pt. Barrow by the following June, as shown by buoy trajectories reported in Appendix 1. Since there is a well-known southerly motion in the Chukchi Sea south from Barrow to Cape Lisbourne we must ask, "under what conditions can oil be transported during spring breakup from the Beaufort Sea through the Bering Strait and into the Bering Sea?" The consequence of such transport would be devastating on that rich eco-system. Fortunately, the stage is set to develop *a* mathematical model of the Chukchi Sea that will allow this "breakout" problem to be analyzed. The AIDJEX model has already been shown to be an accurate simulation tool in similar circumstances. And the ongoing data buoy program will provide drift tracks and barometric pressures in this region beginning in March 1977. Therefore, the important question of understanding large-scale motion in the Chukchi Sea can be addressed immediately. In addition to studying the motions observed with presently deployed buoys, satellite imagery will enhance our knowledge of the ice conditions. Analysis of these data will help to determine parameters of the model and to identify which features are most important. As part of this model development, the ocean must be considered as an important component. Ocean current data are available and must be analyzed to find the relative importance of ocean currents.

As a result of current modeling activities and data analysis we have learned that simpler models may be used to relate winds to ice drift under certain conditions. We have shown theoretically that area-wide wind stress averages control drift rates--with the effect of ice stress being small if the area is large enough (Pritchard, to be published). This result is obtained from the AIDJEX model, but the accuracy with which that model represents ice drift lends confidence to the results. Therefore, we feel that the analysis showing limited effect of internal stress on large scales is reasonable. However, the results show that the distance over which this force becomes negligible depends upon the strength of the ice. During the summer when large amounts of open water are present, the average distance can be quite small--even less than 100 km--so that local wind-driven drift can be used to predict motions. However, in winter when the ice is compact and strong, the distances over which air stress must be averaged increase to the order of 1000 km. This means that the average ice motion within such a region can only be defined at distances more than 500 km from shore. Because of this limitation we feel that additional modeling using the entire AIDJEX model in the nearshore region is necessary. However, for the conditions that satisfy this limitation we feel that the currently described simple model should prove useful in correlating winds and ice trajectories. This will allow statistical evaulation of historical wind data and a confident prediction of mean ice trajectories and the range of variations of these trajectories.

The OCS data buoy program that has been in progress during 1975-1977 should be continued to fill several data gaps. The most significant is the need to deploy buoys in the same areas as before to ascertain the year-to-year variability that occurs because of different atmospheric and ice conditions. In addition, buoys deployed in separate local regions, such as the high speed flume off the Alaskan coast of the Chukchi Sea, can answer specific questions. Identification of these

areas and times of year at which deployment should be made also depends on other ongoing programs. The decision should receive strong input from investigators who are testing air, ice and/or ocean models that are being developed.

Finally, more thought must enter the understanding of ice and ocean dynamics on space scales less than 100 km. At times when the ice cover may deform, the response of the ice-ocean system is unknown on these scales. On these scales it is important to understand how loads are transmitted to structures and to learn how to protect these structures from storm surges or from the impinging pack ice. Such a study could allow the barrier islands to be used as protective structures if the manmade structures were properly designed and located. It *is* obvious that final results of this work will be at least several years in coming, but it is desirable to begin a pilot program soon.

X. SUMMARY OF FOURTH QUARTER OPERATIONS

A. Field Activities.

1. Field trip schedule

The field party arrived at NARL on 25 February and worked there until 23 March. NARL aircraft support as follows: Twin Otter, 25 February; C-117, 2 & 7 March; C-lSO, 14, 17 & 22 March. NOAA helicopter support on 9, 17, 18, 19 and 20 March. Chartered Volpar aircraft support from Arctic Guide in Barrow on 13 March.

2. Scientific party

In addition to the aircraft crews the personnel involved in the work were: Pat Martin, who coordinated the various activities; Mel Clarke, who took care of electronic troubleshooting and repair and handled the data processing and analysis; and Dave Bell, who assisted in the assembly and deployment of the buoys.

3. Methods

The buoys mentioned in this report are sampled by the Random Access Measurement System on board NIMBUS-VI. Position and barometric pressure are determined 6-12 times per day.

4* Sample localities

The deployment sites of the buoys are as follows:

Buoy ID	Date	Latitude	Longitude
1064	2 March	67°05'N	168°00'W
1035	2 March	68°50'N	168°59'W
1052	2 March	70°40'N	165°40'W
1617	7 March	72°20'N	166°00'W
1023	13 March	69°40'N	173°40'W
1305	13 March	70°55'N	173°45'W
0632	22 March	70°37'N	147°15'W
1601	22 March	70°50'N	147°00'W

5* Data collected or analyzed

There have been no significant new data collected during the fourth quarter 1976. Data analysis from earlier periods are presented in the appendices.

6. Milestone chart and data submission schedule

a. October 1976 Buoy deployment (in agreement with Gunter Weller, this deployment was held off until March 1977, and has been completed).

b. January 1977. Complete data analysis of buoys in the Beaufort Sea. Data report complete (See Appendix 1).

c. June 1977. Data report completed (See Appendices 1 and 2).

d. June 1977. Model calculation in progress (See Appendix 3).

e. October 1977. Model report (see preliminary report, Appendix 3).

B. Problems encountered/recommended changes.

The principal problem encountered with the spring field work was with arrangements to deploy buoys west of 169° west longitude. Though written notification of the need for such arrangements was given on 3 November, it was apprently impossible for the OCS office to obtain the necessary clearances on time. Therefore, the mission *was* flown by charter aircraft on March 13. This charter flight was conducted by an operator unfamiliar with and unequipped for air navigation techniques necessary for the safe conduct of such flights. These facts were known in advance and were weighed carefully by the participants who decided to accept the risks and proceed with the mission. In the future such operations should be planned well in advance with non-military aircraft.

All the buoys deployed stand a good chance of drifting to positions where the data will no longer be of use to the proposed study, but where recovery of the buoys for reuse will be feasible. Such missions are not a part of the proposed work, but should be considered by OCS.

c. Estimate of funds expended.

As of 28 February 1977, actual expenditures under this contract totaled .$150,609. The estimated obligations for March are anticipated to be approximately $38,239.

APPENDIX 1

MEASUREMENTS OF SEA ICE MOTION DETERMINED FROM OCS DATA BUOYS OCTOBER 1975 TO DECEMBER 1976

by

A. S. Thorndike and J. Y. Cheung
AIDJEX
4059 Roosevelt Way N.E.
Seattle, WA 98105

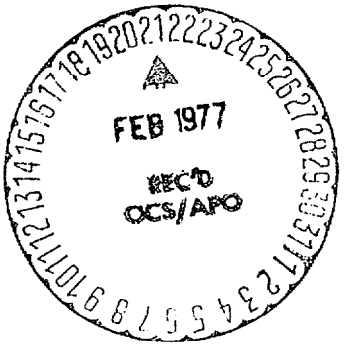

Contents

* DATA NOT COPIED HERE, BUT FULL REPORTS SUBMITTED IN FEBRUARY TO BLM ANCHORAGE & OCSEAP DATA BASE.

MEASUREMENTS OF SEA ICE MOTION DETERMINED FROM OCS DATA BUOYS OCTOBER 1975 TO DECEMBER 1976

by

A. S. Thorndike and J. Y. Cheung
AIDJEX

ABSTRACT

During 1975 and 1976 measurements of sea ice motion were made as part of AIDJEX, and the Outer Continental Shelf project. The raw data from the 20 platforms deployed in the continental shelf region have been edited and interpolated for presentation in this report.

1. INTRODUCTION

The objective of the Arctic Ice Dynamics Joint Experiment, *as set* forth in its most general statement, was to reach an understanding of the dynamic and thermodynamic interaction between the ice cover and its environment[Maykut et *al., 1972].* One component of the experiment was an array of drifting stations at which frequent measurements of position were made. For the present report those measurements have been edited and interpolated using Kalman smoothing techniques to give position and. velocity estimates at evenly spaced time points. (The raw measurements themselves are not reported here, but are available through the AIDJEX Data Bank.)

This report is limited to buoys deployed in the continental shelf region. For data from other platforms which were tracked during AIDJEX, we refer the reader to Thorndike and Cheung [1977].

2. THE RAN MEASUREMENTS

The measurements *were* made with the Random Access Measurement System (RAMS), which uses the techniques of Doppler Satellite navigation. The

raw measurement is the frequency of a signal transmitted from the ice station to the satellite. The measured frequency is affected by a Doppler shift related to the rate of change in distance between the satellite and the ice station, which is itself related to the unknown ice coordinates and the known satellite orbit. During each satellite orbit several frequency measurements were made and from them an over-determined solution was found for the unknown coordinates. The Doppler counts were made for discrete l-second bursts transmitted from the buoy each minute. Typically, 20 measurements per pass were collected, stored, and transmitted to a receiving station on the ground. Fix calculations were done at NASA and the results passed to AIDJEX on magnetic tape. The best of these buoys got about 15 fixes per day. A few RAMS buoys operated for only part of each day and had a much lower data rate, approximately 4 fixes per day. (See Brown and Kerut [1976], Burke and Buck [1975], and Martin and Gillespie [1976], for details of the hardware systems.)

3.. PREPROCESSING

The first step in preprocessing was to reduce each position fix to an abbreviated format containing 80 characters which summarize the fix. Only the fix itself, the time of the fix, and several parameters relating to the quality of the fix were included in the summary format. Raw data--the Doppler counts, say--are contained only in the original data tapes. The abbreviated format is summarized in Appendix 1.

The raw data sequence from RAMS platforms is seriously contaminated with bad fixes. A glance at *a* plot of the raw time series (Figure 1) illustrates the problem. Because outlying fixes have a deleterious effect on the Kalman filtering results, an attempt was made to remove them during preprocessing. The algorithm employed compares each fix latitude with the median of the latitude of the 10 fixes preceding and the 10 fixes following it. When the differences exceeded a preset tolerance, the fix was eliminated, The algorithm was applied twice, with a smaller tolerance the second time. The same procedure was then applied for longitude. The tolerances used were 20 km and 5 km for buoys with a high data rate anti 40 km and 10 km for buoys with a low data rate.

Data were filtered in 20-day blocks. Some overlap was provided to give continuity at the end points of each block, so actually the raw data were prepared for filtering in overlapping 26-day chunks, and are avai.l-able from the AIDJEX Data Bank in that form.

Visual checks were an important part of the procedure. Plots of the data points were produced before and after preprocessing. At times it seemed from the plots that we were not detecting certain bad fixes, or that we were throwing out good ones, and it was necessary to adjust the tolerance levels. This *was* especially true for buoys with a low data rate. The final data plots (Figure 2) provided assurance that the data were ready for filtering.

4. KALMAN SMOOTHING

In the smoothing scheme used here an assumption is made regarding the motion of the ice. If the state of the ice at time t_n is represented by a vector X_n, containing, say, the position, velocity, and acceleration of each point in the ice pack, then the state at some future time is assumed to be partially determined by X_n:

$$X_{n+1} = \Phi X_n + \Gamma W_{n+1} \tag{1}$$

where Φ and Γ are known from the physics of the situation, and W_{n+1} represents an unknown random perturbation. In Kalman's formulation, which we follow, the random effects are assumed to be Gaussian and *white:*

$$\text{co\'}\ (W_n W_m) = \begin{cases} Q \text{ if } n = m, \text{ and} \\ 0 \text{ if } n \neq m. \end{cases} \tag{2}$$

We have chosen $Q = 100\ \text{m}^2\,\text{hr}^{-6}$ [Thorndike, 1973]. Qualitatively choosing a small value of Q is equivalent to assuming that the ice moves in a completely predetermined way. (See from equations 1 and 2 that $Q = 0$ would imply that $X_{n+1} = \Phi X_n$.) A large value of Q corresponds to assuming that

the ice experiences large sudden changes in its acceleration. For this problem we have defined $\Delta = t_{n+1} - t_n$ and

$$X = \begin{pmatrix} x \text{ position} \\ x \text{ velocity} \\ x \text{ acceleration} \end{pmatrix}, \quad \Phi = \begin{pmatrix} 1 & \Delta & \Delta^2/2 \\ 0 & 1 & \Delta \\ 0 & 0 & 1 \end{pmatrix}, \tag{3}$$

and

$$\Gamma = \begin{pmatrix} \Delta^3/6 \\ \Delta^2/2 \\ \Delta \end{pmatrix} * \tag{4}$$

An identical equation can be written for the y-coordinates. The two coordinates are treated independently. Treating the stations one at a time in this way is equivalent to assuming that different stations experience *independent* random perturbations in acceleration. We know that this is "not true [see Thorndike, 1974, p. 114, Fig. 5]. But since an objective of the program was to study the differences in motion between the stations, we chose not to build into the data processing scheme any physical coupling between the stations. Otherwise, interpretation of, say, strain estimates would be clouded by an underlying assumption that one station knew what the other was doing.

The variance Q affects the high frequency response of the processing scheme.. Figure 3 shows the approximate response. Fluctuation with periods of less than about two days cannot be resolved with these measurements and this Processing scheme.

Each measurement, Z_n, is related to X by a matrix H which picks out of X the position element:

$$Z_n = H X_n + V_n$$

where V_n is a measurement error with assumed variance R.

The structure of R reflects our understanding of the measurement process. In the equations (Appendix 2) which give the smoothed estimates of X, data points are weighted according to the measurement error variance assigned in R.

Important for our application of the RAMS system is the presence of several RAMS platforms at fixed sites on land. For each satellite pass it is possible to determine the error at the fixed reference platforms and"' to apply a correction to the fixes obtained from the same pass by our moving buoys.

The algorithm used finds the fix error in the direction of satellite motion at the reference point and subtracts that error in the direction of the satellite motion at the buoy. The application of this translocation principle improves the accuracy of the RAMS fixes and allows us to process data from the RAMS buoys one buoy at a time. A constant value of R = $(2\ \text{km})^2$ has been used in processing the RAMS data.

The general smoothing problem is to estimate X at time t_n using the entire set of observations $\{Z_i\}$ $i = 1,\ldots,M$, and to give the error variance of that estimate. The solution equations, due to Kalman, are reproduced in Appendix 2. Tables and plots which follow summarize the results of our calculations. Typical estimation error variances for each quantity are summarized in Table 1. When measurements were scarce the variances increased, of course. Figure 4 shows the time periods for which the variance exceecled *a* nominal limit, at which times the results must not be taken too seriously.

ACKNOWLEDGMENT S

The authors want to emphasize that the work reported on here, for which they were responsible, is only a part of the total effort involved in this buoy program. Pat Martin had the responsibility for monitoring the design and production of the buoys and for their deployment. Max Coon and others from the AIDJEX modeling group made decisions about *where* the buoys were to be deployed. Gillespie wrote the software to read the data from the NASA tapes and got them into a form suitable for our processing.

Finally Bill Seechuk at NASA provided important support and was remarkably patient in dealing with our many requests for near real time data.

The work was supported by the National Science Foundation Grant Arctic Sea Ice Study number OPF76-10801, and by the National Oceanographic and Atmospheric Administration Outer Continental Shelf contract 03-5-022-67 , entitled Near Shore Ice.

REFERENCES

Brown, W. P., and E. G. Kerut. 1976. Air droppable RAMS (ADRAMS) buoy. In *Ocean* 76, *Proceedings of the* 1376 *International Conference on. Engineering in the Ocean Environment.* IEEE Publ. No. *76* CHO 1118-9 OEC, section 14, D1-6.

Burke, S. P., and B. M. Buck. 1975. The SYNRAMS ice *station.* In *Ocean 75, Proceedings of the 1975 IEEE International* Conference on *Engineering i-n the Ocean Environment.* IEEE Publ. No. 75 995-1 OEC, pp. 413-417.

Martin, P., and C. R. Gillespie. 1976. Arctic odyssey--five years of data buoys in AIDJEX. In *Proceedings of the Symposium on Meteorological Observations from* ***Spin?,*** *Their Contribution* ***to*** *the First GARP Global Experiment,* National Center for Atmospheric Research, Boulder, CO, pp. 328-334.

Maykut, G. A. , A. S. Thorndike, and N. Untersteiner. AIDJEX scientific plan. *AIDJEX Bulletin,* 15, 67 pp.

Meditch, J. S. 1969. *Stochastic Optimal Linear Estimation and Control.* McGraw-Hill, New York.

Thorndike, A. S, 1973. An integrated system for measuring sea ice motions. In *Ocean* 73, *Proceedings of the* 1973 *IEEE International Conference on Engineering in the Ocean Environment.* IEEE Publ. No. 73 CHO 774-O OEC, pp. 490-499.

Thorndike, A. S. 1974. Strain calculations using AIDJEX 1972 position data. *AIDJEX Bulletin,* 24, 107-129.

Thorndike, A. S., and J. Y. Cheung. 1977. AIDJEX measurements of sea ice motion, 11 April 1975 to 14 Nay 1976. *AIDJEX Bulletin,* 3 5 , 1-149.

APPENDIX 2

AIDJEX MET-OCEAN BUOYS

Interim Data Report

by

M. McPhee
L. Mangum
P. Martin
AIDJEX Office

I. INTRODUCTION

This document presents current measurements made from ice- bound drifting data buoys in the Arctic Ocean. It is intended as a "first-look" compilation of the data; interpretation and conclusions have been kept to a minimum.

Four meteorological/oceanographic (M/O) data buoys were deployed in November, 1975, at locations chosen along the 1000 m isobath in the continental shelf break north of Alaska and Western Canada. It was anticipated that the buoys, each of which was equipped to measure relative current: speed and direction at 2 m and 30 m belowthe ice, would add to our meager knowledge of how near-surface currents in the most intense part of the anticyclonic Pacific Gyre interact with the continental shelf regime. In addition, the boundary layer structure inferred from the measured currents could be compared with similar measurements made at manned ice stations to estimate momentum exchange between the ice and upper ocean within the shear zone.

II. BUOY PERFORMANCE AND RAW DATA

A brief summary of M/O buoy performance is listed in Table 1, In conformance with AIDJEX notation we have listed time in days from the beginning of calendar 1975, e.g., day 366 is 1. January 1976.

Environmental data were collected from $1/0 1 for 145 days and frcm M/O 4 for 332 days as shown. The other two buoys furnished no oceanographic data.

Each buoy consists of a tube 6 m long and 0,3 m in diameter frozen into a hole drilled through the ice. Savonius-rotor current meters with current following vanes (manufactured by Hydro-products) are attached to a suspended pipe mast fixed rigidly to the buoy chassis. The magnetic bearing of a reference azimuth for the buoy is sensed with a compass housed in the tube. Samples of current speed and direction, magnetic azimuth, and meteorological parameters are taken every three hours. The current speed is averaged for 10 minutes, while direction samples are instantaneous

in order to avoid 0°-360° crossover ambiguity. The buoy's memory holds a full day's samples, which are repeatedly transmitted so that when the Nimbus VI weather satellite is within view, the data are received and stored for later playback to a tracking station. NASA performs basic processing of the raw data and furnishes the results to our office on magnetic tape. Geographic positions are computed by NASA based on Doppler frequency measurements made by the spacecraft. The position data are further enhanced by processing developed at AIDJEX (see Thorndike and Cheung, 1977).

The buoys were built by the Applied Physics Laboratory, University of Washington, under contract for NOAA Environmental Research Laboratory, monitored by the NOAA Data Buoy Office and AIDJEX. Deployment was from helicopter and required approximately two hours on the ice per installation.

Figures 1 and 2 (adapted from Thorndike and Cheung, 1977) show drift tracks for the two buoys from which oceanographic data were received. M/O 1 left the air on day 452, but began transmitting again about two months later. Environmental data during the later period appear to be garbled; this was unfortunate since buoy drift in the vicinity of Barrow Canyon is often anomalously swift and it would have been particularly useful to have surface current measurements there.

Figures 3 and 4 show the magnetic azimuth data required for defining true current directions. In order to get the actual magnetic azimuth, the raw data shown require a correction, unique to each buoy, that is dependent on the compass direction and the local horizontal field strength. Correction curves were obtained by extrapolating from errors measured at Seattle and Barrow where the field strength is known.

Raw data from the current meter sensors are received as integer counts and converted to dimensional units using calibration data supplied by the designer. Figures 5 through 8 show calibrated data samples (8 per day) as they were received.

The current bearing shown is the apparent direction of the current relative to the buoy azimuth. The? scatter is large but not unexpected, particularly since no provision for vector averaging was made. From previous work under ice we expect turbulent eddies with time scales of from 5 to 10 minutes and these would introduce large variations in directions sampled instantaneously even with steady drift. This would be especially true for the 2 m measurements. Another source for large variations on scales of a few hours is inertial oscillation of the ice cover and upper ocean. We found at the manned stations that it was not uncommon for the apparent direction at 30 m to swing full circle in one inertial period. Thus the extreme scatter exhibited in Figures 7 and 8 for the 30 m direction is expected. It does not show up in the 2 m direction because the water at that level is oscillating in phase with ice. An interesting aspect of these oscillations is that their onset is apparently about two months earlier than was observed at the mannedcamps the previous summer. Presumably the oscillations are damped when the ice is thick, but occur freely when the ice can no longer support internal stress gradients.

111. PROCESSED DATA

For useful results it was clear that some sort of filtering of the current data was required, and as a first attempt we applied a "cosine bell" running mean, i.e., each smooched sample was calculated by averaging the corresponding unsoothed sample with the 1.2 preceeding and succeeding samples, all with the proper cosine weighting. The effect in the frequency domain is a low-pass filter with little energy content at periods shorter than 12 hours. The filter attenuates most of the energy at the inertial period, which is 12.6 hours at 72°N.

The filter was applied to the zonal and meridional. velocity components. These were obtained by subtracting the corrected magnetic, heading from the current direction, then adding the magnetic declination at the buoys' positions. Also, from

intercompari son between the ice motion and the 2 m and 30 m currents, we belie've that the 30 m sensor of M/O 1 and both sensors of M/O 2 were installed backward. so that. 180° is added to each of those bearings. It should be pointed out that inst allat ion requires coupling current meters to the pipe in the field and the design permitted a 180° misalignment.

Results of the calculations described above are shown in Figures 9 through 12. We have reconverted the smooth components to speed and bearing and have shown them compared to the ice speed and bearing as determined from the smoothed satellite data. The reference frame is chosen such that the actual current at either level is obtained from the vector addition of the ice velocity and the measured current. In other words, if the water at 30 m were still, the 30 m current would (ideally) have the same speedasthe ice and its bearing would be 180° out of phase with that of the ice.

With this in mind, the speed plots show many of the characteristics we have seen at the manned camp, i.e., the 30 m speed is usually close to and shows many of the same fluctuations as the ice speed. The 2 m speed also follows, but at a reduced magnitude, indicating that the water at 2 m is following the ice (causing reduced shear). An interesting event is apparent beginning about day 360 in the 30 m speed at M/O 1 (Figure 9). Note that the current speed is sustained at a level appreciably higher than the ice speed for several days. A similar event occurs at buoy M/O 4 about 1.0 days later. It is possible to conjecture that the events are from the same baroclinic disturbance which is propagating eastward at about 40 cm/s (the buoys are approximately 400 km apart). There is also a sustained current during February, March, and April 1976 at M/O 4 in the absence of much ice drift. It apparently sets west as would be expected in the southern part of the. gyre.

The intent of this report has not been an exhaustive analysis of the buoy data, and much remains to be done. In view of the fact that the buoys pioneered in having current measuring capability, the results are encouraging. We have had trouble interpreting the directional measurements and consider some of the directional data suspect; however, this may be more due to prejudice from previous ice station experience rather than the actual evidence. We do point out that when a towing velocity is provided by the ice, the directional measurement requires higher precision to determine the actual current direction to the same accuracy than if the current meter were fixed. This is something that should be considered in design of future buoys. It also seems well within present technical capability to provide vector averaging electronics. A sensitive temperature sensor seems feasible and would be useful, particularly during the summer months, to indicate the amount of stratification.

IV. REFERENCES

Thorndike, A.S. and J. Y. Cheung. 1977. Measurements of sea ice motion determined from OCS data buoys - October 1975 to December 1976. Appendix 1, Annual Report, "Dynamics of Near Shore Ice."

TABLE 1

MET-OCEAN BUOY PERFORMANCE

M/O Buoy	RAMS Platform	Deployed		Position Data	Environmental Data	Remarks
		Position	Date			
1	*1416/1420*	71°32'N 147°W	2 Nov 75 (306)	307-4.52 519-697	307-452	Env. data poor quality after 430
2	1451/1467	71°20'N 149°W	2 Nov 75 (306)	307-608	none	Position data only
3	1143/1175	73°44'N 130°W	5 Nov 75 (309)	none	none	Failed soon after deployment
4	1245/1273	71°N 135°W	3 Nov 75 (307)	308-640	308-640	

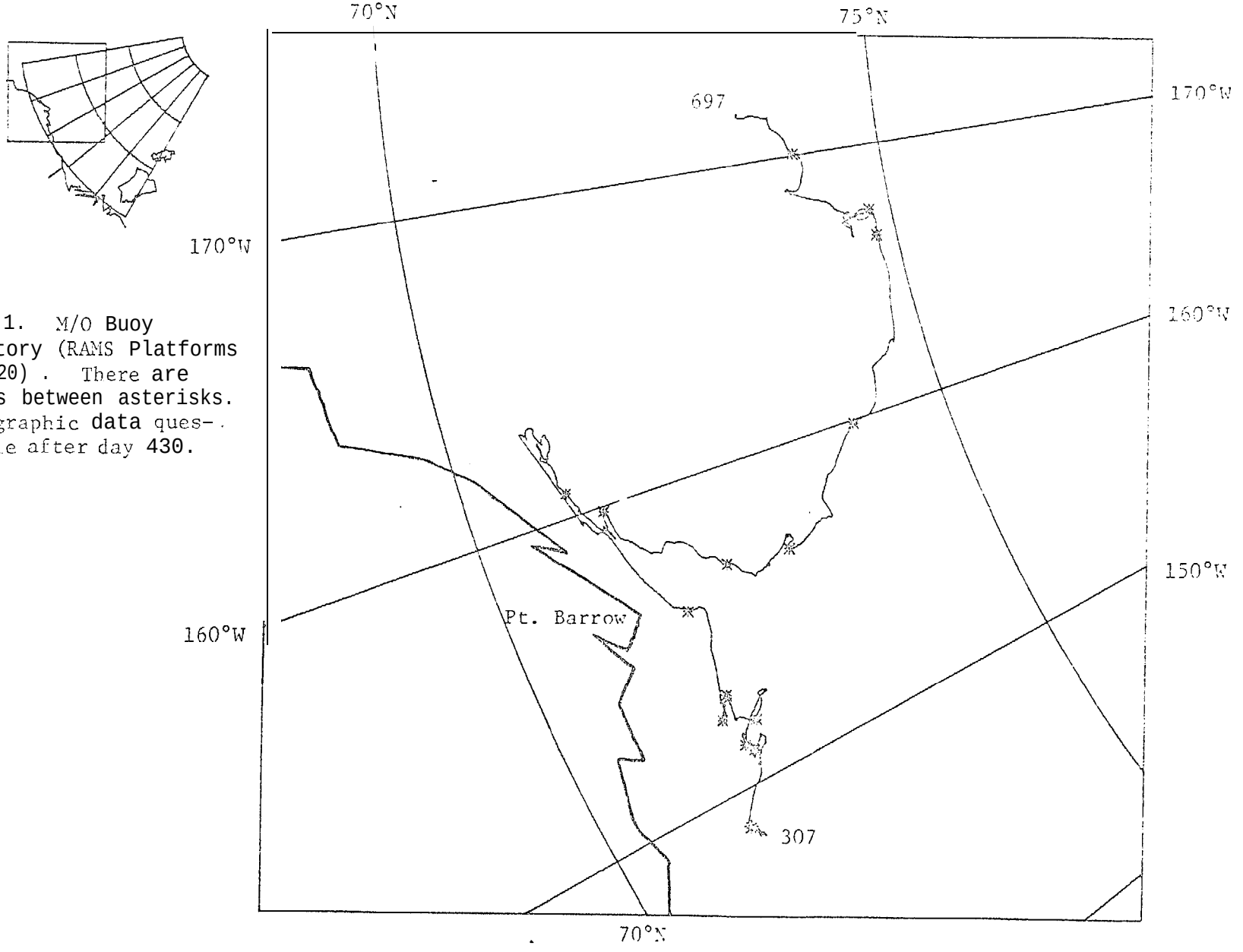

Figure 1. M/O Buoy Trajectory (RAMS Platforms 1416/1420). There are 20 days between asterisks. Oceanographic data questionable after day 430.

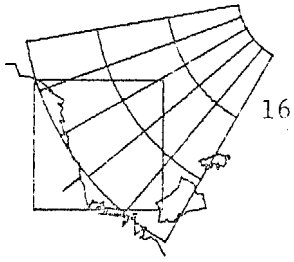

Figure 2. M/O Buoy Trajectory (RAMS Platform 1245/1273).

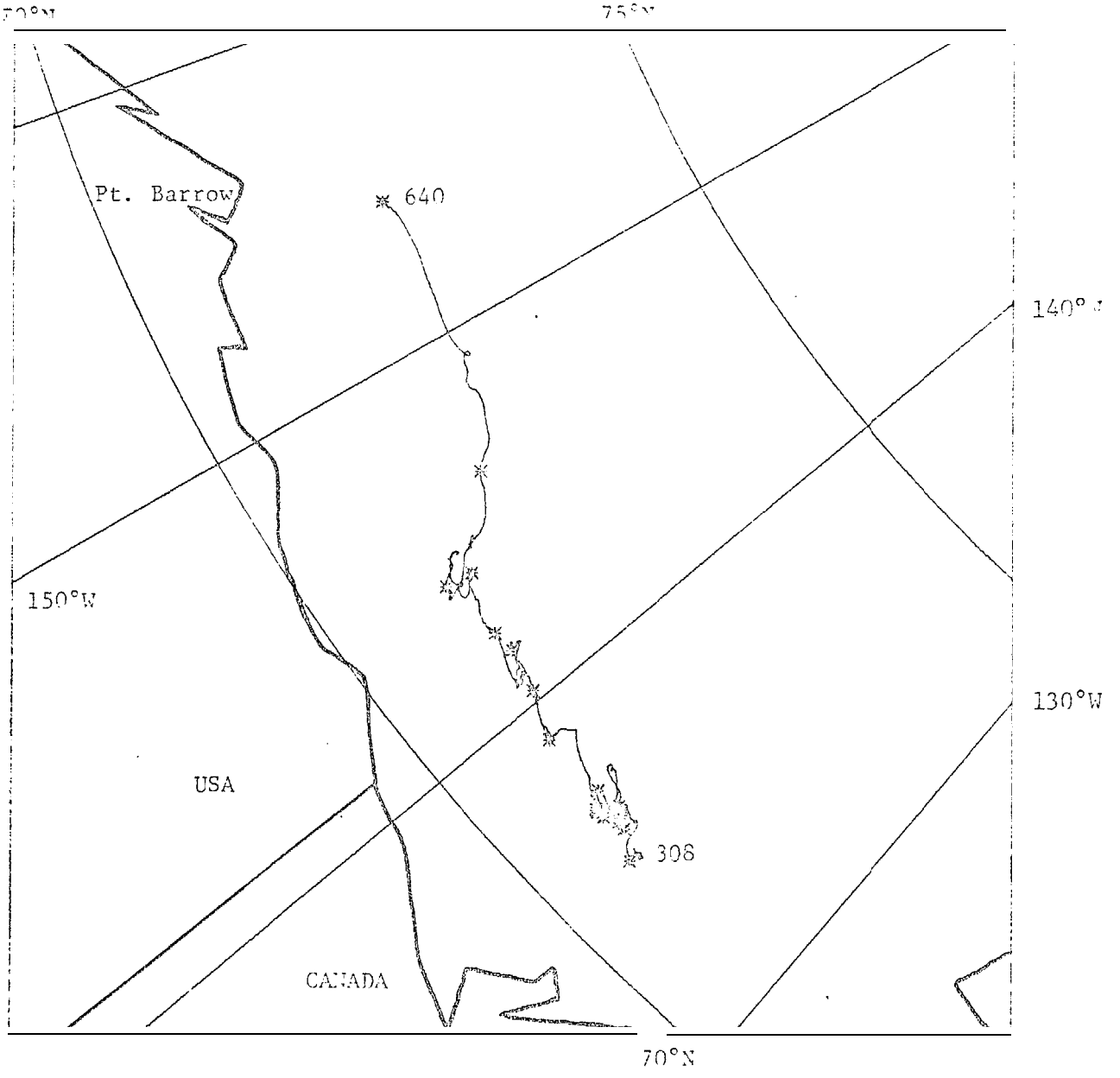

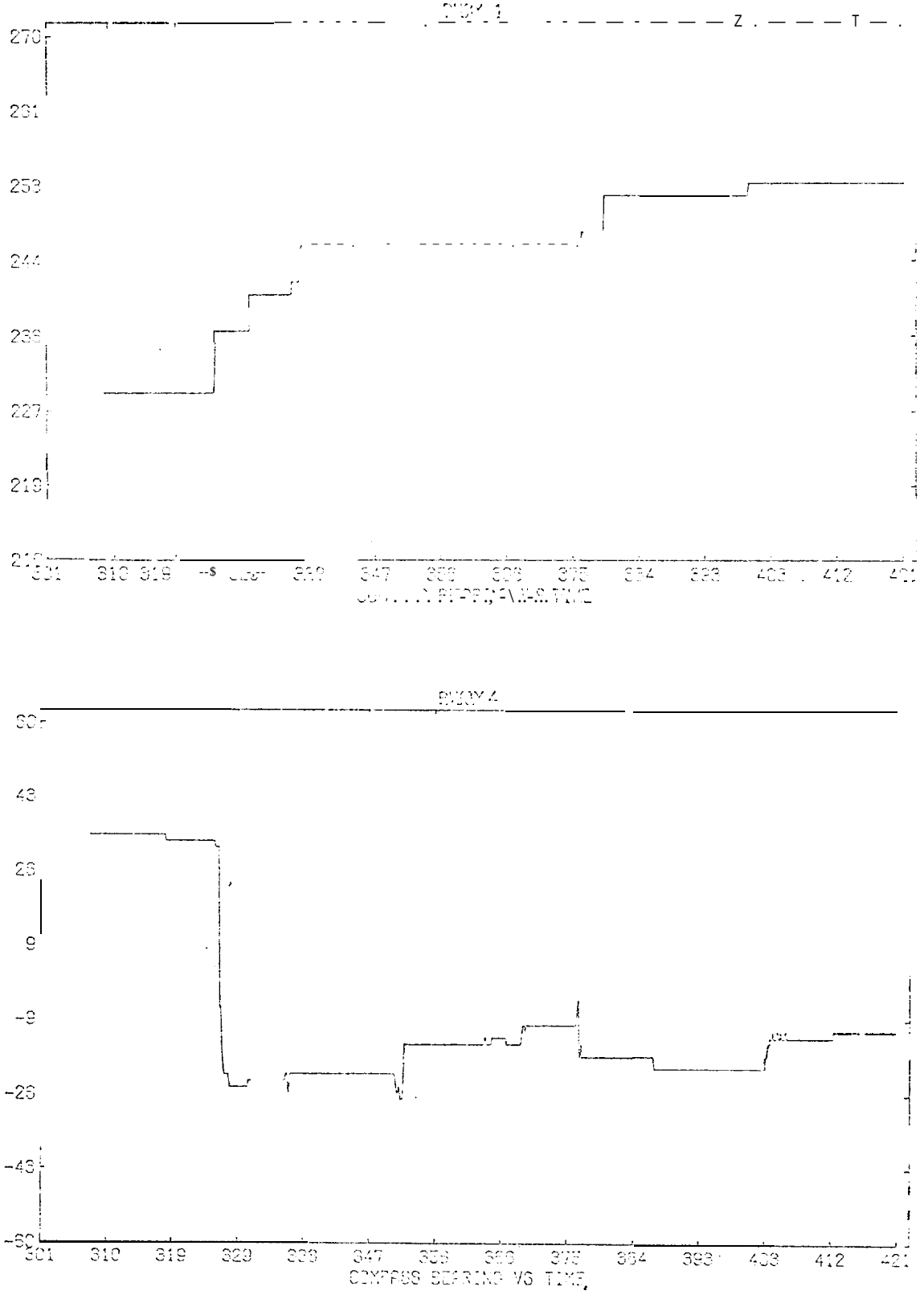

Figure 3." Magnetic Azimuth Buoys 1 and 4, Day 301 to 421 (28 Oct. 75 to 25 Feb. 75).

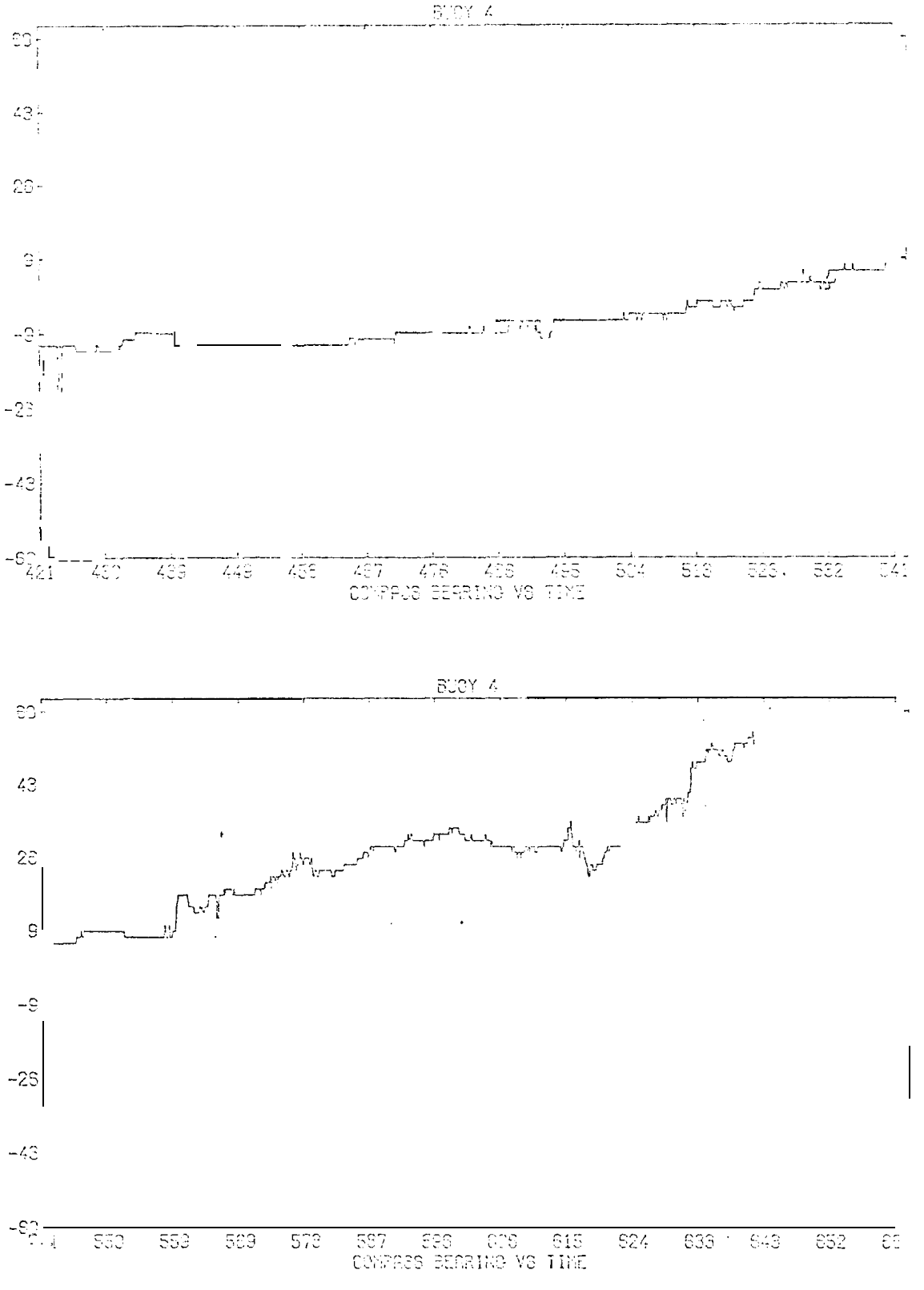

Figure 4. Magnetic Azimuth Buoy 4, Day 421-661 (25 February 76 to 22 October 76).

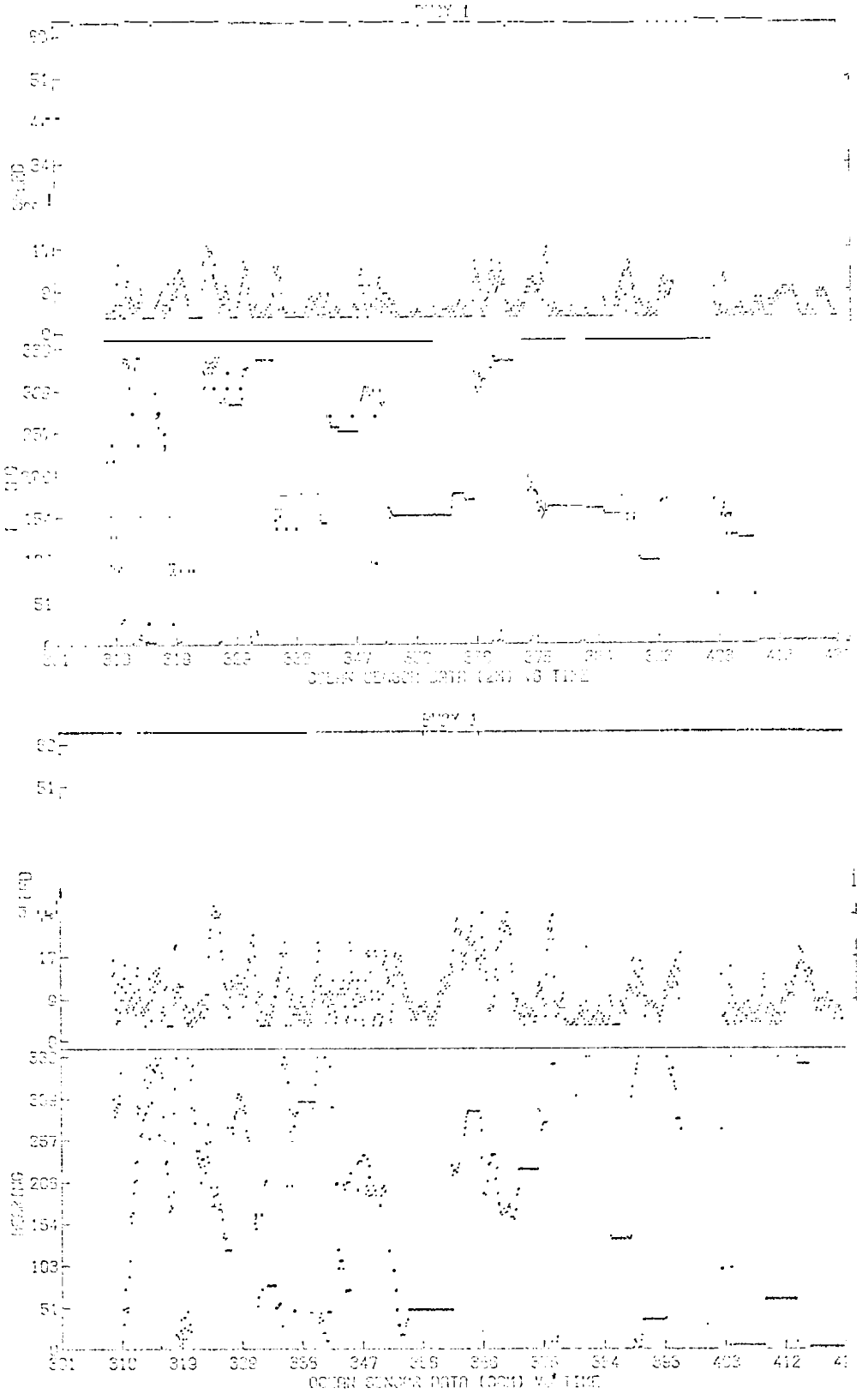

Figure 5. Current Meter Data from Buoy M/O 1, 28 October 75 to 25 February 76. Speed is in cm/s, bearing is degrees clockwise from buoy azimuth.

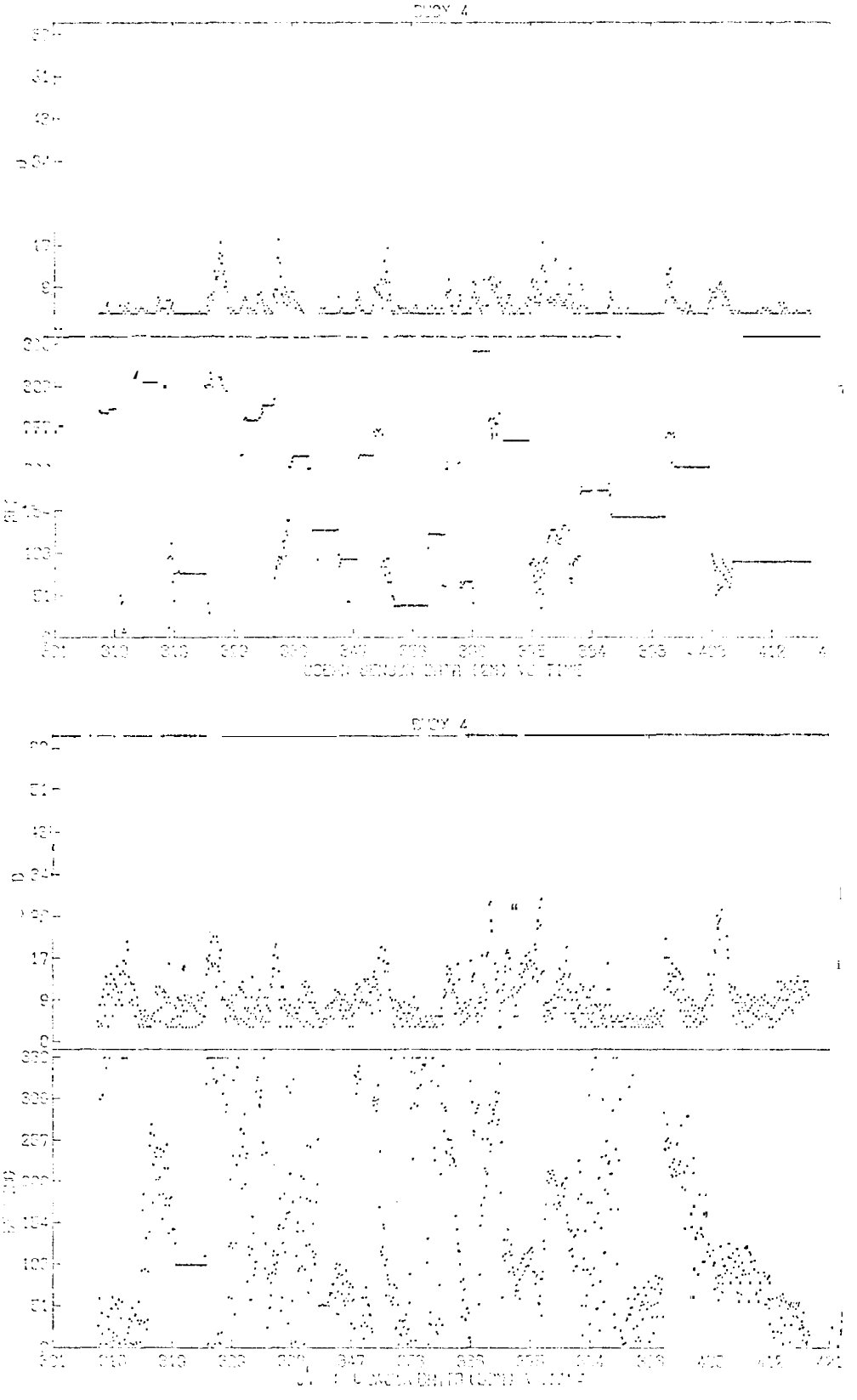

Figure 6. Current Meter Data from Buoy M/O 4, 28 October 75 to 25 February 76.

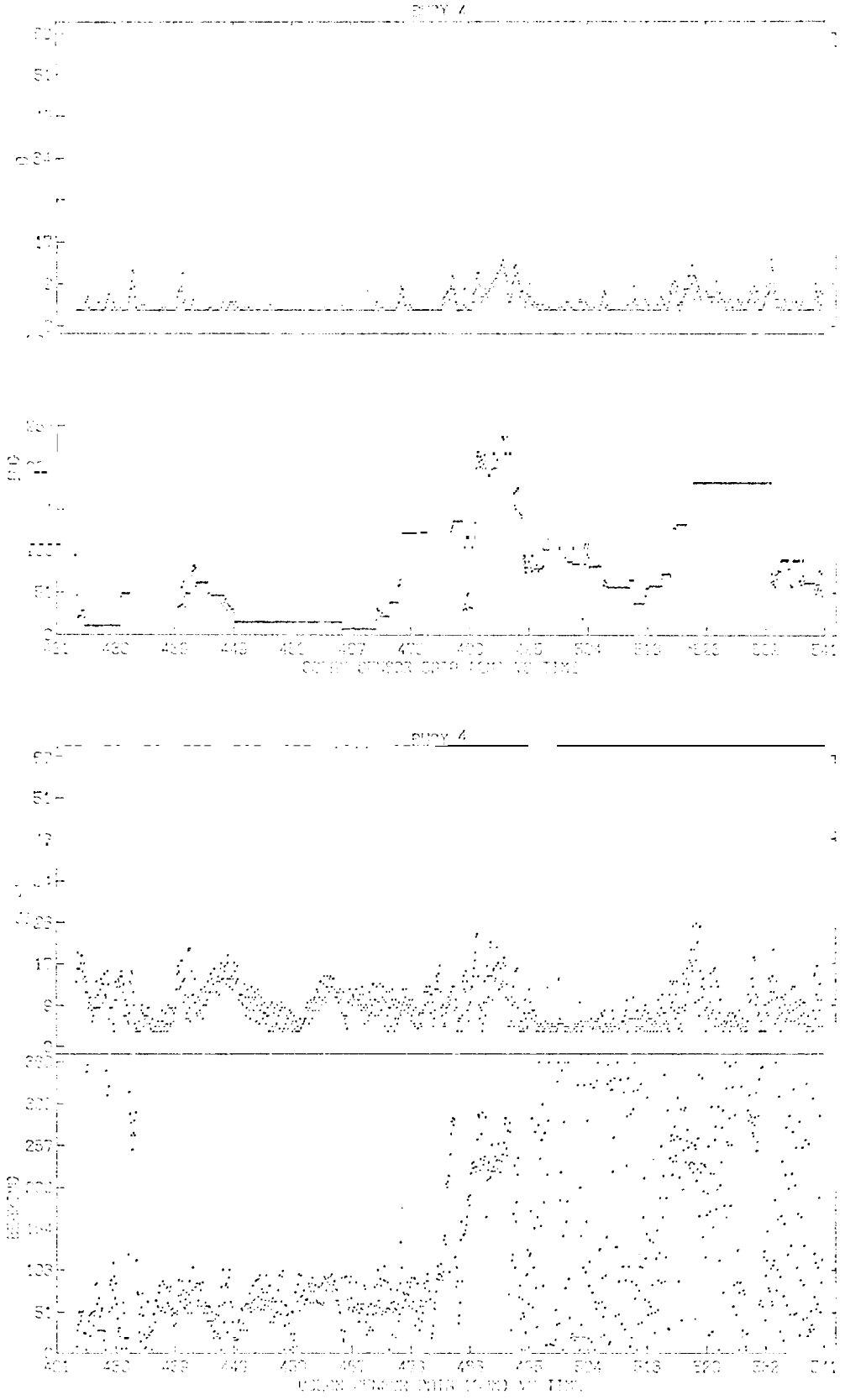

Figure 7. Current Meter Data from Buoy M/O 4, 25 February 76to 24 June 76.

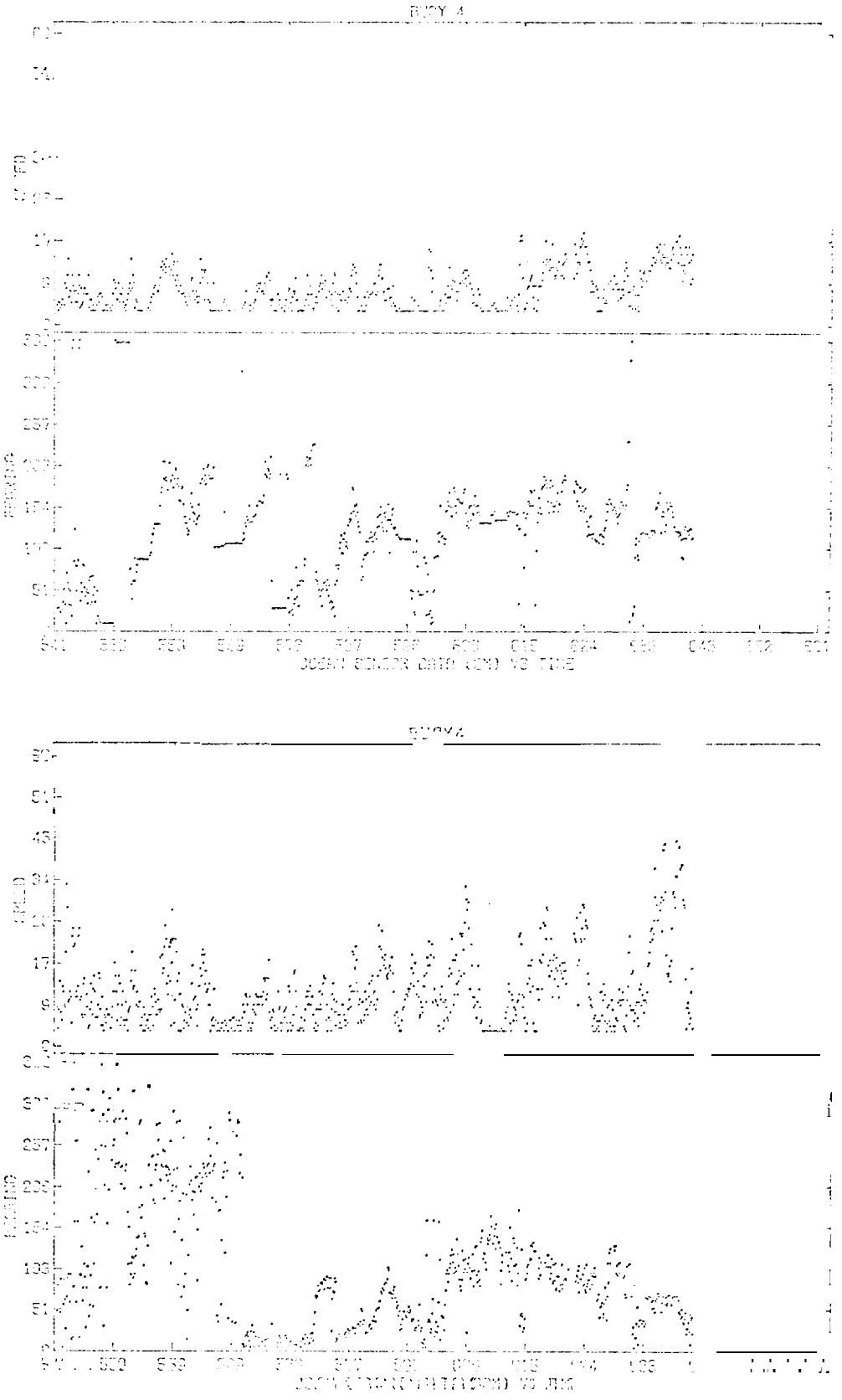

Figure 8. Current Meter Data from Buoy M/O 4, 24 June 76 to 22 October 76.

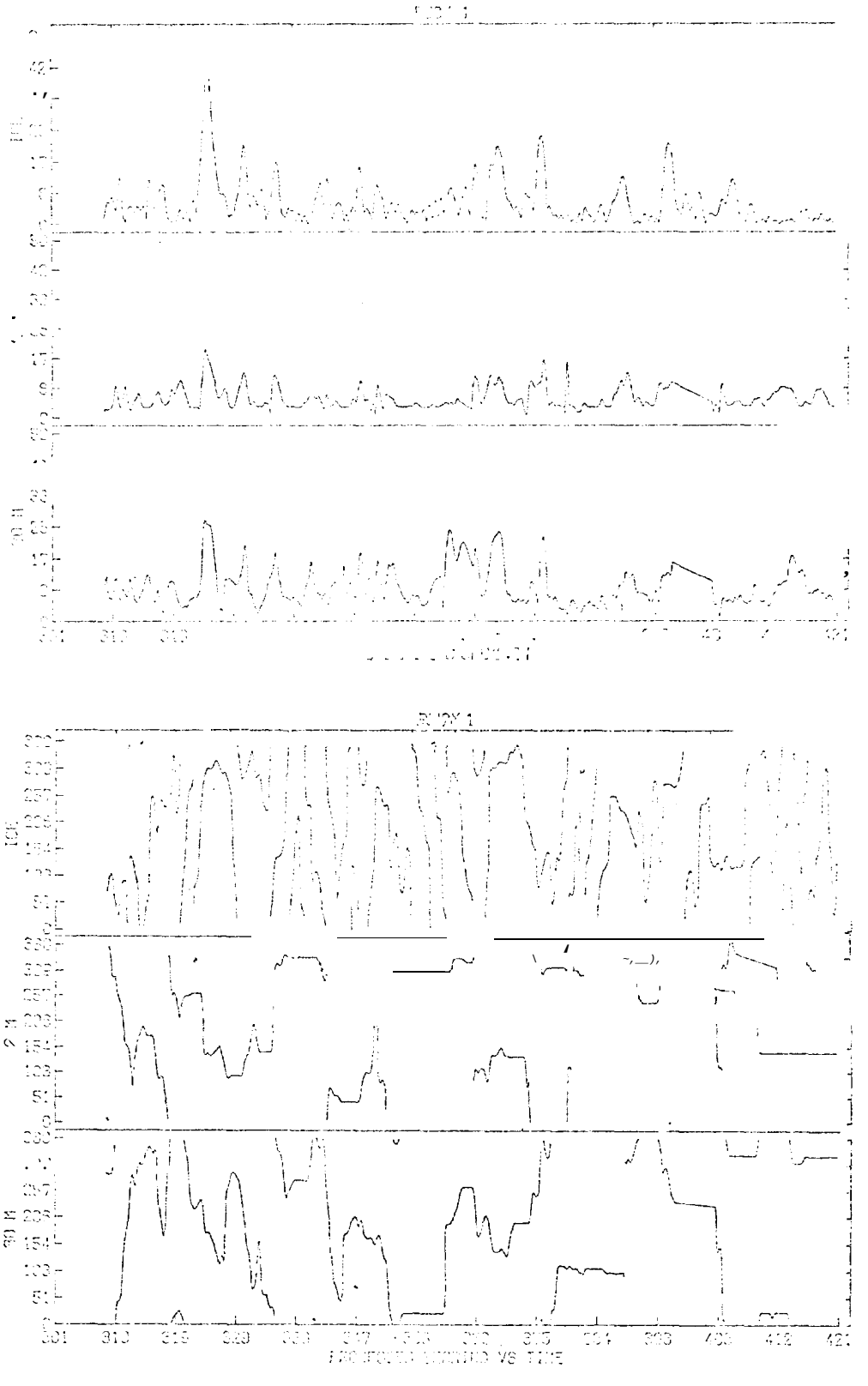

Figure 9. Smoothed and Corrected Data, Buoy M/O 1. Speed is cm/s, bearing is degrees clockwise from true north. Current data are apparent speed and direction relative to the drifting buoy.

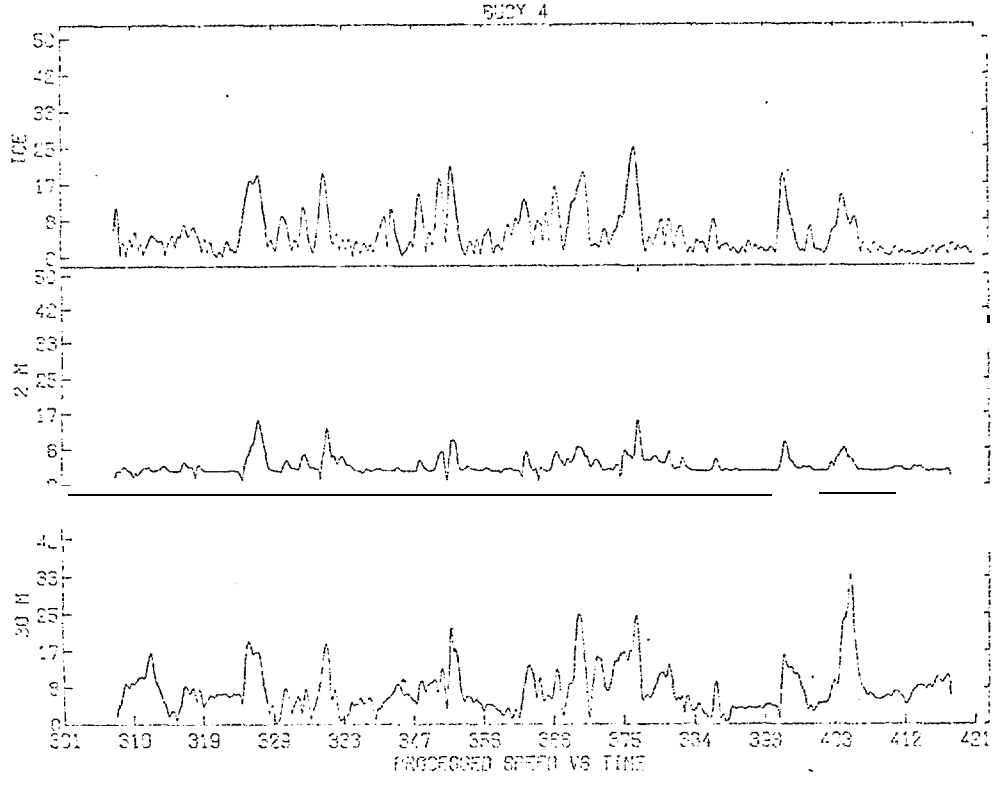

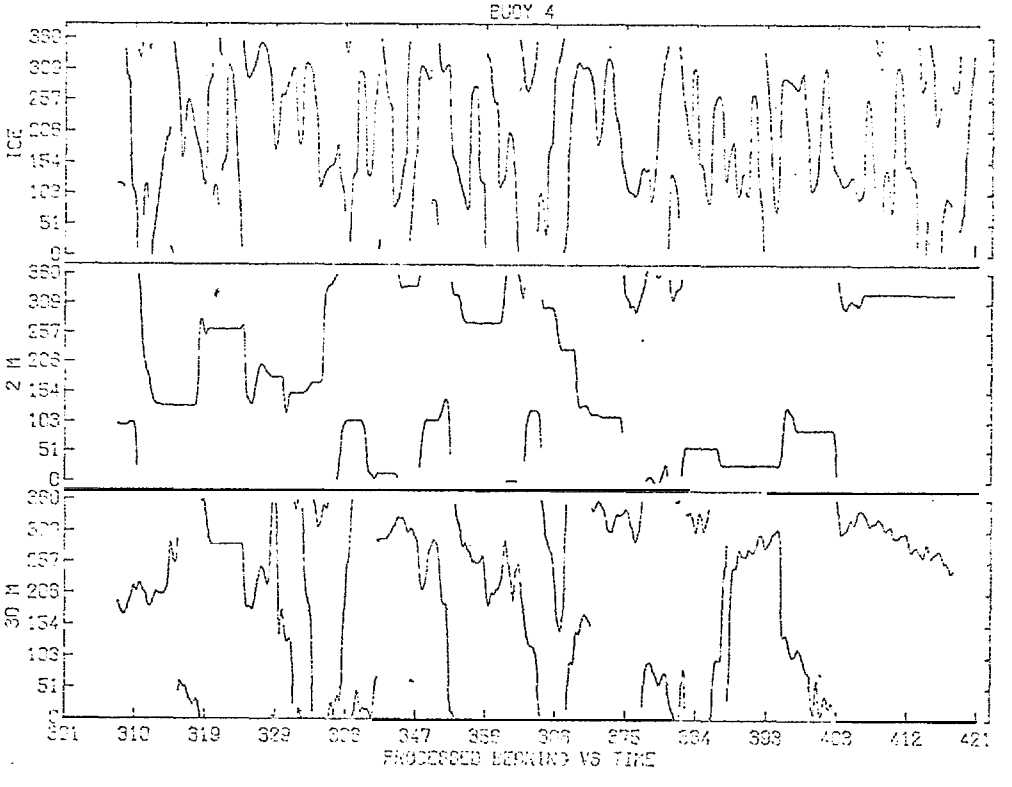

Figure 10. Smoothed and Corrected Data, Buoy M/O 4.

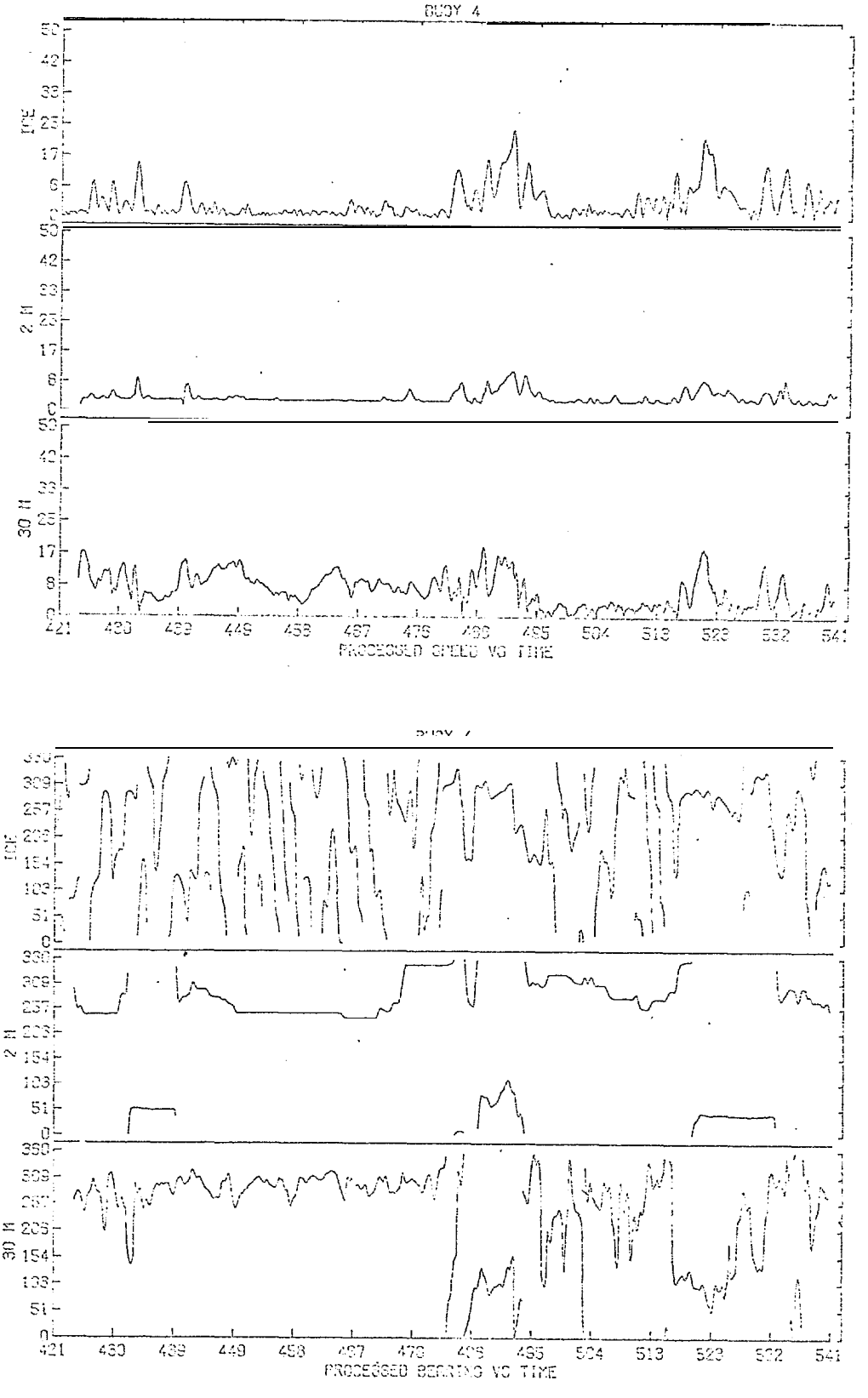

Figure 11. Smoothed and Corrected Data, Buoy M/O 4.

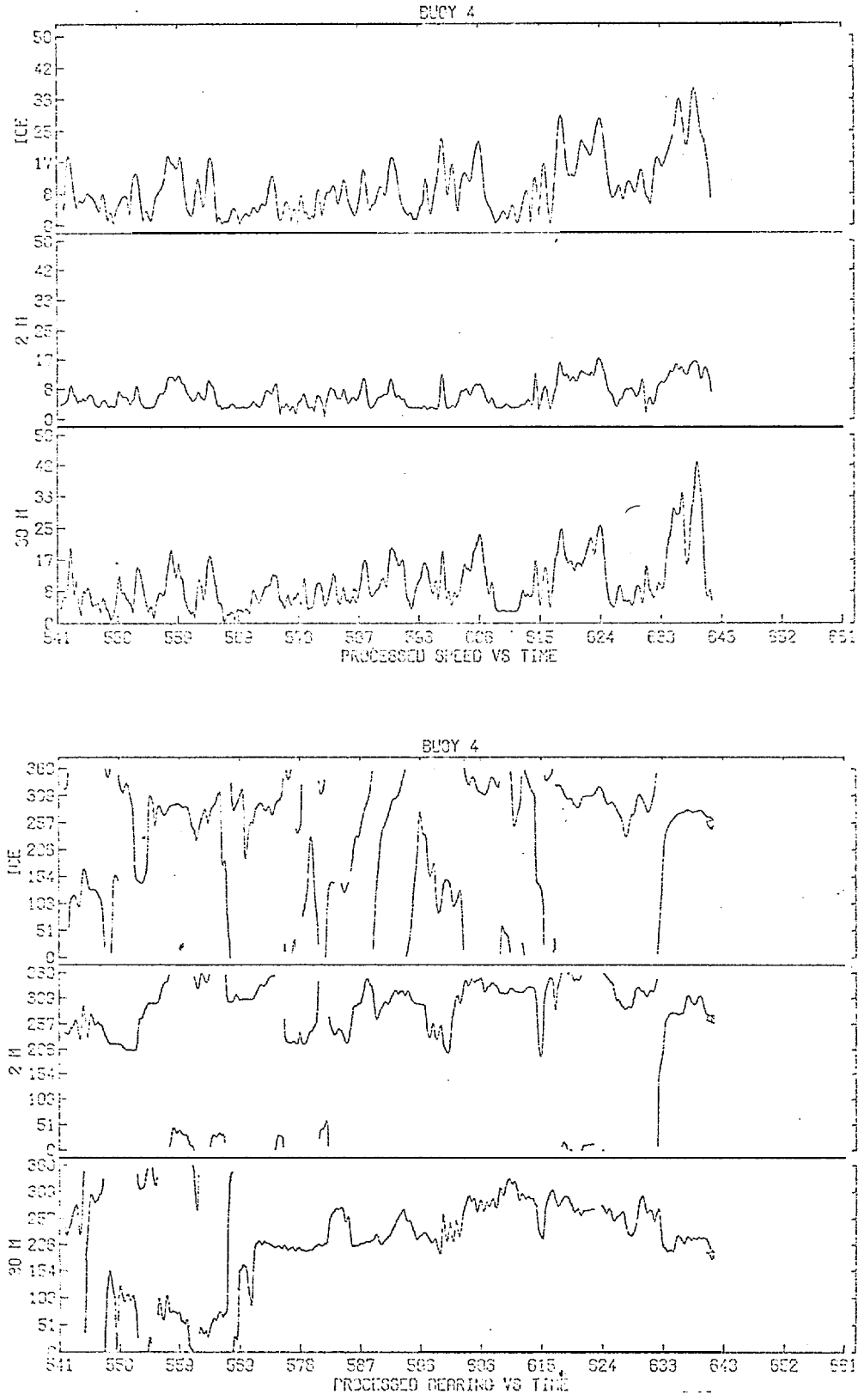

Figure 12. Smoothed and Corrected Data, Buoy M/04.

APPENDIX 3

WINTER ICE DYNAMICS IN THE NEARSHORE BEAUFORT SEA

by

Robert S. Pritchard
Max D. Coon
Miles G. McPhee
Eric Leavitt

March 1977

ABSTRACT

Ice conditions and motion in the nearshore Beaufort Sea from 27 January to 3 February, 1976 were strongly affected by ice stresses. We chose to simulate this response using the AIDJEX model. There is no motion during the first two days. When motions begin, they are westward. There is a time lag with ice in the eastern portion responding later. In the nearshore a fast ice region exists that is separated from the moving pack by a discontinuity. These conditions are verified by NOAA satellite imagery and data from drifting buoys and AIDJEX manned camps. The model is shown to simulate these features accurately, including the velocity discontinuity. This test of the AIDJEX model shows that we understand how ice responds on the large scale to driving forces and are able to describe this relationship at times when the ice stress exerts a dominant influence on the response. This model allows us to use winds (including the large set of historical winds) to determine ice velocity (and trajectories) and to estimate the large-scale average forces that pack ice may exert.

INTRODUCTION

This report describes the ice conditions and dynamics in the Beaufort Sea from January 27 through February 3, 1976. In addition to describing observed response of the atmosphere, ice, and ocean, we present a simulation of the ice conditions using the AIDJEX ice model. The time period was chosen because the ice dynamics conditions and motion are very interesting and because there is a considerable amount of high quality data from the AIDJEX program taken during this period of time. The motion of the ice during this period is greatly influenced by the internal stress in the ice pack. A flaw lead is developed along the north coast of Alaska, extending from Pt. Barrow to the Mackenzie Delta. Shoreward of the flaw lead the ice has very little motion; however, seaward of this lead the ice shows

appreciable motion. However, even in the regions where there is appreciable motion the amount and direction of it is greatly influenced by the internal stress. A detailed description of these conditions is given in this report.

In Figure 1 we show the region of interest together with the position of data stations for the AIDJEX program [the data station numbers shown in Figure 1 are the same as those used by Thorndike and Cheung (1977) and in Appendix 1 to report on sea ice motions observed during AIDJEX and as part of this work]. Stations numbered 1, 3 and 2 were manned camps where extensive measurements in the atmospheric and oceanic boundary layers were taken. These camps are also identified by radio call names of Caribou, Snow Bird and Blue Fox, respectively, We have used directly the positions and barometric pressure measured at each camp. The data from the AIDJEX stations and NOAA satellite imagery are used in the next section of this report to describe the ice conditions during the time period in question.

A simulation of the ice dynamics for the region shown in Figure 1 has been made using the AIDJEX ice model. In the simulation, part of the data from AIDJEX stations is used to drive the model and the remaining data are used to verify the quality of the simulation.

ICE CONDITIONS

Daily velocity (average velocity during a day) is shown for eight days for all stations in Figure 2. On January 27 and 28 there is essentially no motion of any station. As will be shown later, there is appreciable air stress applied to the ice during those days. On January 29 the westernmost stations begin to move and over days January 30 and 31 there is a predominantly western motion of all stations except for those in the Alaskan nearshore area, where the stations have essentially no motion. During February 1, 2 and 3 the ice motion reverses. To obtain a more detailed view of how the ice motion develops during this time, velocity time

histories are shown for several of the stations in Figures 3 and 4. Figure 3 indicates the north-south and east-west components of the velocity for stations 3 (Snow Bird) and 2 (Blue Fox). The major velocity component during the time period is directed east-west. We also see that the east-west motion of station 3 begins a half day before station 2. This indicates that the disturbance that causes the motion travels from west to east across the Beaufort Sea and this disturbance produces motion in the ice which is predominantly in the east-west direction. This fact is supported by motions of other stations, e.g., 66 and 17, shown in Figure 2. Figure 4 shows the velocity time history for stations 44, 1 (Caribou), and 22. From Figure 1 it can be seen that these stations are aligned more or less north-south. The largest velocity component at stations 44 and 1 are directed in the east-west direction. We also see that station 1 and 44 begin their motion at essentially the same time (even though the peak occurs later). Again, the disturbance moves west to east. Station 22 shows no appreciable motion during the time period. This indicates that there is a large velocity difference between stations 1 and 22, which is, of course, what was seen in Figure 2 with the average daily velocities.

The characterization of the motion that emerges from Figures 2, 3 and 4 is also indicated clearly in NOAA satellite imagery for the period shown in Figures 5 through 8. All figures show the locations of the AIDJEX stations, and Figure 5 shows the outline of the area of interest. The NOAA images show a development of a series of cracks in the ice running essentially north-south from the flaw lead to the northernmost boundary of the area of interest. The flaw lead is not apparent in the earlier imagery, but by 2 February it is fully developed. It is at the flaw lead that the velocity discontinuity apparent in Figures 2 through 4 arises. It is the opening of cracks running north-south that produces the east-west motion of the stations indicated in Figures 2 through 4. The progression of these cracks occurring in time sequence from west to east across the area is consistent with the

velocity time histories shown in Figure 3.

In addition to examining the kinematics of the sea ice, it is important to look at forces acting on the sea ice. We begin by discussing the atmospheric boundary layer model used in the AIDJEX model simulation. Specifically, we discuss the procedure for determining the drag coefficient and turning angle from observed conditions. A similar discussion follows in the oceanic boundary layer. Finally, we study the forces acting on the ice and the resulting motions of the manned camps (Caribou and Blue Fox).

The barometric pressure field defines the atmospheric geostrophic flow U. The planetary boundary layer relates the surface traction exerted by the atmosphere on the upper ice surface $\underset{\sim}{\tau}_a$ to the geostrophic flow [Brown, 1976]. The air stress is computed as a quadratic function of $\|\underset{\sim}{U}\|$ applied at an angle α counterclockwise from $\underset{\sim}{U}$:

$$\underset{\sim}{U} = \frac{1}{\rho_a f_c} \underset{\sim}{k} \times \nabla p \tag{1}$$

$$\underset{\sim}{\tau}_a = \rho_a C_D \|\underset{\sim}{U}\| \underset{\sim}{B}_a \underset{\sim}{U} \tag{2}$$

where

ρ_a = air density,

f_c = 14.15×10^{-5} See-l is the Coriolis parameter at 76"N latitude,

C_D = a dimensionless drag coefficient,

$$\underset{\sim}{B}_a = \begin{pmatrix} \cos\alpha & -\sin\alpha \\ \sin\alpha & \cos\alpha \end{pmatrix},$$

$\underset{\sim}{k}$ = unit vector upward and orthogonal to plane of motion, and

Vp = horizontal gradient of barometric pressure p.

The surface air stress can also be related to the square of the meanwind speed measured at 10 meters above the ice surface

$$\tau_a = \text{pa}\ C_{10} U_{10}^2 \tag{3}$$

where C_{10} is the 10 meter drag coefficient. Combining (2) and (3) we can express C_D as a function of C_{10} and the ratio U_{10}/G.

$$CD = C_{10}\ (U_{10}/G)^2 \tag{4}$$

Some measurements of C_{10} from a site near camp Big Bear in spring 1975 are reported by Leavitt et al. (1977). The mean value of C_{10} was 1.3×10^{-3} but the measurements showed a variation with wind direction, from 1.0×10^{-3} to 1.5×10^{-3}. These measurements were taken over smooth floes and do not include the effect of "form" drag due to pressure ridges or rubble fields. For typical ice conditions in the Beaufort Sea Arya (1975) predicts that the drag due to ridges would be approximately equal to that over the smoother ice; for example; this would suggest $C_{10} \simeq 2.6 \times 10^{-3}$. Carsey and Leavitt (1977) have calculated air stress by integrating wind profiles through the boundary layer. These wind profiles were obtained by tracking the motion of balloons (pibals) as they ascended through the boundary layer. A preliminary estimate of U_{10} from these data is 2.7×10^{-3} which agrees with Arya. The confidence limit on this estimate is 0.7×10^{-3}.

Preliminary analysis of pibal data and recorded surface winds for this period suggest $(U_{10}/G)^2 = .3$ and a turning angle $\alpha = 28°$. These values are used to compute the drag coefficient

$$C_D = 0.8 \times 10^{-3} \tag{5}$$

which is used to compute air stress from the geostrophic wind for the simulation. Further comparisons between surface and geostrophic winds suggest that the mean turning angle for this period is 35° rather than 28°, but the standard deviation in this estimate is 15°. The value used is therefore within the range of uncertainty.

A comparison between geostrophic and surface wind derived stresses at each of the manned camps is shown in Figures 9-11. The agreement is excellent except for 30 and 31 January, when the east-west component of air stress obtained from geostrophic velocity exceeds the value determined from surface winds. Barometric pressures at the manned camps have been found to be in error by 0.1 mb at this time. Corrected values reduce the air stress by about 20%. The corrected air stress is shown in Figures 9-11. The uncorrected value has been used in the simulation presented later in this report.

Figure 12 shows a balance of dynamic forces derived from smoothed records of measured quantities at station Caribou sampled at 1200 GMT on 30 January. The force balance is a sum of air stress $\underset{\sim}{\tau}_a$, water stress $\underset{\sim}{\tau}_w$, Coriolis force $\underset{\sim}{f}_c$ and a residual R where

$$\underset{\sim}{\tau}_a + \underset{\sim}{\tau}_w + \underset{\sim}{f}_c + \underset{\sim}{R} = \underset{\sim}{0} \qquad (6)$$

The water stress is related to ice velocity by

$$\underset{\sim}{\tau}_w = \rho_w C_w \|\underset{\sim}{v}\| \underset{\sim}{B}\,\underset{\sim}{v}$$

$$\underset{\sim}{B} = \begin{pmatrix} \cos(\pi+\beta) & -\sin(\pi+\beta) \\ \sin(\pi+\beta) & \cos(\pi+\beta) \end{pmatrix} \qquad (7)$$

and Coriolis force is

$$\underset{\sim}{f}_c = -m f_c \underset{\sim}{k} \times \underset{\sim}{v}$$

where ρ_w is the water density, m is the ice mass per unit area (300 gm cm-z), f_c is the Coriolis parameter and β is the angle of turning. The resultant vector $\underset{\sim}{R}$ is required to balance the equation and represents internal ice forces, sea tilt, and ice inertia. We have used summer conditions when the ice is not compact enough to support appreciable internal stress (i.e., $\underset{\sim}{R}$ is small) to evaluate the water stress constants. The best results were obtained with $C_w = 0.0055$ and $\beta = 23°$ using

observed surface winds, and a drag coefficient $C_{10} = 0.0027$. During 30 January it is clear that R is an appreciable force acting on the ice. Therefore, ice stress is an important factor in any simulation of this period.

Figures 13, 14 and 15 show time series of forces and velocities as measured at the three manned camps. In the top segment of each plot are shown the air stress component as determined from the 10-meter wind ($\underset{\sim}{\tau}_a = \rho_a C_{10} |\underset{\sim}{U}_{10}| \underset{\sim}{U}_{10}$), along with the negative component of the resultant vector, $\underset{\sim}{R}$. From (6) and (7), it is clear that $\underset{\sim}{R}$ and $\underset{\sim}{\tau}_a$ will be equal and opposite when there is no ice motion, thus the plotted curves coincide for the first few days. When the ice velocity increases, the water drag and Coriolis force become increasingly important. We further analyzethe forces by considering how the ice would behave if it were too weak to support an internal stress gradient. Then $\underset{\sim}{R} = \underset{\sim}{0}$ and (6) can be solved for the wind-driven velocity, $\underset{\sim}{v}_{wd}$. Solutions for wind-driven drift are shown along with the measured velocities as the lower traces of each plot. Observed motions are constrained to an east-west direction by the ice stress. Wind-driven drift has a larger north-south component. This is also indicated by the sizable southward components of internal force on 30 January *at Caribou* (Figure 12) and Snow Bird even though there was practically no north-south component of surface wind.

An important question to ask is how much does the internal ice stress affect the trajectory of a given point? To this end, Figure 16 indicates the observed trajectory of station 1 (Caribou) and the wind-driven trajectory. It can be seen clearly that the difference between these trajectories is very large. At the end of the eight-day period there is a difference in position of approximately 25 kilometers. The internal ice stress has retarded the motion of the ice by this amount.

MATHEMATICAL MODEL

Conservation of momentum in this system accounts for air stress $\underset{\sim}{\tau}_a$, water stress $\underset{\sim}{\tau}_w$, divergence of ice stress $\nabla \cdot \underset{\sim}{\sigma}$ ($\underset{\sim}{\sigma}$ is the Cauchy stress in excess Of isostatic equilibrium integrated through the thickness in this two-dimensional material model), Coriolis acceleration $-mf_c \underset{\sim}{k} \times \underset{\sim}{v}$ and sea surface tilt $(mf_c \underset{\sim}{k} \times \underset{\sim}{v}_g)$

$$m\dot{\underset{\sim}{v}} = \underset{\sim}{\tau}_a + \underset{\sim}{\tau}_w + \nabla \cdot \underset{\sim}{\sigma} - mf_c \underset{\sim}{k} \times (\underset{\sim}{v} - \underset{\sim}{v}_g) \tag{8}$$

where m = mass per unit area, and $f_c = 14.15 \times 10^{-5}$ See-l is the Coriolis parameter at 76"N latitude. The notation (*) implies differentation along the particle path and V is the spatial gradient operator.

The oceanic boundary layer is represented by a quadratic drag law similar to that used in the oceanic boundary-layer as shown in equation (7). Water drag, however, is a function of the ice velocity relative to the geostrophic current $\underset{\sim}{v}_g$. The relationship is

$$\underset{\sim}{\tau}_w = \rho_w C_w \| \underset{\sim}{v} - \underset{\sim}{v}_g \| \underset{\sim}{B} (\underset{\sim}{v} - \underset{\sim}{v}_g) \tag{9}$$

where all variables except $\underset{\sim}{v}_g$ have been defined previously. The geostrophic flow is assumed to be given by long-term mean observed values. In Figure 17 we present the values. Values at intermediate locations are computed by linear interpolation between values defined on the 75 km square grid.

The elastic-plastic constitutive law developed by the AIDJEX modeling group (Coon et al., 1974; Coon and Pritchard, 1974; Pritchard, 1975) relates stress to the deformations. We assume a stiff linear elastic response.

$$\underset{\sim}{\sigma} = (M_1 - M_2) \underset{\sim}{1} \operatorname{tr} \underset{\sim}{e} + 2M_2 \underset{\sim}{e} \tag{10}$$

where $\underset{\sim}{e}$ is the elastic strain. Moduli used in each simulation are presented in Table 1. The moduli are large enough so that elastic strain cannot exceed 0.2

percent. The rate of change of elastic strain is determined from

$$\dot{\underset{\sim}{e}} - \underset{\sim}{W}\underset{\sim}{e} + \underset{\sim}{e}\underset{\sim}{W} = \underset{\sim}{D} - \underset{\sim}{D}_p \tag{11}$$

where stretching $\underset{\sim}{D} = 1/2(\underset{\sim}{L} + \underset{\sim}{L}^T)$ and spin $\underset{\sim}{W} = 1/2(\underset{\sim}{L} - \underset{\sim}{L}^T)$ are obtained from the velocity gradient $\underset{\sim}{L} = \nabla\underset{\sim}{v}$. The plastic stretching $\underset{\sim}{D}_p$ is defined by the normal flow rule

$$\underset{\sim}{D}_p = \lambda \frac{\partial \phi}{\partial \underset{\sim}{\sigma}} \tag{12}$$

where λ is a positive multiplier. Finally, the yield criterion

$$\phi(\underset{\sim}{\sigma}, p^*) \leq 0 \tag{13}$$

completes the description. The yield surface has been assumed to have the shape of a "squished teardrop" as shown in Figure 18. The family of curves has been normalized by p^*. The surfaces are defined by

$$\phi = \sigma_{II} + \tan b\, \sigma_I (1 + \sigma_I/p^*)^{\frac{1}{2}} \tag{14}$$

where b is the angle at which the curve approaches the origin ($\underset{\sim}{\sigma} = \underset{\sim}{0}$). We have chosen $b = 30°$ since this value has been found to be reasonable in previous simulations (Pritchard, Coon and McPhee, 1977). Yield strength p^* determines the size of the surface given by equation (14). For the set of simulations we have varied p^* as a parameter, setting it to a constant in each calculation. Thus, we have used a perfect plasticity model.

An important feature of the AIDJEX ice model is the ice thickness distribution. It is this variable that distinguishes ice conditions by describing the relative area covered by ice of each thickness. One of the properties of the ice model that depends on thickness distribution is the yield strength p^*. In our current state of thinking we believe that strengths found from thickness distributions are too low to allow realistic simulation of ice motion and deformation (Pritchard, 1977).

Therefore, we have bypassed this part of the model in favor of varying p^* as an arbitrary input parameter. The results of this work provide critical information on strength needed to simulate ice response and shall provide direction as we reformulate the redistribution function and the energetic argument that enable us to determine strength from the thickness distribution.

QUASI-STEADY NUMERICAL INTEGRATION

In previous simulations (Coon et al., 1976; Pritchard, Coon and McPhee, 1976) we have input air stress fields each six hours and boundary velocities each three hours with values determined at intermediate times by linear interpolation. Solutions were then obtained using a difference approximation known as the leapfrog scheme (Pritchard and Colony, 1976). This scheme requires numerical time steps on the order of 2 minutes for cells that are 40 km wide using typical elastic parameters, say $M_1 = 1/2 \times 10^{11}$ dyn cm^{-1} and $M_2 = 1/4 \times 10^{11}$ dyn cm^{-1} and an area mass density of m = 300 gm cm-z. The Courant condition is assumed to give $c\,\Delta t/\Delta x \leq 1/2$ where $c = [(M_1+M_2)/m]^{\frac{1}{2}}$. *See* Table 1 for values used in the simulation.

The fundamental concept of the AIDJEX model is that the physical processes of ridge building and lead formation are the mechanisms that provide deformation. The model further assumes that a large-scale spatial average (~ 100 km) is being described. We feel it is consistent with these ideas that temporal variations be resolved on scales of the order 1 day. To be more compatible with these concepts, we have modified the numerical scheme. We have averaged the air stress and the boundary velocity over each one-day interval and now seek to find the steady state response of the model to the constant driving forces. The ice acceleration may be rewritten

$$\dot{\underset{\sim}{v}} = \underset{\sim}{v}_t + \underset{\sim}{L}\,\underset{\sim}{v} \qquad (15)$$

where $\underset{\sim}{v}_t$ is the partial derivative of velocity $\underset{\sim}{v}(\underset{\sim}{x},t)$ with time and $\underset{\sim}{L}\,\underset{\sim}{v}$ represents advection. Since we seek steady solutions (by which we mean that velocity is constant, not zero), we see that an Eulerian formulation is simpler to visualize. In that case $\underset{\sim}{v}_t = \underset{\sim}{0}$. The contribution of advection to the momentum balance is an apparent force

$$\underset{\sim}{f}_a = m\,\underset{\sim}{L}\,\underset{\sim}{v} \tag{16}$$

The magnitude is on the order of

$$\|f_a\| \leq m\,\|L\| \cdot \|v\| \tag{17}$$

where velocity gradient $\|L\| \approx 1 \times 10^{-5}$ see-l in the marginal ice zone and velocity $\|v\| \approx 20$ cm see-' in the pack ice so that as a worst case

$$\|f_a\| \approx .06 \text{ dyn cm}^{-2} \tag{18}$$

which is an order of magnitude smaller than significant forces in equation (8). Therefore, we neglect advection in the simulations.

For completeness, we must similarly evaluate the advection of elastic strain in equation (11). However, we have no accurate estimate of the spatial gradient of elastic strain. Therefore, without proof we neglect this advection term also, but note that the elastic response is as much a numerical artifact as a physical reality. Furthermore, elastic strains are constrained to be less than .2% by choosing moduli (M_1 and M_2) to be large. From these arguments we feel that the assumption is valid.

Our results show that some variations still occur during the last cycle of iteration. It is at this time that we are assuming the solution to have reached steady state. Forces appear to vary less than 0.1 dyn cm^{-2} during the last hour of iteration (approximately 60 cycles) and this difference is acceptable. Since the

quasi-steady concept is a new one, we have not felt justified in developing a criterion to decide when the solution has coverged because we have only begun to decide whether or not we should continue the quasi-steady solution method. Present indications are that the method is an improvement over our previous scheme in which solutions vary continuously and we shall begin to look into the convergence question in more detail.

PROBLEM CONFIGURATION

The locations of 17 data buoys and three manned camps have been shown in Figure 1. We have chosen to use the four northernmost and the two westernmost buoys (one buoy common to both) to provide boundary conditions for the simulation. The boundary is assumed" fixed to shore along the North Slope from Pt. Barrow east to Banks Island. The motion of each of the other two section of boundary is obtained using a spline interpolation polynomial with zero second derivatives at the end points. For example, a spline interpolation 'polynomial using four data buoys and a fixed point provides velocities at each grid point lying along the northern boundary of the grid. A generally rectangular grid is set up in the interior of the region. The interior points are chosen so that each additional buoy or camp lies either on a grid point or on a line to simplify interpolation of solutions for comparison. The fifteen interior stations allow us to test the performance of the model at reproducing observed motions. We have regenerated a grid for each day of the calculation because of the motion that occurs. This detail is necessary so that the computed results can be interpolated properly for direct comparison with observations.

RESULTS

Wind-driven drift velocity is presented in Figure 19. This velocity is obtained as a balance between all forces considered in the complete AIDJEX model except for

ice stress divergence. The wind-driven velocity is calculated at each point independent of information at surrounding points using the air stress fields shown in Figure 20. During 27 and 28 January when air stress was quite small over much of the domain and was less than about 2 dyn cm^{-2} near the Alaskan North Slope, the wind-driven velocity ranged from a low of about 5 cm sec^{-1} that reflected transport on the geostrophic ocean current to high speeds on the order of 25 cm see-l where the winds are largest. These results may be compared with the observed ice drift (Figure 2) which is essentially zero during these two days. During the next three days (29, 30 and 31 January) the winds rise and the air stress increases to a range of values on the order of 2-5 dyn cm^{-2}. The air stress is more nearly homogeneous on each day blowing toward the west. The wind-driven drift shows most of the domain moving to the northwest at about 20-30 cm sec^{-1}. During the last two days the wind pattern within about 100 km of the Alaskan North Slope shows a steep gradient with wind-driven drift results either zero or turned northward. The speeds are larger than observed at these times but more striking is the fact that the icewas observed to drift westward but the wind-driven drift is to the northwest. During the last three days (1, 2 and 3 February) the winds fall off and turn northward and finally to the northeast. At these times the wind-driven drift generally follows the direction of the observed motion but speeds are typically twice as high as observed speeds. The most striking feature that is modeled poorly by wind-driven drift is the nearshore behavior when ice is motionless in a band nearly 200 km wide along the North Slope and separated by the flaw lead that appears as a velocity discontinuity in the observed motions (Figure 2) and the satellite imagery (Figures 5–8). Instead, the wind driven drift varies smoothly everywhere with spatial gradients dictated by gradients in the air stress field.

The ice model is included in the simulation so that the effect of ice stress divergence may be considered. We have performed the simulation three times during

the time interval 27 January - 3 February. During each of these simulations the yield strength p^* was held at a different constant value throughout the domain. The values are shown in Table 1. The intermediate yield strength of $p^* = 10^8$ dyn cm^{-1} was chosen to agree with the lower bound estimate of Pritchard (1977) during the time interval 10–24 February 1977, just 7 days after the simulation time chosen for the present study. Although a lower bound, the estimate is thought to be a reasonable estimate of the actual value. We have also used values an order of magnitude smaller and larger to see how sensitive the resulting motions are to such variations. For convenience of presentation, we shall first discuss the velocity calculated using the intermediate yield strength (Run 3C). Then we shall show the effect on the velocity field due to changing yield strength, Finally, we shall return to the best estimate to look in more detail at the deformation and stress fields that are obtained.

The sequence of modeled ice velocities determined with yield strength $p^* = 10^8$ dyn cm^{-1} is presented in Figure 21. The accuracy with which we have simulated velocity seems remarkable. The simulated velocity is "to be compared with observed velocity at each available station as shown in Figure 2. During 27 and 28 January the model velocity is nearly zero throughout the domain, which agrees with observed motions. During 29 January as the winds rise we find motion to the northwest in the western half of the domain, which agrees with observed motions. Except for the two buoys at approximately 150 km northeast of Pt. Barrow, the velocity of each interior check buoy and manned camp is accurate to within a few centimeters per second. The discrepancy between the two nearshore buoys and model results is caused at least in part by the velocity profile assumed as a boundary condition. We have interpolated the boundary velocities between the five buoys along the boundary to input the velocity of each grid point. Furthermore, all points along the fixed shore have zero velocity. Therefore, the boundary velocity

smoothly approaches zero as we approach shore. This does not allow the large velocity gradients that are observed to appear near these regions. During 30 January the ice speed increases to about 20 cm sec^{-1} with the wind and the flow to the west. In the Alaska nearshore region steep gradients normal to the shoreline appear. The velocity out to about 80 km is small, comparing well with observed motions. To the east we find that the modeled velocity field continues to move with a lead opening along the shore at Banks Island. The observed velocity decays rapidly in the last 200 km of this region. It is possible that either inaccuracies in the winds, incorrect yield surface shape or the lack of tensile strength of the ice model could cause this error in the approximation. During 31 January, winds are similar to 30 January with the velocities being comparable also. By this day the region off Banks Island is observed to be moving at the same velocity as the area to the west. The most striking feature of the velocity field during 31 January is the region of fast ice along the U.S.-Canada north slope that is separated from the moving pack ice by an abrupt change in velocity--a discontinuity. As seen in Figure 2e, the three buoys within this region are stationary and nearby ones are moving rapidly. We interpret this discontinuity as the flaw lead reaching from Pt. Barrow to Banks Island. We have simulated the existence and location of this discontinuity accurately. Furthermore, the smooth velocity field in the pack ice is simulated accurately also. During the last three days of the simulation (1, 2 and 3 February) the details of the velocity field become less interesting but we find that the modeled velocity does. come around and match the observed motions accurately. The comparison is accurate throughout the domain with negligible motions in the Alaskan nearshore correctly represented.

It is important to point out that while it *is* true that the prescribed boundary velocity has a strong influence on the resulting velocity field, the accurate representation of the velocity field throughout the interior of the domain could only

be achieved by a model that represents sea ice response correctly in a variety of deformation states. We shall demonstrate this point by simulating the response using the same plasticity model but with different valuesof yield strength.

In Figure 22 we present the set of eight velocity fields that result when a yield strength $p^* = 10^7$ dyn cm^{-1} is used (Run 3B). A comparison with wind-driven drift velocities (Figure 19) shows that velocities modeled by the low-strength yield surfaces are similar. In the interior the velocities compare within a few centimeters per second in magnitude and are oriented in approximately the same direction but turned consistently to the left by ice stress divergence by 10-20 degrees. Therefore, as with wind-driven drift, the weak ice model does not provide an accurate simulation of observed buoy and manned camp motions, For example, during the first two days when winds are too low to move the ice we find that the weak ice model instead allows motion. Furthermore, at the boundaries where the velocity is specified by the buoy motions, we find the weak ice model allows a discontinuity to develop in the velocity field. The jump in velocity persists at almost all boundary locations for the entire eight-day period. Finally, the behavior of the weak ice model in the nearshore does not simulate the discontinuous behavior that" is observed to exist. The modeled velocity field instead varies smoothly to the zero boundary value specified at the shore. This is not a reasonable representation of the fast ice zone seen in satellite imagery, in the buoy motions and in the modeled results with yield strength $p^* = 10^8$ dyn cm^{-1} (Run 3C).

To learn how sensitive modeled velocities are to changes in yield strength we felt it to be worthwhile also to perform a simulation with $p^* = 10^9$ dyn cm^{-1} (Run 3D), an order of magnitude larger than the estimated value. However, we felt it unnecessary to simulate all eight days. During the first two days (27 and 28 January) when winds were low and boundary velocities motionless, the model predicted

no motion with a yield strength of $p^* = 10^8$ dyn cm^{-1}. It is therefore not possible to change this velocity field by increasing yield strength. Since sea ice conditions were similar during the next three days (29, 30 and 31 January), we felt it necessary to simulate only one day. We have chosen 30 January as representative. The modeled velocity field during 30 January is presented in Figure 23 for the high yield strength $p^* = 10^9$ dyn cm^{-1}. Although the nearshore region has zero velocity it is seen that the width is far larger than the fast ice region defined by buoy motions (Figure 2). Approximately half of the entire domain is predicted to be at rest. As expected, the strength is so high that no discontinuous behavior is exhibited at boundaries, but in the interior modeled velocities do not compare closely with observed velocities. Results similar to those for the days 27-31 January are expected if the last three days are simulated (1-3 February).

In summary, we find that the perfect plasticity model may be used to simulate the observed velocity field quite accurately when the yield strength is estimated correctly. In particular, fast ice regions in the nearshore are accurately delineated and pack ice motion is accurately represented. The interface between these regions is narrow and is approximated by a discontinuity in the theoretical model (and by a rapid variation across 2-3 cells in the difference approximation). Furthermore, we have learned how sensitive modeled velocity fields are to variations in yield strength. Variations of an order of magnitude provide modeled velocities that are similar to wind-driven if too weak, and strongly dominated by boundary conditions if too strong.

Our attention turns back to the intermediate strength simulation (Run 3C). We now present a more detailed view of the results since the velocity field has been shown to be accurate.

The deformation is shown in Figure 24 for each of the eight days simulated using the strength estimated at $p^* = 10^8$ dyn cm^{-1} (Run 3C). We have presented

the stretching $\underset{\sim}{D}$ which is the symmetric part of the velocity gradient $\underset{\sim}{L} = \nabla \underset{\sim}{v}$. This is the variable considered as strain rate in small deformation theories and is the variable most descriptive of velocity differences throughout the domain. Within each cell of the numerical grid we have displayed the principal values of stretching oriented in the correct directions. Opening and closing in each direction are differentiated by dashed and solid lines, respectively. A line of 1 cm length on the figure represents a stretching value of 8×10^{-7} sec (approximately 8% per day). During the first two days (27 and 28 January) deformations are negligible as were the motions. During 29 January deformations begin to occur around the nearshore with opening at Banks Island and with both shearing and opening north of Alaska. We note that principal values of equal magnitude and opposite sign represent pure shearing--that is, shearing accompanied by no dilatation (area changes). During 30 and 31 January a similar pattern of deformation occurs but principal values are larger. Maximum shearing ($D_{II} = D_1 - D_2$, the difference between principal values) in the two cells approximately 100 km north of the U.S.-Canada land mass is about 16×10^{-7} sec (~ 16% per day). This larger deformation is calculated in a narrow band about two computational cells wide (~ 80 km) and represents the velocity discontinuity that we discussed earlier (Figure 2). Since the numerical technique does not predict discontinuities explicitly, we must interpret these features by studying both the velocity and the deformation fields, It is seen that deformation in the center of the domain is an order of magnitude smaller than in the nearshore region. It should be pointed out that we had expected a region of uniaxial opening to occur along a line running generally northward from the shear zone. This is seen in the satellite images (Figures 5–8) in the form of leads running north to south. This feature of the observed conditions is not represented in the simulation. We shall return to the discrepancy later. During the last three days (1-3 February) the deformations do not show a simple and significant

pattern until 3 February when the northwest corner is seen to undergo shearing of about 6% per day, whereas the entire part of the domain near shore is not deforming.

The stress states simulated during the eight-day period are presented in Figure 25. At each node point we have determined the stress state as the average value found in the surrounding nodes. The principal stress values are shown proportional to line length in the directions in which they occur. A line length of 1 cm represents a value of stress equal to the yield strength of 10^8 dyn cm^{-1}. While we cannot test the stress state by direct comparison with observations, we can learn at least to some extent whether the stress state is physically reasonable. For example, we see that during 28 January - 1 Feburary when ice is blown away from Banks Island that the stress is small in that region. This result is desirable since we expect little ice stress to arise in regions that are undergoing opening. Similarly, where the ice is being blown into a region the stress is seen to be larger (e.g., the western boundary on 30 January). However, we are not satisfied that principal values of stress in the center of the domain during 30 January are on the order of 5×10^7 dyn cm^{-1}. It is in this region that we have seen the leads opening in a generally north-south direction. We find it difficult to understand how stress may be transmitted across these leads in an east-west direction. We believe the shape of the yield surface must be modified to correct the stress state in this region. We have preliminary results of such a simulation using the triangular yield curve shown in Figure 26. Using the triangular yield curve allows the stress state to be uniaxial where plastic flow occurs. Preliminary results indicate that the principal values are aligned with the leads and a zero stress occurs normal to the leads. We further believe that the uniaxial opening deformation that is not observed in the present simulation (with a squished teardrop) will probably occur when the triangle yield surface is used. In summary, we find the stress fields to be reasonable except for one detail and we understand how that problem may be eliminated.

The force balance at each location provides important insights relating response to the driving forces. In Figure 27 we present the sequence of plots showing the forces acting at the node nearest the location of manned camp Caribou. In Figure 28 we present similar results for the node nearest the location of manned camp Blue Fox. The differences between the two plots depict spatial variations that occur between points that are about 150 km apart. During each day the results are similar but can vary by the order of 25 percent. In each plot of force balance we present the calculated ice drift as a dashed vector. The air stress $\underset{\sim}{\tau}_a$, water stress $\underset{\sim}{\tau}_w$, ice stress divergence $\underset{\sim}{f}_\sigma$ and Coriolis force $\underset{\sim}{f}_c$ are also shown. In addition, we show a vector $\underset{\sim}{E}$ that is required to sum forces to zero. It is composed of sea surface tilt, of inertia which is a measure of the lack of convergence to steady state conditions and of plotting errors on the order of 0.1 dyn cm^{-2}. During 30 and 31 January when winds and ice motion are highest, the force balance plots are especially useful. Since these two days are similar we concentrate on results of only one day--30 January.

We confine our further attention to the Figure 27 and consider results at Caribou because these may be checked directly with Figure 12. It should be noted that during 30 January (see Figure 2d) the observed motion of the two manned camps Caribou and Snow Bird appear to be about 20-30 degrees counterclockwise from other nearby points. This appears from satellite images to occur because the camps are on a large single floe that is surrounded by several leads and is rotating, Therefore, we do not want to be confused by this anomalous motion. The comparison between modeled and observed forces is reasonably accurate. Many of the differences can be explained. First, we have already shown (Figure 9) that the geostrophic air stress input to the model is about 20% too large. This is shown also in the force balance. It is a cause of a large difference between $\underset{\sim}{f}_\sigma$ and $\underset{\sim}{R}$ (we note that stress divergence should be the largest contributor to $\underset{\sim}{R}$) because a reduction of $\underset{\sim}{\tau}_a$ by 20% would cause

that vector difference to be subtracted from $\underset{\sim}{f}_{\sigma}$. Furthermore, the anomalous observed velocity of Caribou means that the modeled velocity is a better representation of large-scale motion than the motion measured at the camp. This observed velocity in turn is used to compute $\underset{\sim}{f}_{c}$ and $\underset{\sim}{\tau}_{w}$ in Figure 12. Rotating each clockwise would better align the "observed" forces with computed results. The water stress computed from observations neglects geostrophic ocean currents which are about 5 cm see-l in the direction of motion. This accounts for the fact that the water stress in Figure 12 is about twice as large as modeled. The consequence of this neglect of $\underset{\sim}{v}_{g}$ is to reduce $\underset{\sim}{R}$. Thus, halving $\underset{\sim}{\tau}_{w}$ automatically adds the vector difference to $\underset{\sim}{R}$ because $\underset{\sim}{R}(\equiv -\text{Is-}\ \underset{\sim}{\tau}_{w} - \underset{\sim}{f}_{c})$. Consideration of these three corrections to the "observed" force balance reduces the discrepancy to about 0.5 dyn cm^{-2}. In that case $\underset{\sim}{f}_{\sigma}$ and $\underset{\sim}{R}$ are aligned to within about 20°. This comparison is felt to be excellent considering the uncertainty in each of the many components.

SUMMARY

The AIDJEX model has been shown to provide a physically realistic simulation of the dynamic response of sea ice to winds during the winter when ice stress is significant. Furthermore, the motion is seen to compare extremely well with observed motions of buoys and manned camps. In the nearshore regions the plasticity model represents fast ice areas. These areas are separated from the moving pack ice by rapid variations or discontinuities. The location of the flaw lead agrees with satellite images. A close look at deformations and stress shows that we may improve some details of the response by changing the yield surface shape and we expect to pursue that work soon.

In addition to gaining a greater scientific understanding by studying the results of this simulation, we are a large step closer to answering a question of more immediate concern. That is, how can we relate the ice drift to given wind

conditions? We have shown that the AIDJEX model, including air, ice and ocean components, allows the large-scale ice drift to be determined. Thus, it is now possible to use the large set of historical winds data to drive a model and determine what ice drift occurs in the wide variety of conditions. Since the amount of ice drift data is very sparse, this provides a dramatic increase in our knowledge of ice trajectories.

Ice trajectories are not the only variables that become better known as a result of this modeling effort. The stress state in the ice cover is also important and our model also allows stress to be studied. The stress in the AIDJEX model is interpreted as the large-scale average of the forces that are transmitted between ice floes on the small scale. Although much work remains to relate the large-scale stress to forces that may be exerted on an individual ship or marine structure, we are sure that the large-scale stress is an indicator of relative size of those forces.

ACKNOWLEDGEMENTS

We thank R. T. Hall and A. S. Thorndike for help in preparing NOAA satellite images and manned camp motion data. In addition, the help of D. R. Thomas and L. Harris in making the computer calculations and graphics is appreciated.

REFERENCES

Arya, S. I'. S. 1975. A drag partition theory for determining the large-scale roughness parameter and wind stress on arctic pack ice. *AIDJEX Bull. No. 28*: *29-47.*

Brown, R. A. 1976. The resistance law. *AIDJEX Bull. No. 31*:21-31.

Carsey, F. D. and E. Leavitt. 1977. Pibal acoustic radar data measurements and computation of air stress over pack ice. To appear in *AIDJEX Bull.No.36.*

Coon, M. D., R. Colony, R. S. Pritchard and D. A. Rothrock. 1976. Calculations to test a pack ice model. In *Numerical methods in geomechanics*, Vol. II., ed. C. S. Desai, pp. 1210-1227. New York: American Society of Civil Engineers,

Coon, M. D., G. A. Maykut, R. S. Pritchard", D. A. Rothrock and A. S. Thorndike. 1974. Modeling the pack ice as an elastic-plastic material. *AIDJEX Bull. No. 24*:1-106.

Coon, M. D. and R. S. Pritchard. 1974. Application of an elastic-plastic model of arctic pack ice. In Coast *and Shelf of the Beaufort Sea,* ed. J. C. Reid and J. E. Sater, pp. *173-193.* Arlington, Virginia: Arctic Institute of North America.

Leavitt, E., D. Bell, M. Clarke, R. Andersen and C. Paulson. ***1977,*** Computations of air stress and sensible heat fluxes from surface layer profile data. AIDJEX *1975.* To appear in *AIDJEX Bull.No.36.*

Pritchard, R. S. 1975. An elastic-plastic constitutive law for *sea* ice. *Journ. Appl. Mech.*, Vol. *42,* No.2:379-384.

_____. *1977.* An estimate of the strength of arctic pack ice. *AIDJEX Bull. No. 34*:94-113.

Pritchard, R. S. and R. Colony. 1976. A difference scheme for the AIDJEX sea ice model. In *Numerical methods in geomechanics*, Vol. II, ed. C. S. Desai, pp. 1194-1209. New York: American Society of Civil Engineers.

Pritchard, R. S., M. D. Coon and M. G. McPhee. 1977. Simulation of sea ice dynamics during AIDJEX. *AIDJEX Bull. No. 34*:73-93.

Thorndike, A. S. and J. Y. Cheung. 1977. AIDJEX measurements of sea ice motion, 11 April 1975 to 14 May 1976. *AIDJEX Bull. No. 35*:1-149.

TABLE 1. MODEL PARAMETERS FOR VARIOUS SIMULATIONS

Parameter		Run Identifier		
Name	Symbol (Units)	Run 3B	Run 3C	Run 3D
Strength	p^* (dyn cm^{-1})	10^7	10^8	10^9
Bulk Modulus	M_1 (dyn cm^{-1})	0.5×10^{10}	0.5×10^{11}	0.5×10^{12}
Shear Modulus	M_2 (dyn cm^{-1})	0.25×10^{10}	0.25×10^{10}	0.25×10^{12}
Time Step	Δt (see)	*300*	*120*	*40*
Mean Thickness	m (gm cm^{-2})	*300*	*300*	*300*

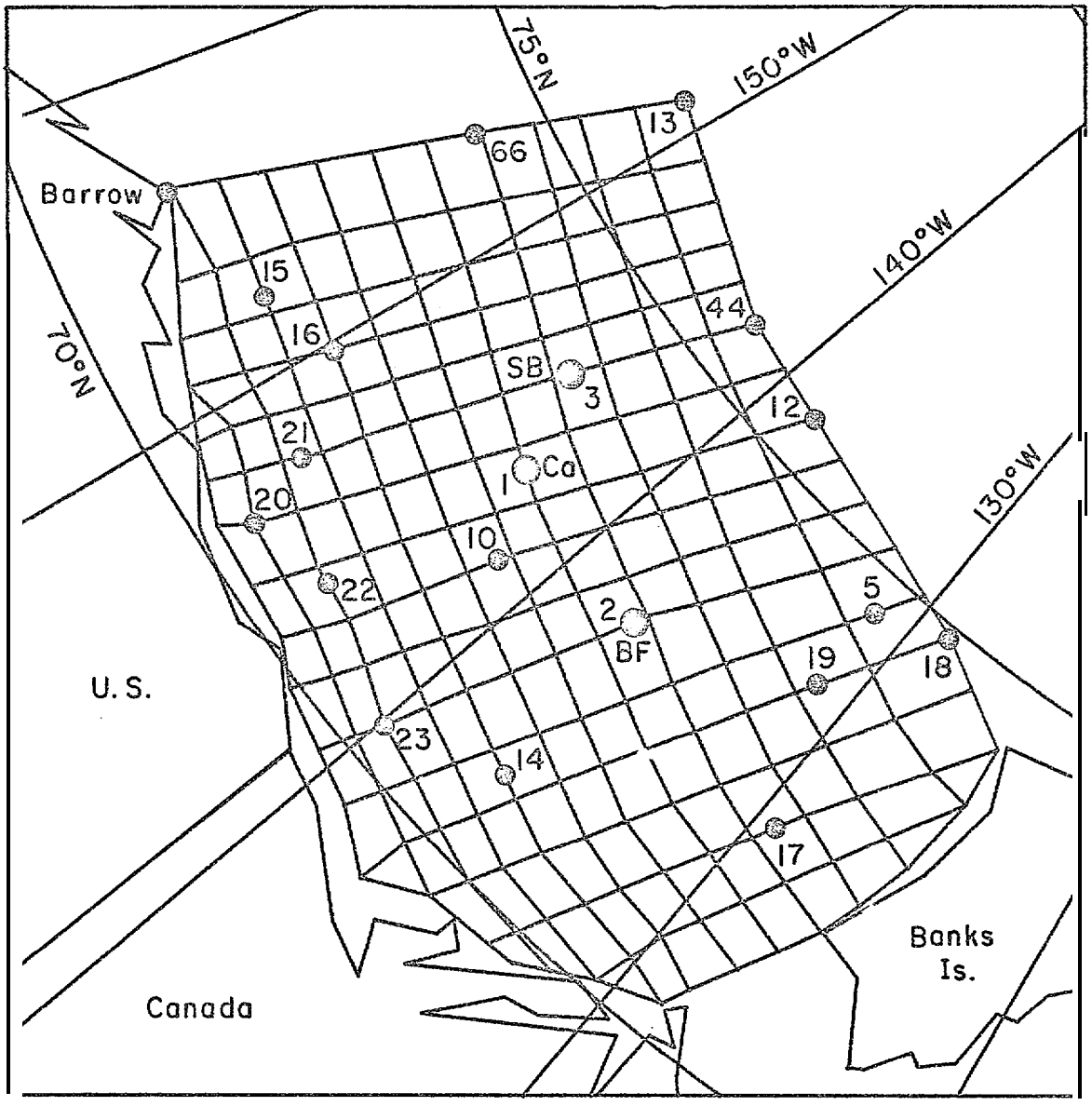

Figure 1. Numerical Grid with Manned Camp and Buoy Locations. Station numbers are consistent with Throndike and Cheung (Appendix 1). Manned camps are identified with the following station numbers: 1 - Caribou; 3 – Snow Bird; 2 - Blue Fox.

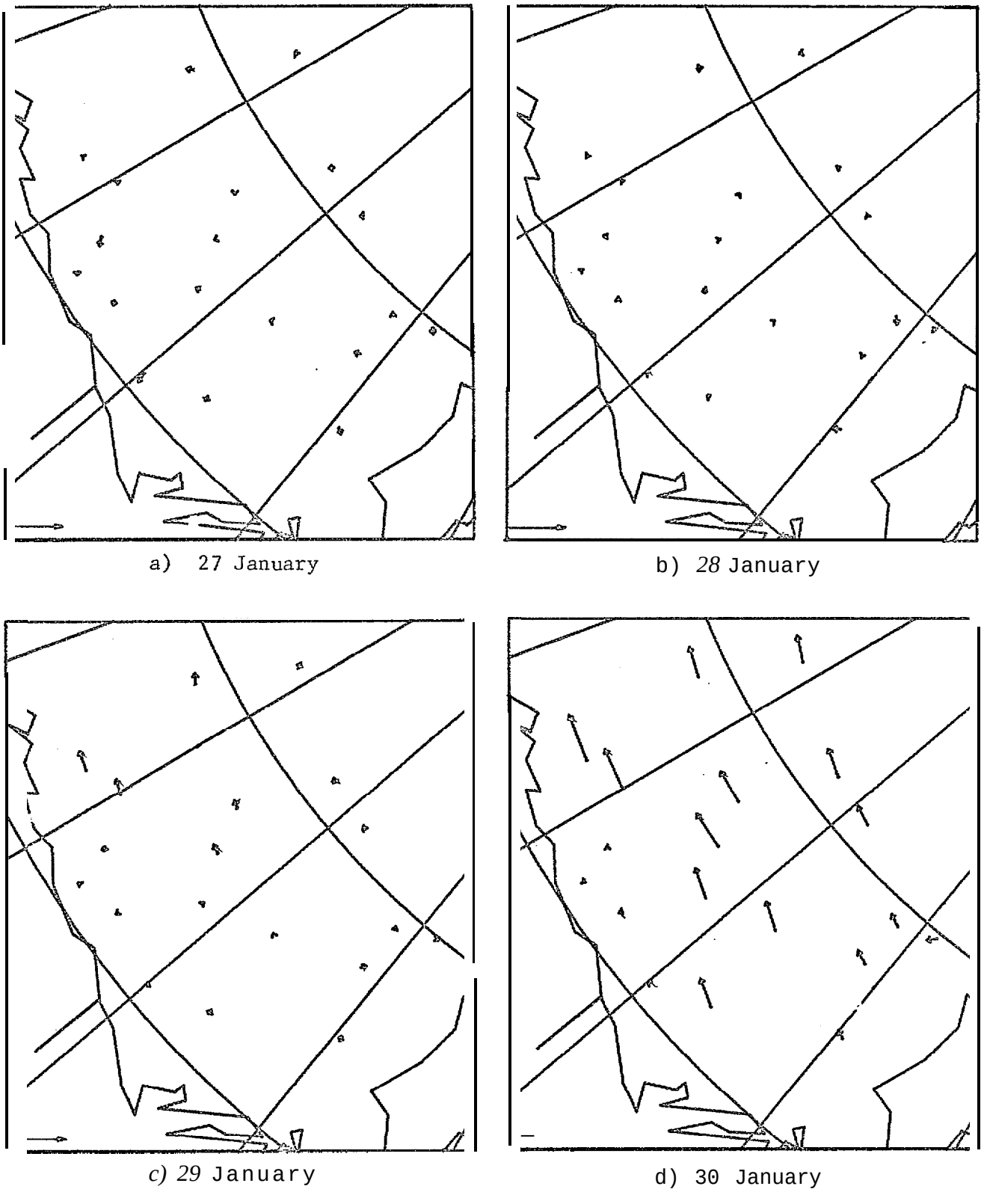

a) 27 January

b) *28* January

c) 29 January

d) 30 January

Figure 2. Daily Averages of Data Buoy and Manned Camp Velocities. Scale vector *is 25* cm see–'. The U.S. and Canadian coastline compares with the model boundary.

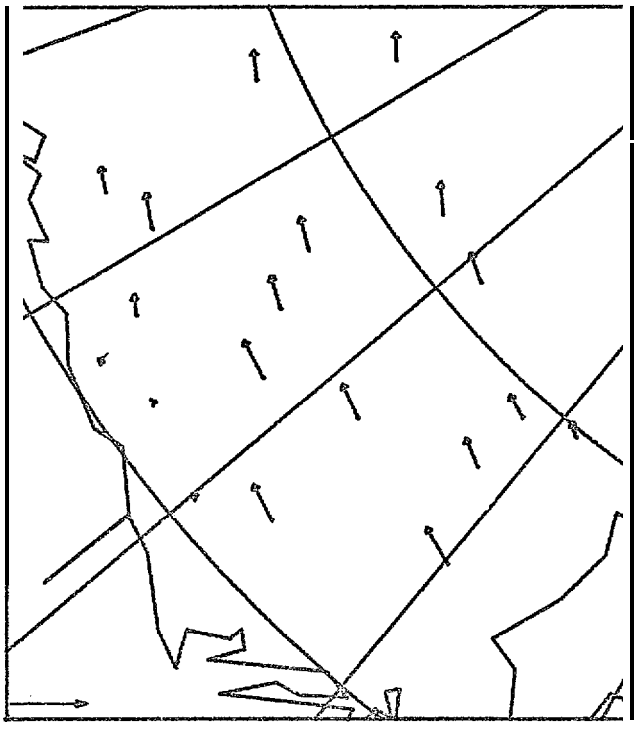

e) 31 January

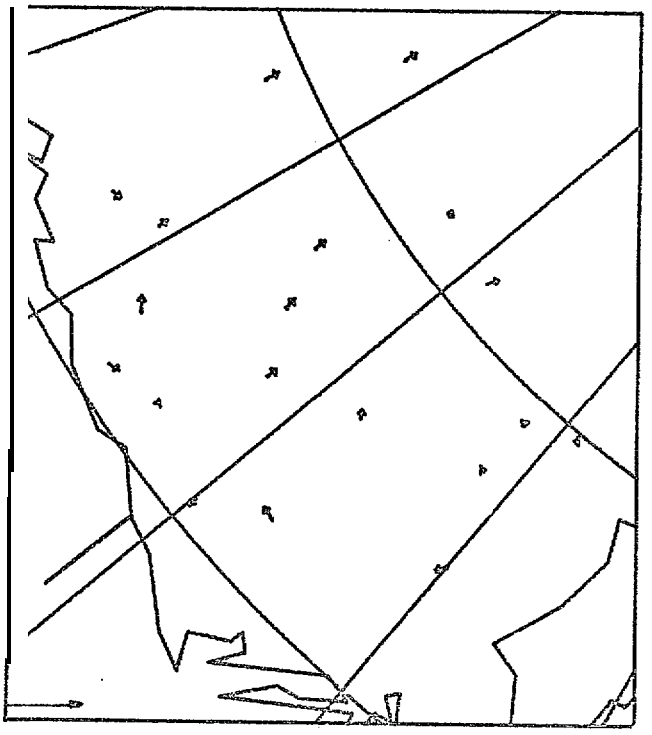

f) 1 February

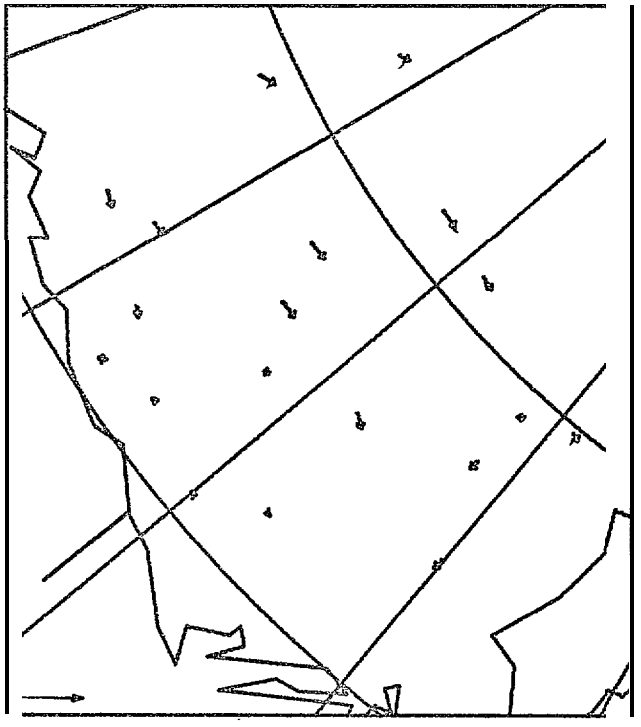

g) 2 February

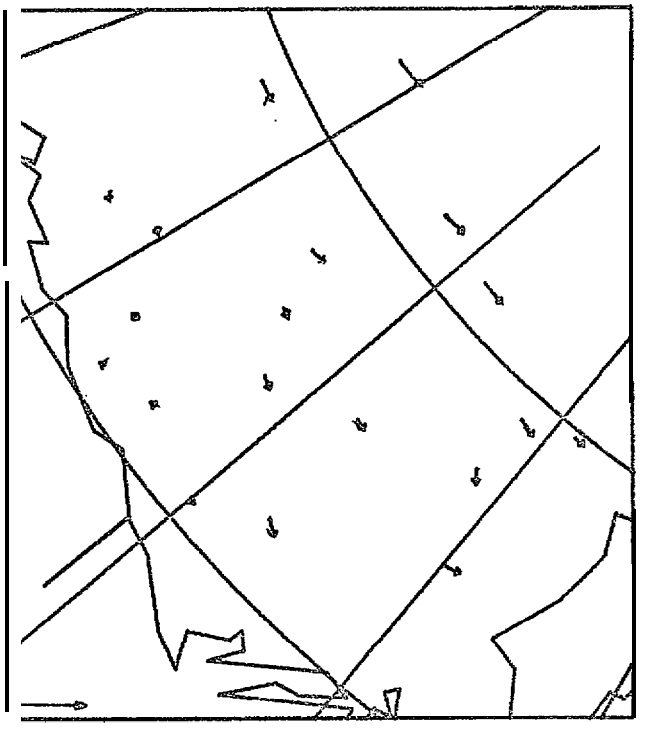

h) *3* February

Figure 2. (cent.) Daily Averages of Data Buoy and Manned Camp Velocities. Scale vector is 25 cm see-l. The U.S. and Canadian coastline compares with the model boundary.

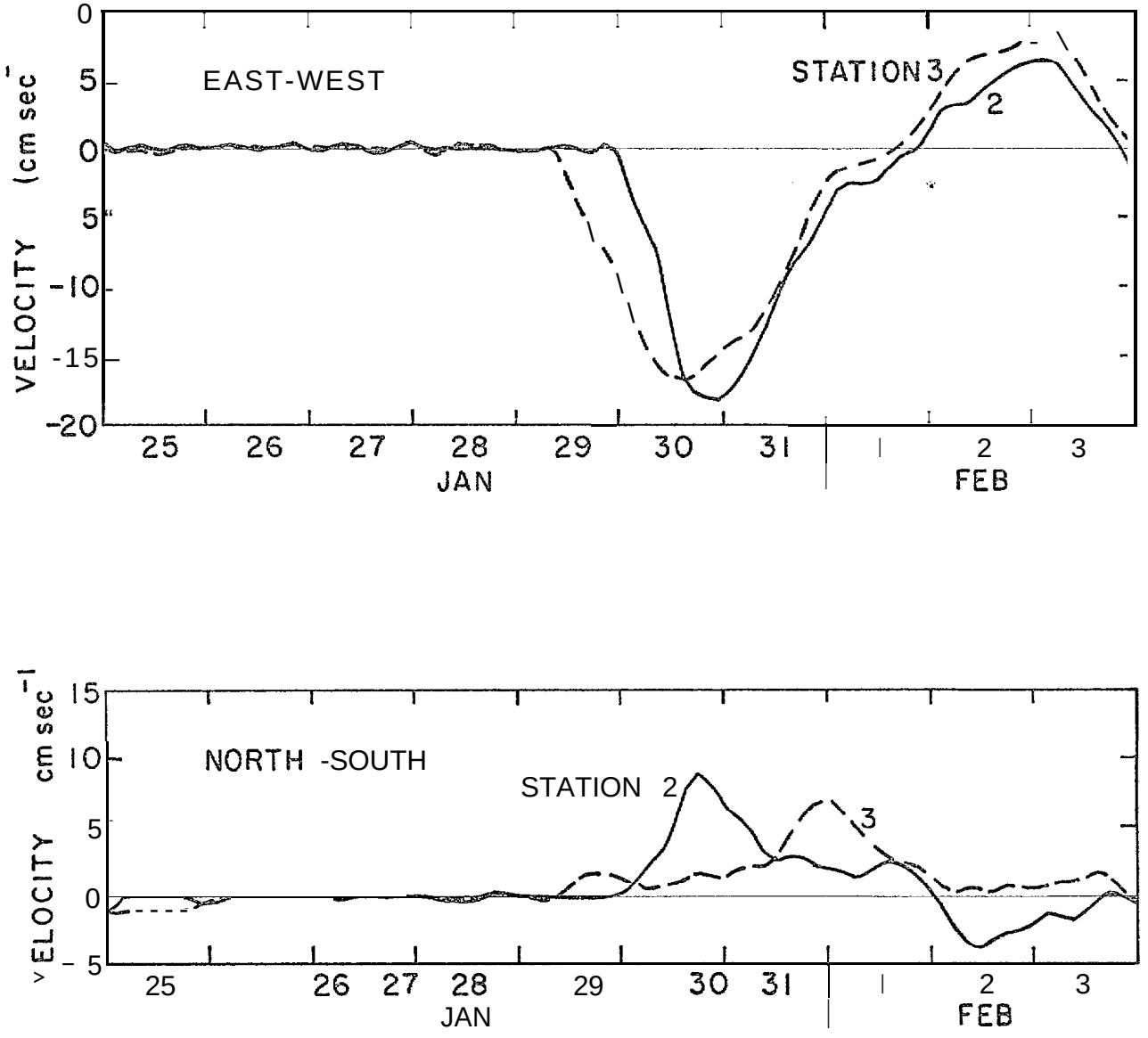

Figure 3. Time History of Observed Velocity from Data Buoysat Stations 3 (Snow Bird) and2 (Blue Fox). Components at each location are east and north.

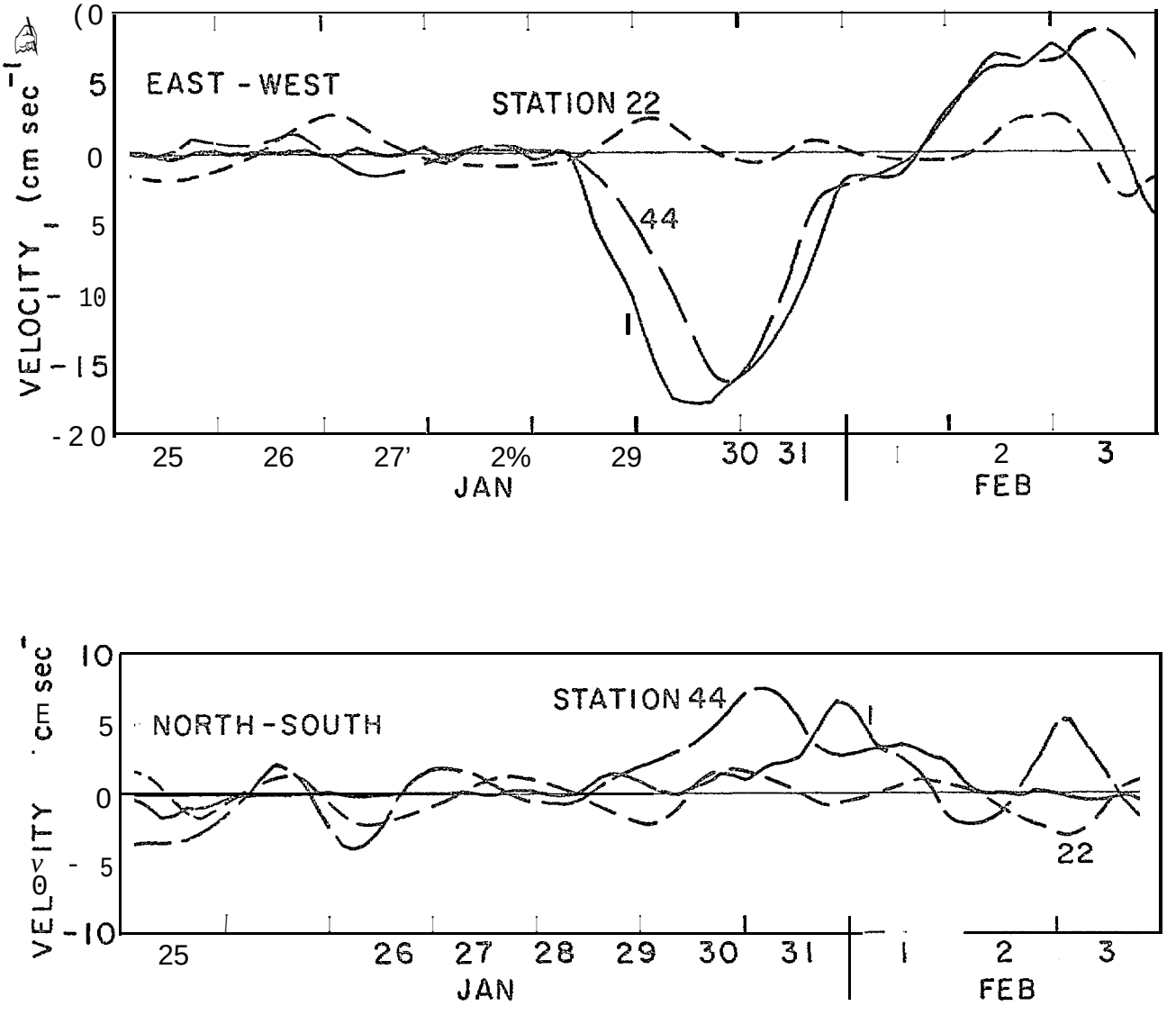

Figure 4. Time History of Observed Velocity from Data Buoys at Stations 1 (Caribou), 22 and 44. Components at each location are east and north.

Figure 5. Reproduction of NOAA 4, IR-VHRR Images (orbit number 5487, frames I1F0001 and I2F2238) Covering the Simulation Region on 27 January 1976 at Approximately 2100 GMT. The boundary of the numerical grid (Figure 1) is shown. Triangles and circles indicate locations of manned camps and data buoys, respectively.

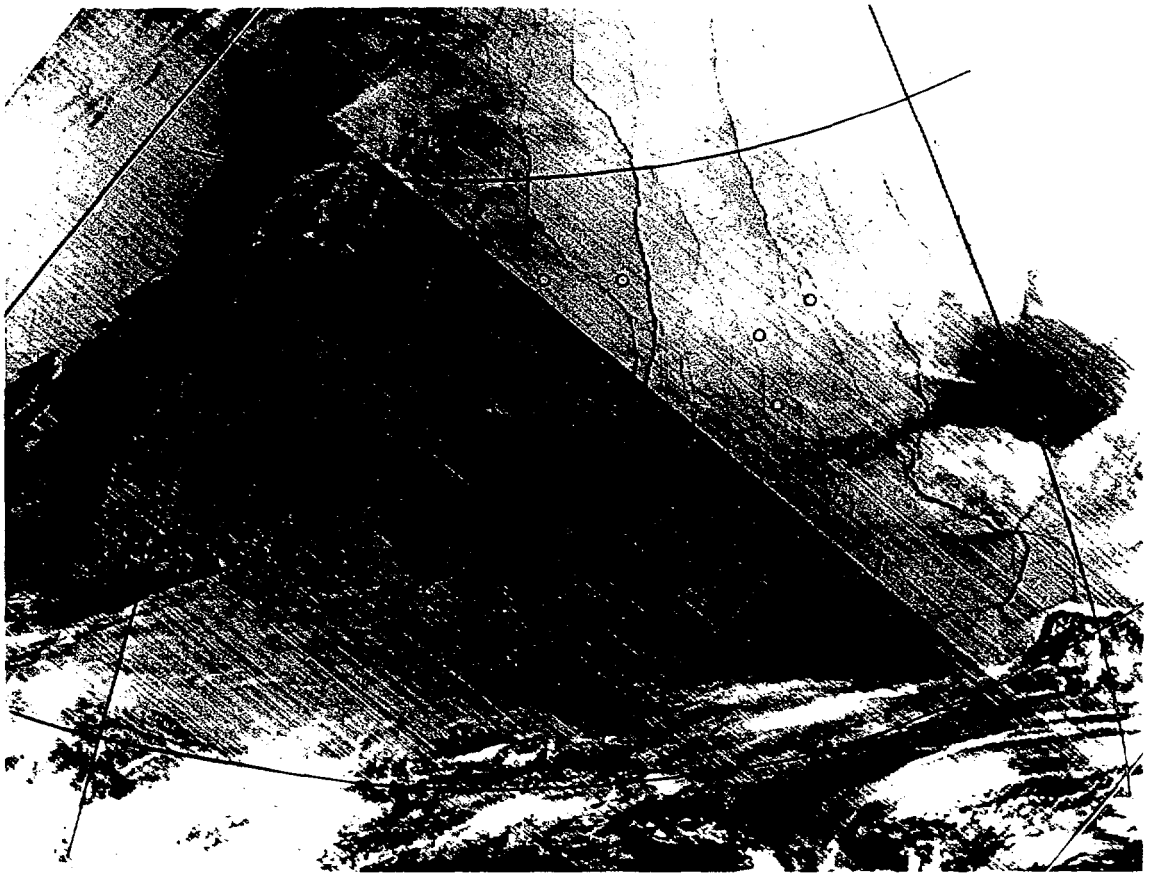

Figure 6. Reproduction of NOAA 4, IR-VHRR Images (orbit number 5524, frames I1F0001 and I2F2238) Covering the Simulation Region on 30 January 1976 at Approximately 2100 GMT. Triangles and circles indicate locations of manned camps and data buoys, respectively.

Figure 7. Reproduction of NOAA 4, IR-VHRR Images (orbit number 5549, frames I1F0001 and I2F2238) Covering the Simulation Region on 1 February 1976 at Approximately 2100 GMT. Triangles and circles indicate locations of manned camps and data buoys, respectively.

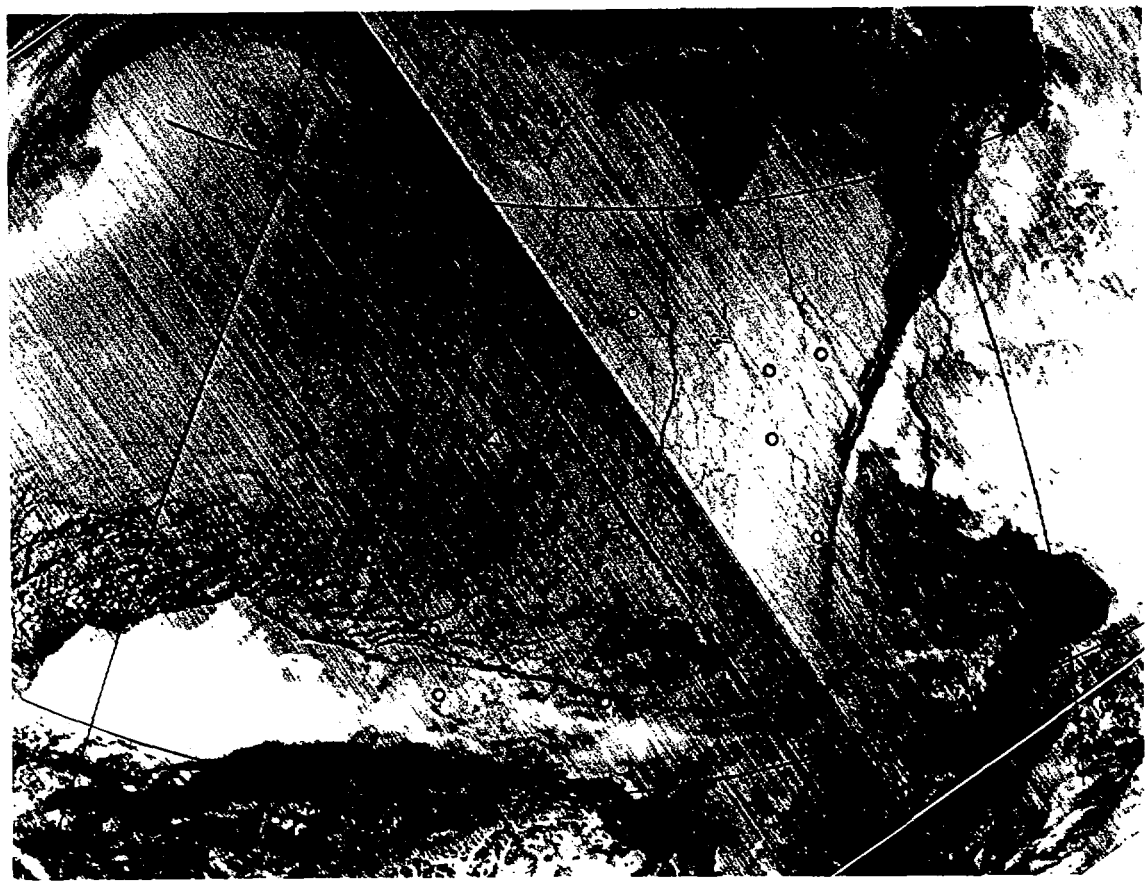

Figure 8. Reproductions of NOAA 4, IR-VHRR Images (orbit number 5562, frames 11F0001 and 12F2238) Covering the Simulation Region on 2 February 1976 at Approximately 2100 GMT. Triangles and circles indicate locations of manned camps and data buoys, respectively.

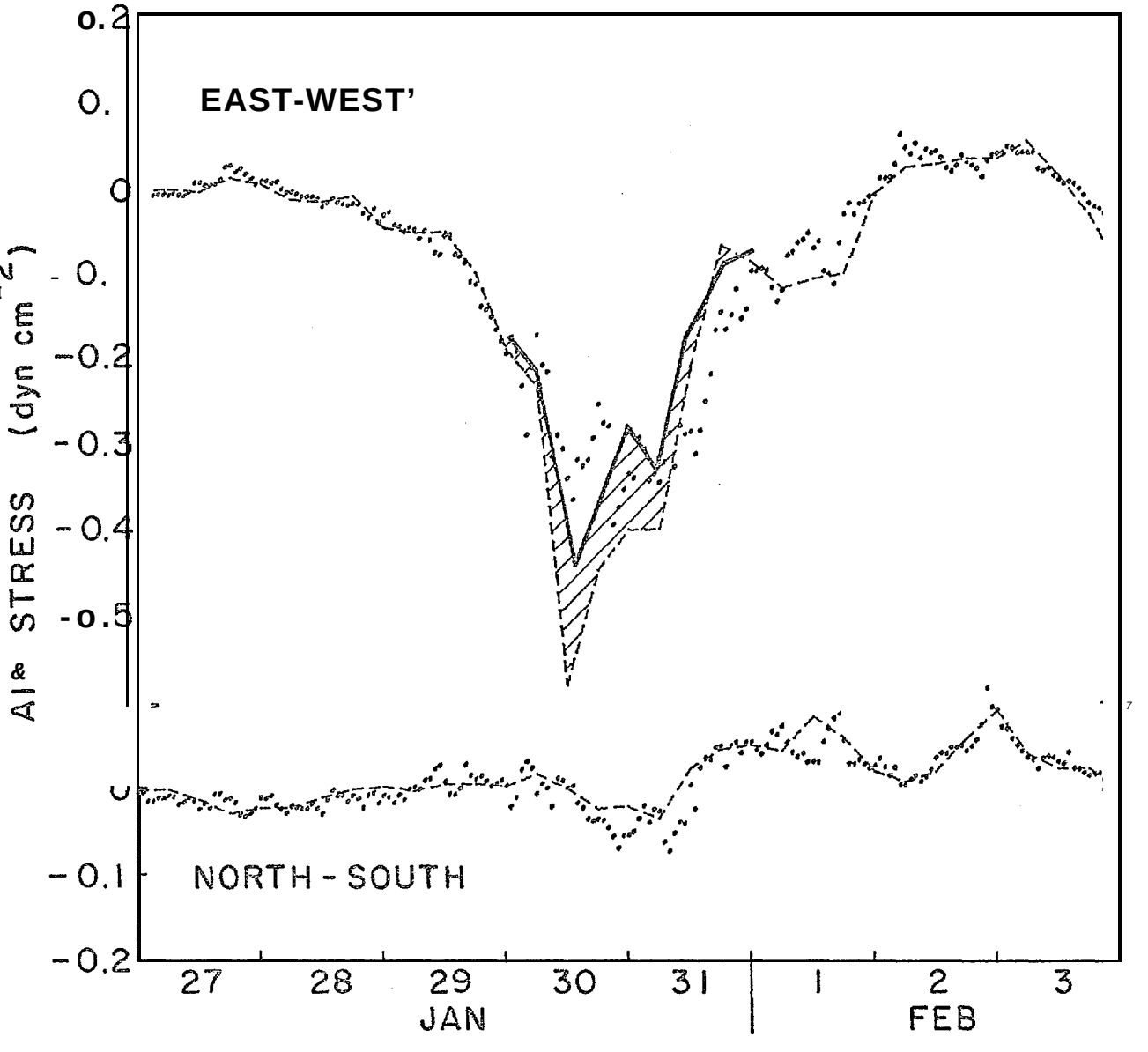

Figure 9. Air Stress Time History at Station 1 (Caribou). Components are shown in east and north directions. The dotted lines (...) represent the best estimate from 10-meter winds, while the dashed lines (---) represent values from geostrophic winds. The latter are linearly interpolated between data points each six hours. The bold line (——) represents modified values after barometric pressures were corrected.

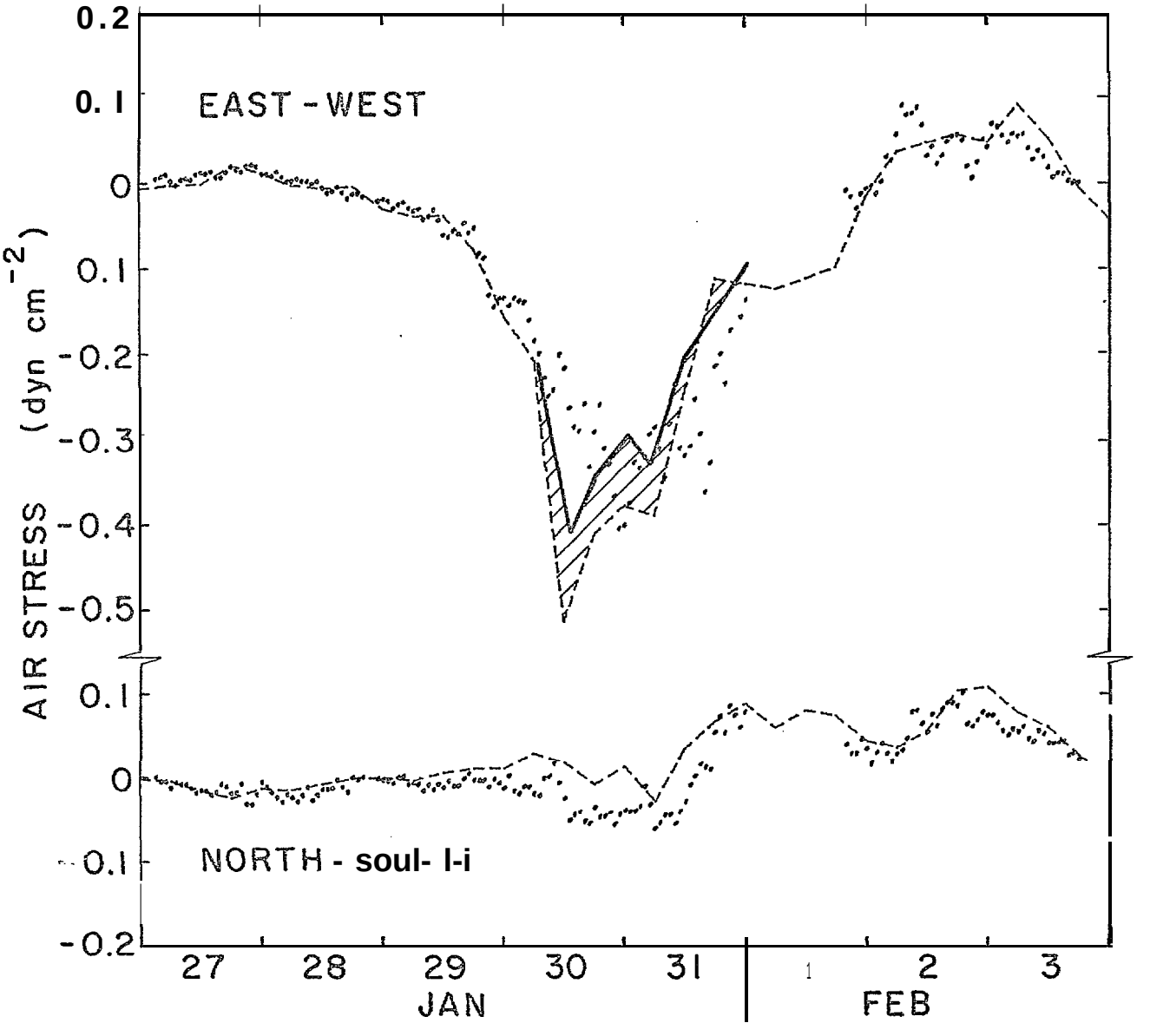

Figure 10. Air Stress Time History at Station 3 (Snow Bird). Components are shown in east and north directions. The dotted lines (...) represent the best estimate from 10-meter winds, while the dashed lines (---) represent values from geostrophic winds. The latter are linearly interpolated between data points each six hours. The bold line (——) represents modified values after barometric pressures were corrected.

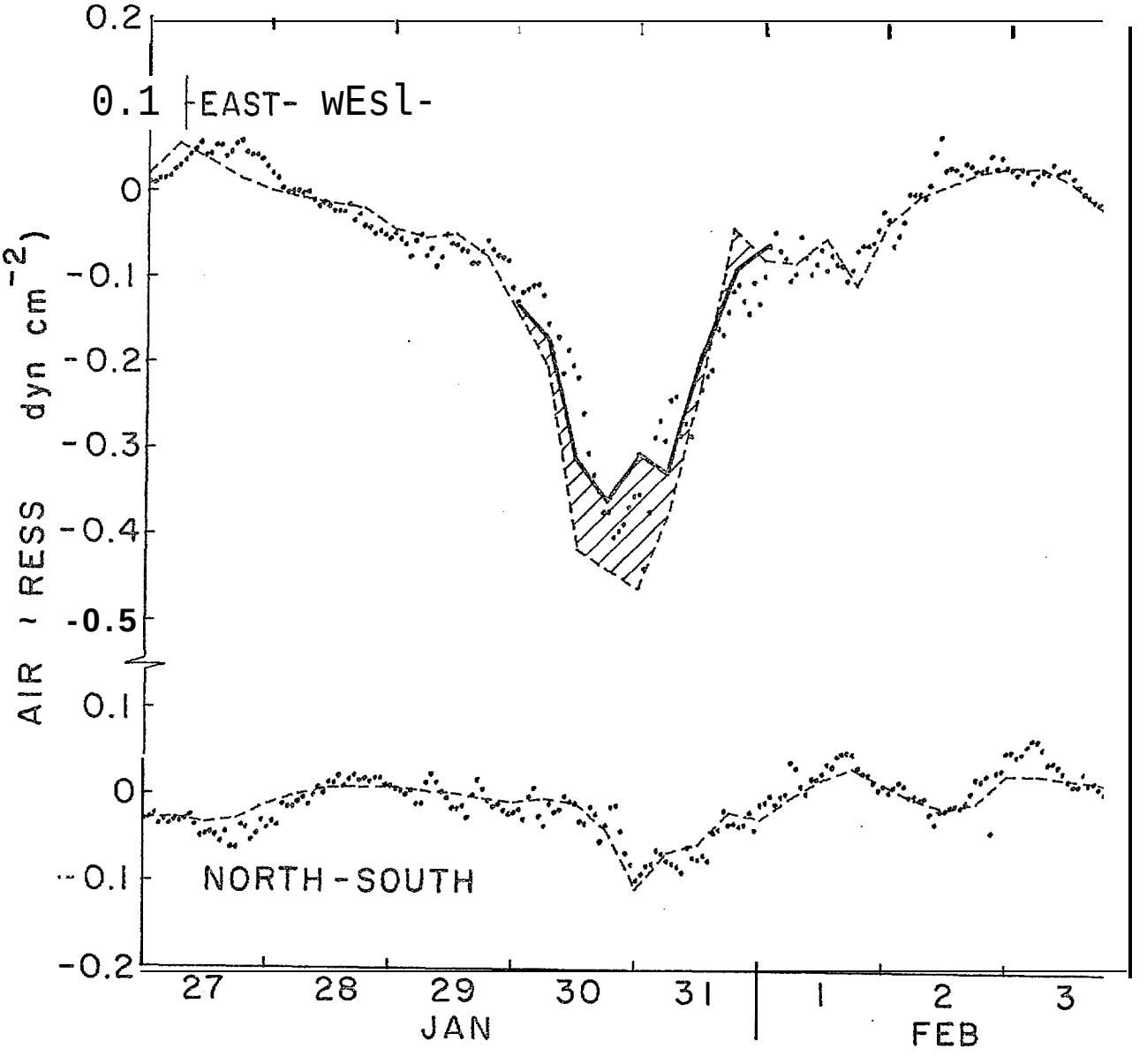

Figure 11. Air Stress Time History at Station 2 (Blue Fox). Components are shown in east and north directions. The dotted lines (...) represent the best estimate from 10-meter winds, while the dashed lines (---) represent values from geostrophic winds. The latter are linearly interpolated between data points each six hours. The bold line (——) represents modified values after barometric pressures were corrected.

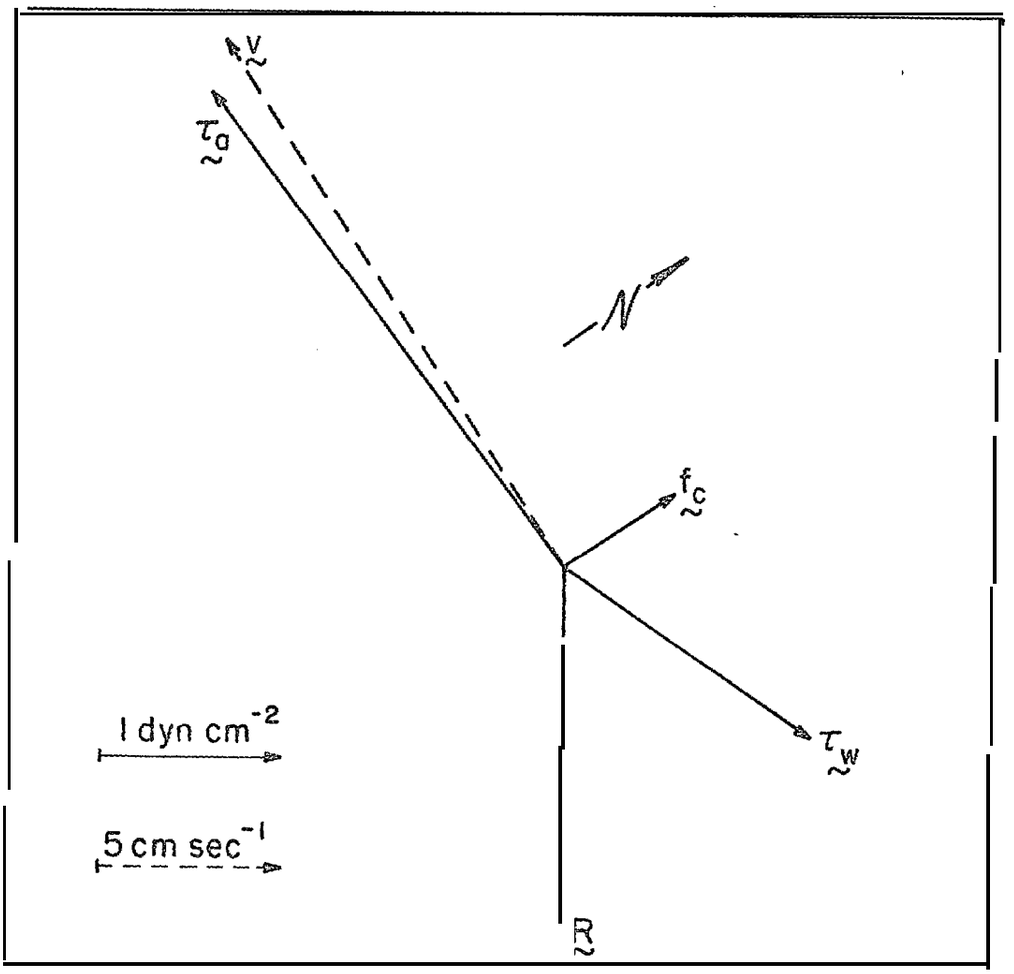

Figure 12, Force Balance at Station 1 (Caribou) at 1200 GMT on 30 January.

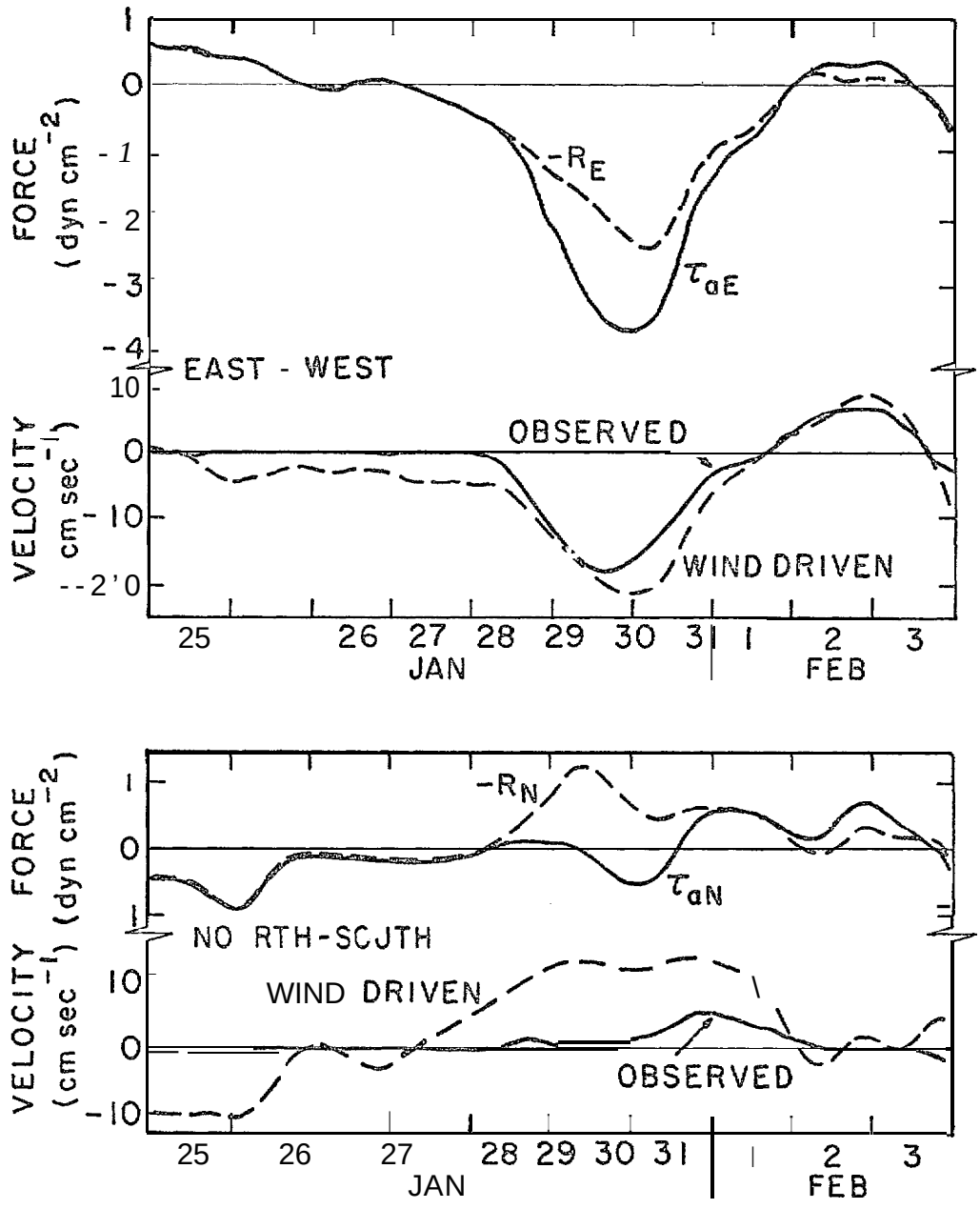

Figure 13. Time History of Driving Forces and Resulting Velocity at Station 1 (Caribou). Components are given in geographic coordinates. Subscript E and N indicate positive values of the component to the east and north, respectively. Air stress $\underset{\sim}{\tau}_a$ and the residual $\underset{\sim}{R}$ (composed largely of ice stress divergence) are shown as are the observed and wind-driven velocities.

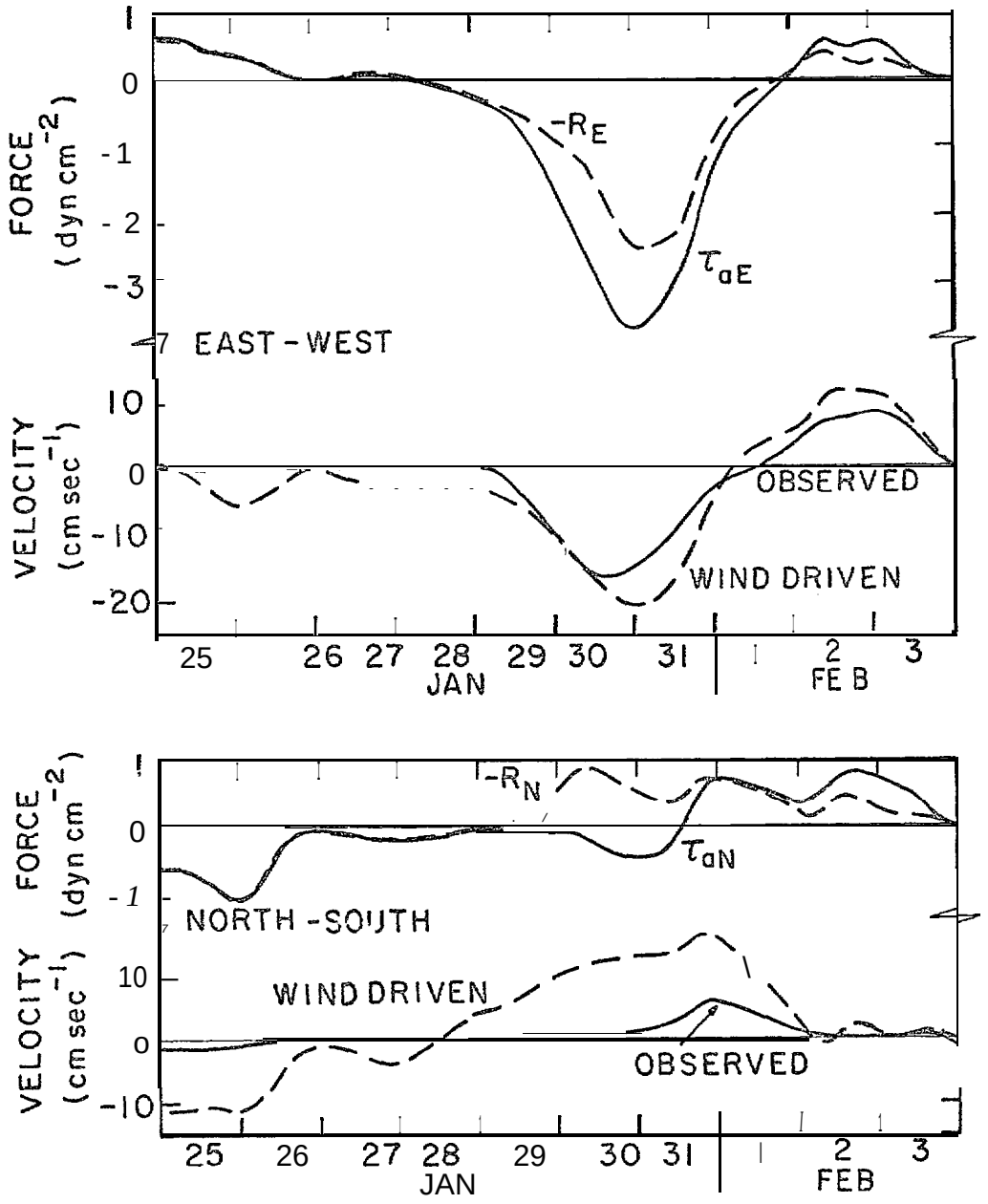

Figure 14. Time History of Driving Forces and Resulting Velocity at Station 3 (Snow Bird). Components are given in geographic coordinates. Subscript E and N indicate positive values of the component to the east and north, respectively. Air stress τ_a and the residual $\vec{R}$ (composed largely of ice stress divergence) are shown as are the observed and wind-driven velocities.

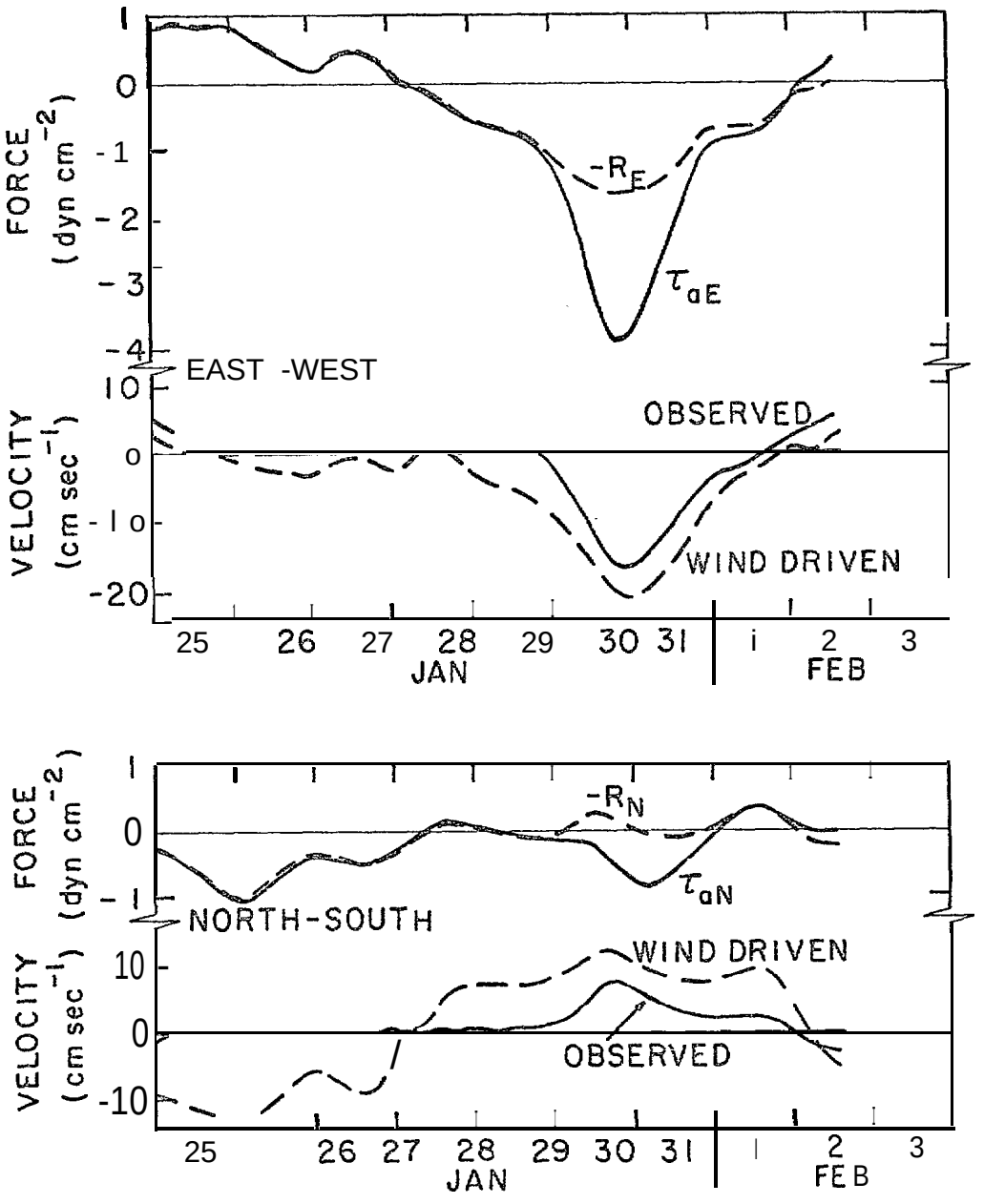

Figure 15. Time History of Driving Forces and Resulting Velocity at Station 2 (Blue Fox). Components are given in geographic coordinates. Subscript E and N indicate positive values of the components to the east and north, respectively. Air stress $\underset{\sim}{\tau}_a$ and the residual $\underset{\sim}{R}$ (composed laregly of ice stress divergence) are shown as are the observed and wind-driven velocities.

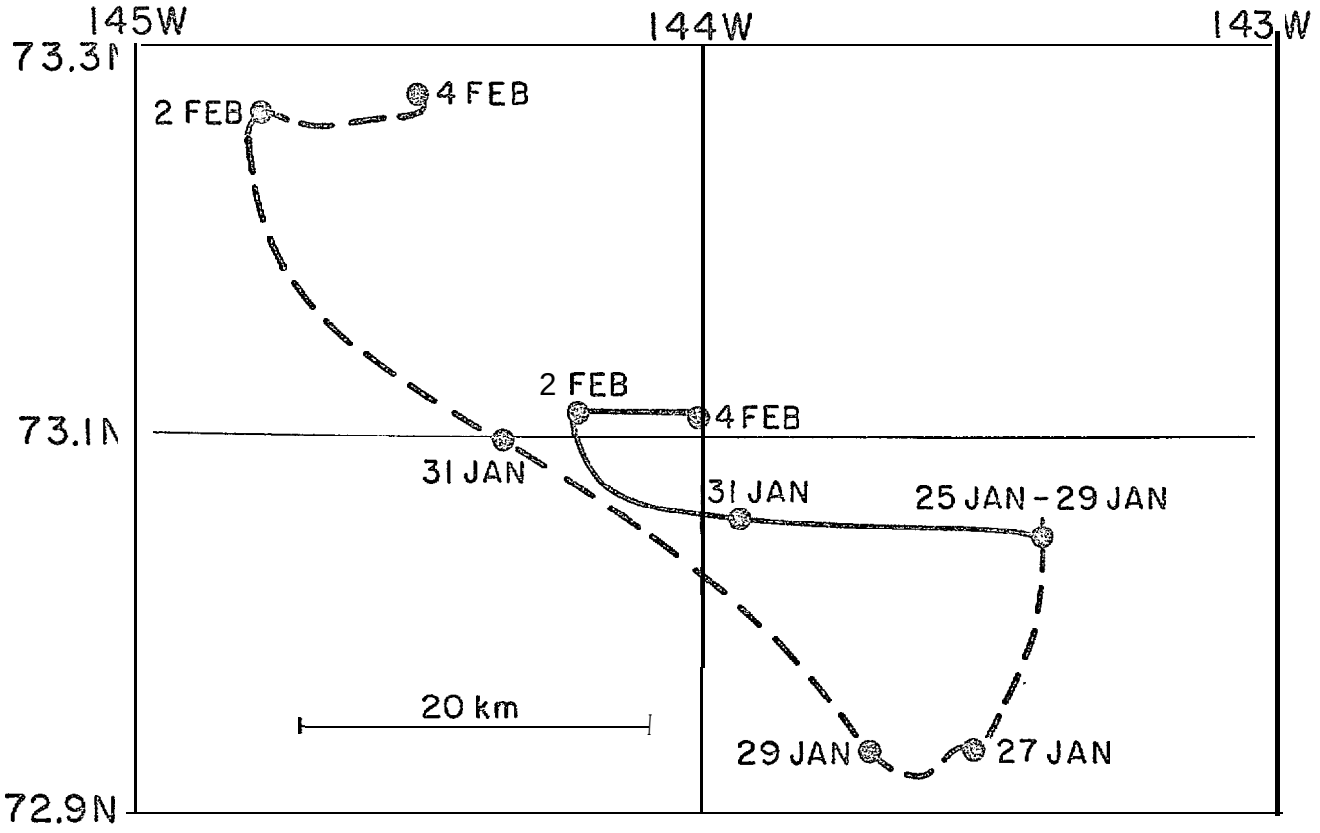

Figure 16. Trajectory of Station 1 (Caribou). Observed drift track shown as (——) and wind-driven shown as (---). Circles indicate location on indicated data at 0000 GMT.

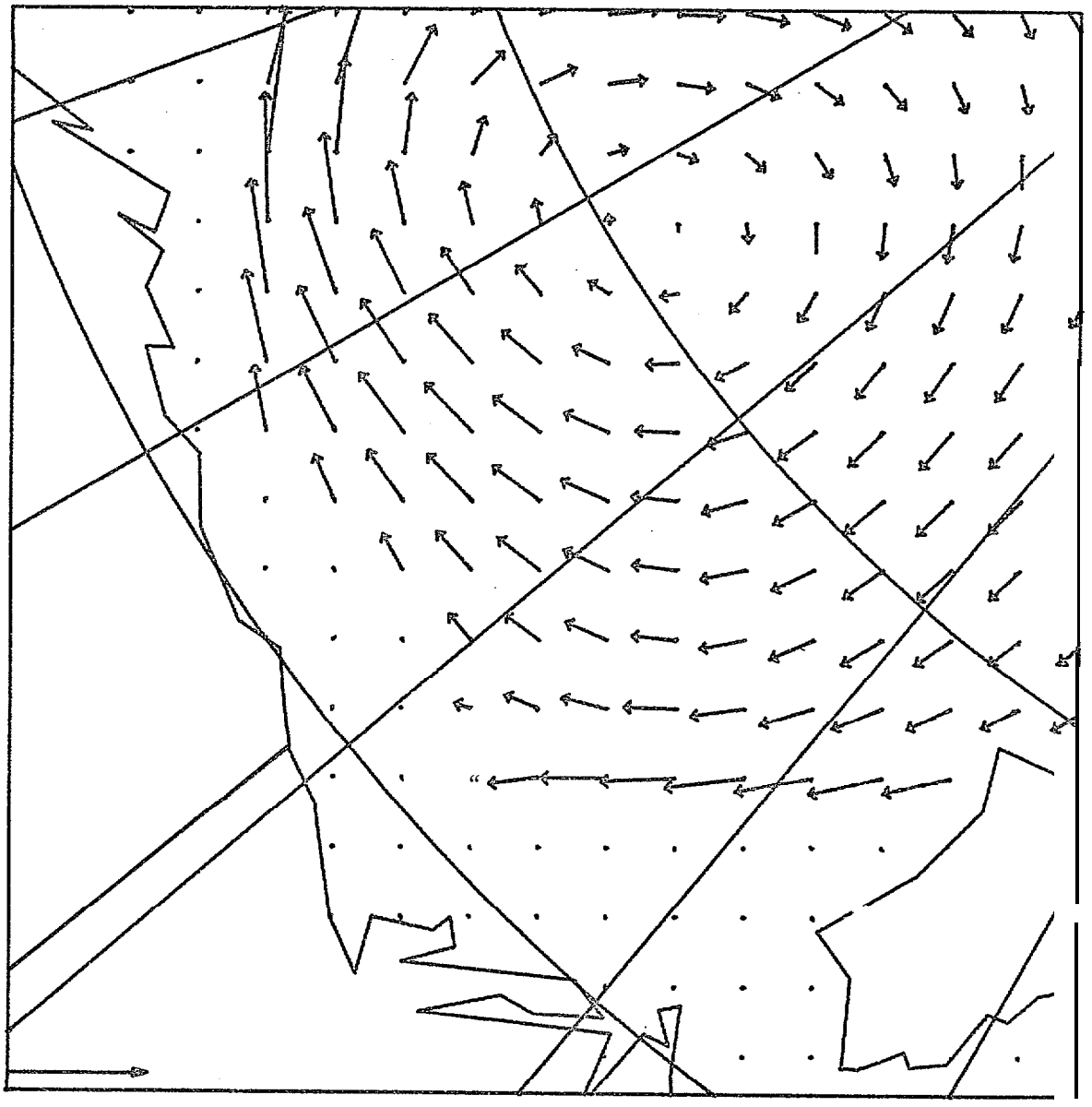

Figure 17. Geostrophic Ocean Current from Long-TermDynamic Topography. Scale arrow is 10 cm see-l. Dots represent zero current.

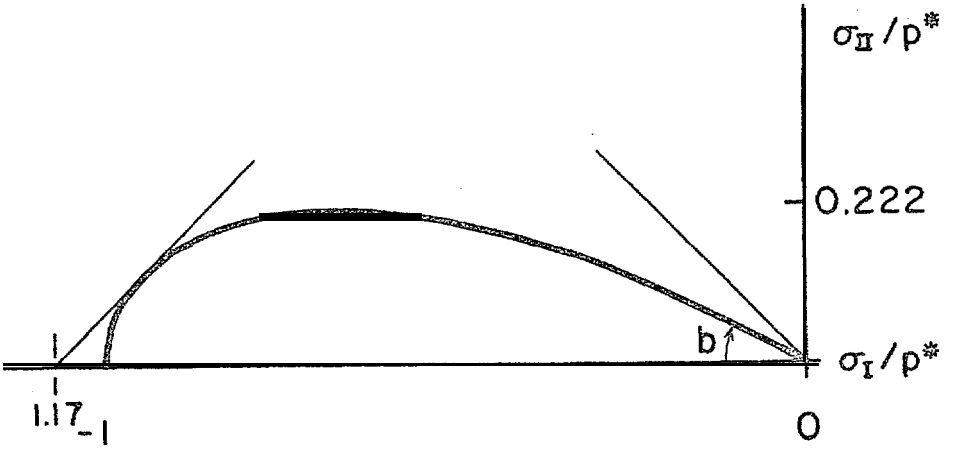

Figure 18. Squished Teardrop Yield Curve.

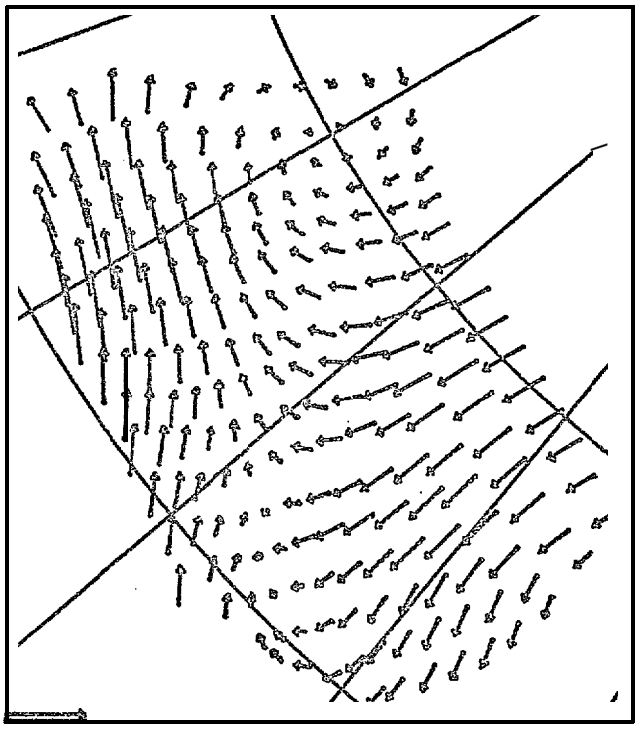

a) 27 January

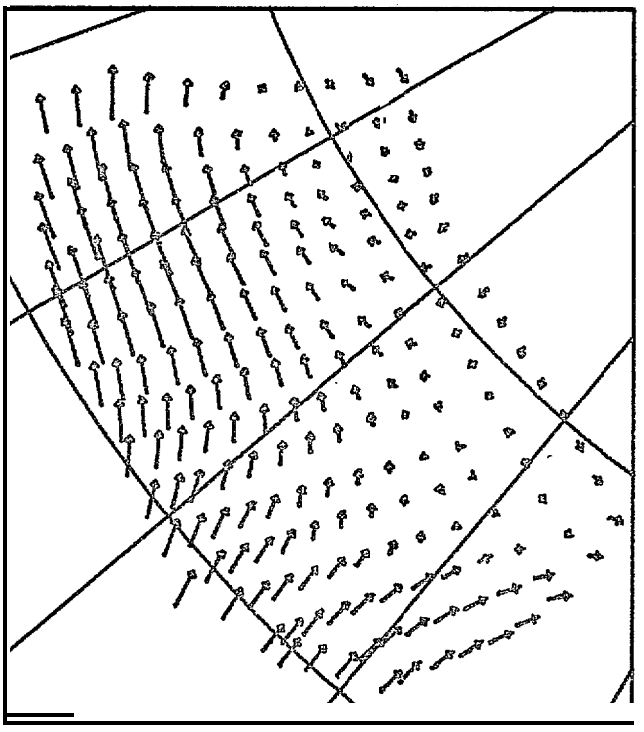

b) 28 January

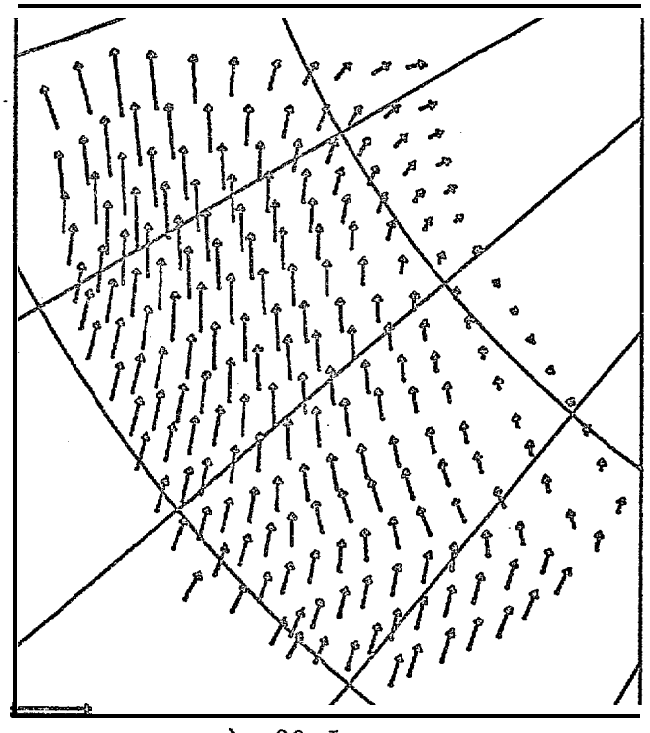

c) 29 January

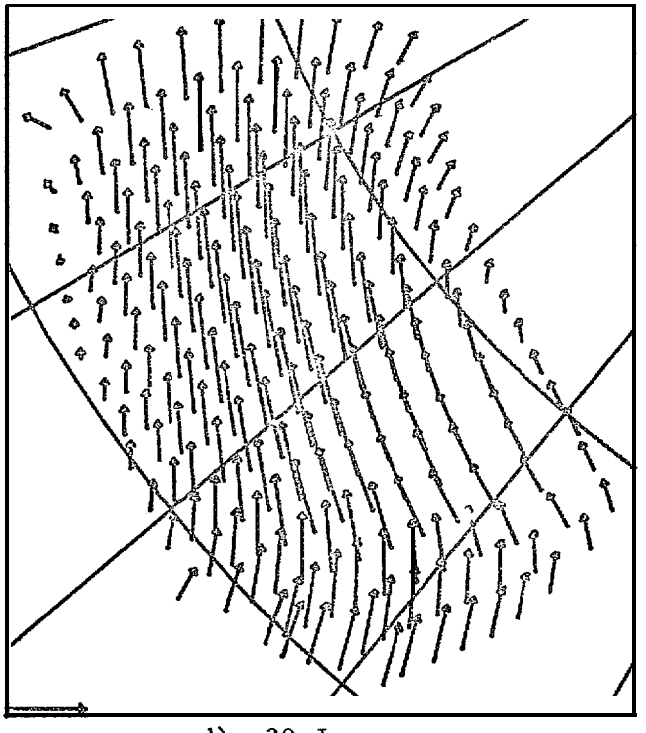

d) 30 January

Figure 19. Wind-Driven (Free-Drift Ice Velocity. Scale vector is 25 cm sec^{-1}.

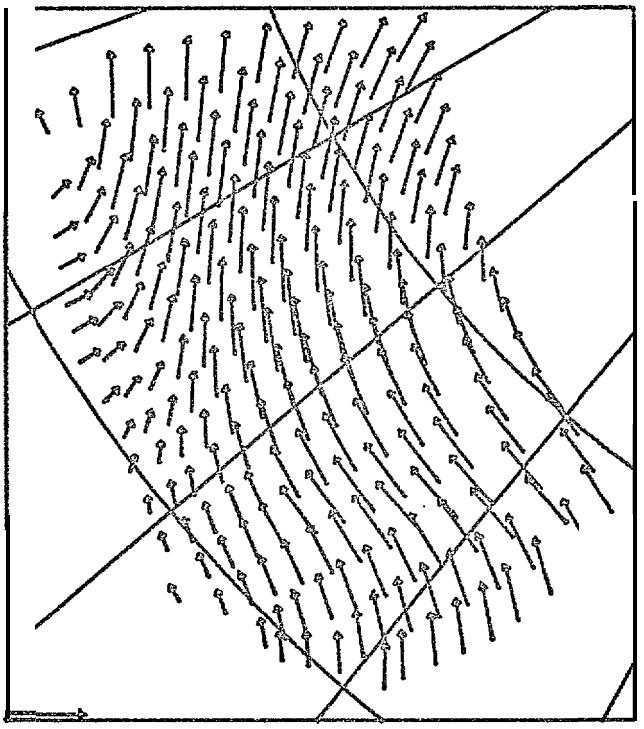

e) 31 January

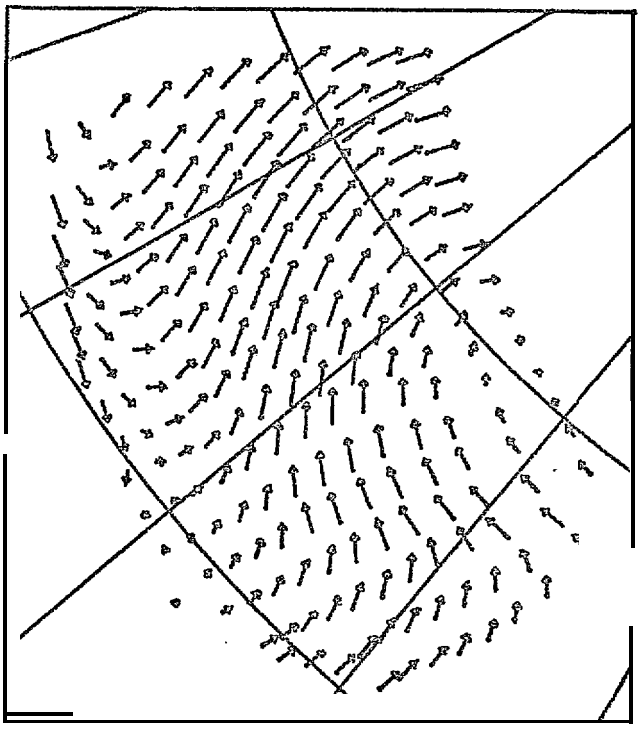

f) 1 February

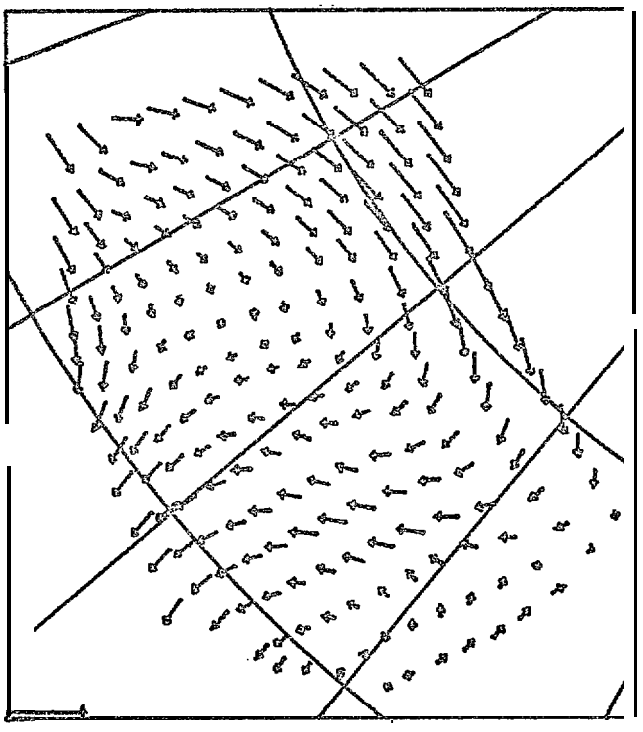

g) 2 February

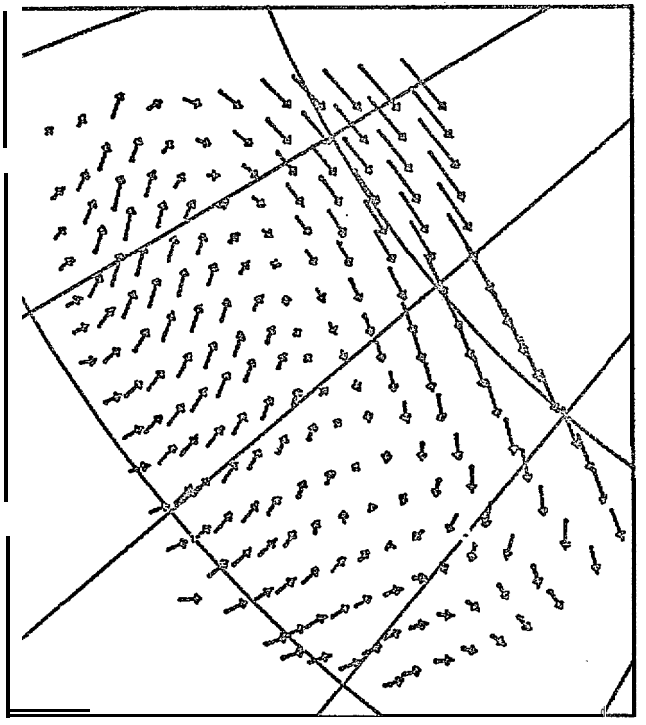

h) 3 February

Figure 19. (cent.) Wind-Driven (Free-Drift) Ice Velocity. Scale vector is 25 cm sec^{-1}.

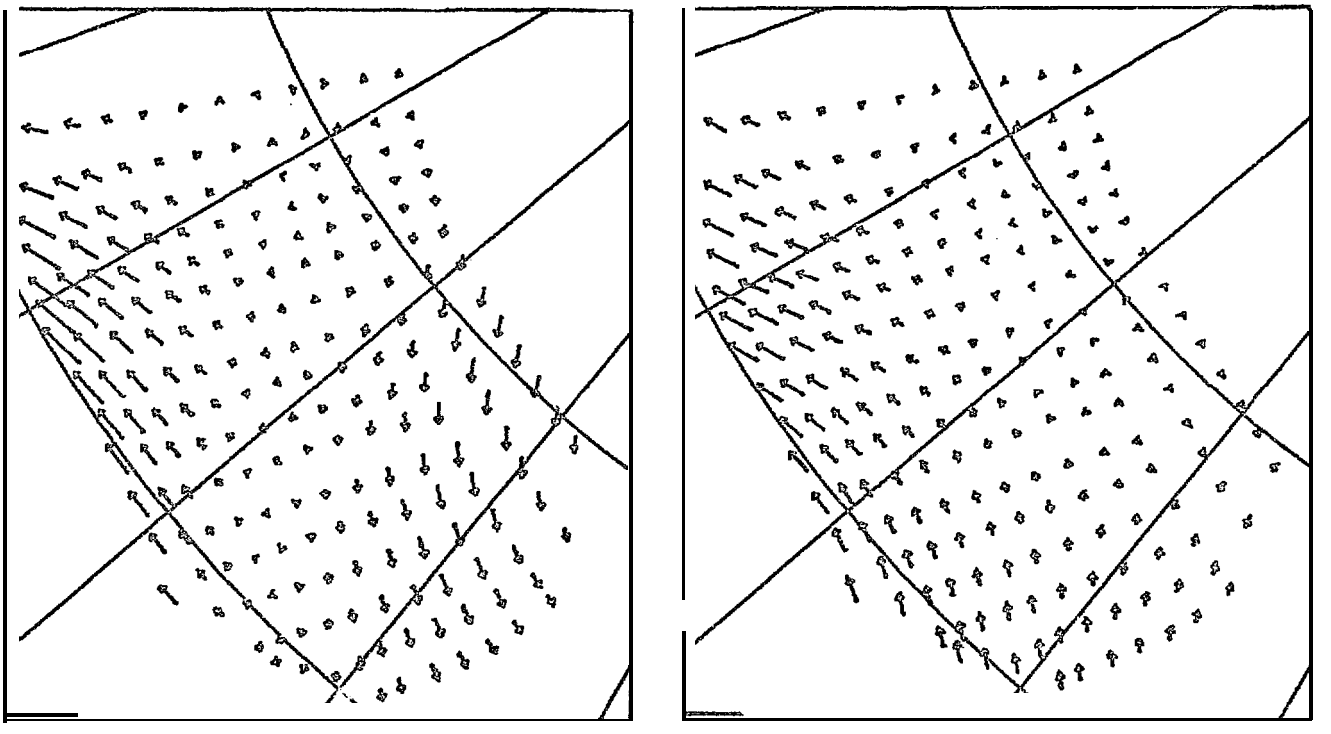

a) " *27* January

b) ***28*** January

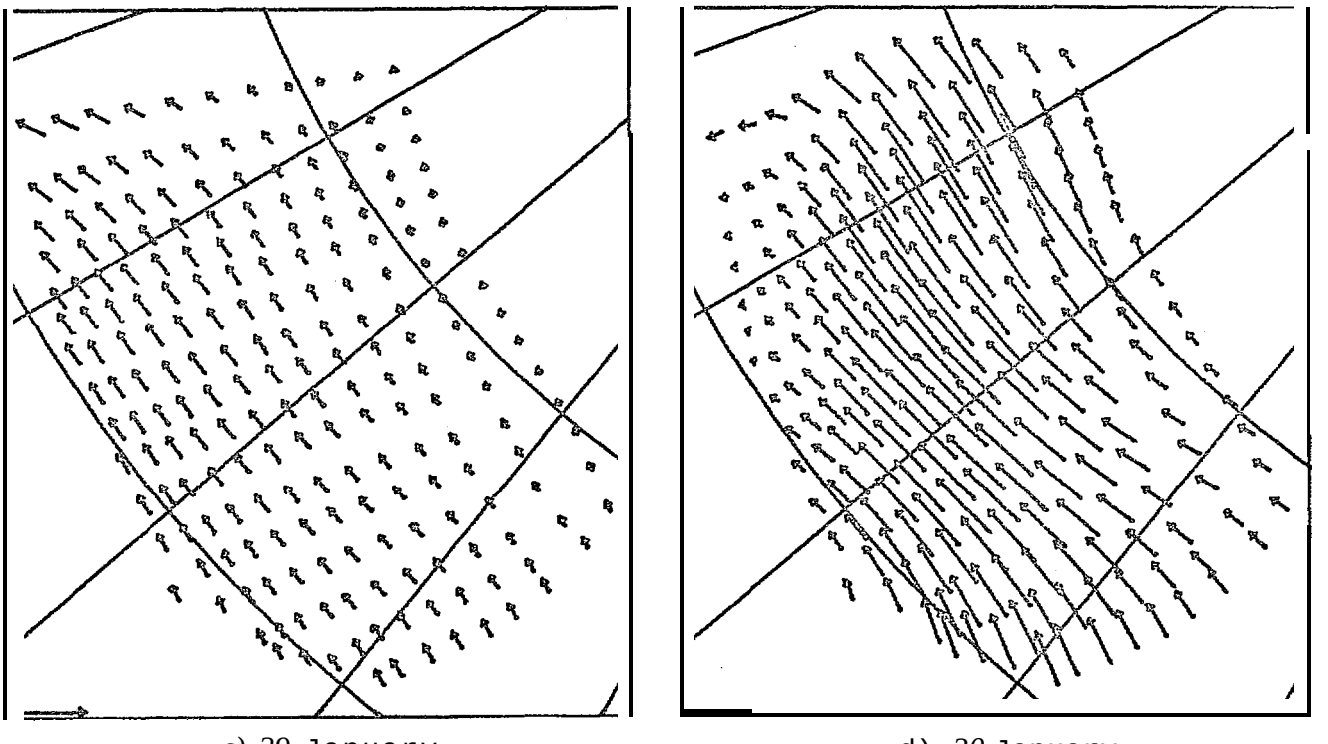

c) 29 January

d) *30* January

Figure 20. Daily Average of Air Stress Field. Scale vector is 4 dyn cm^{-1}.

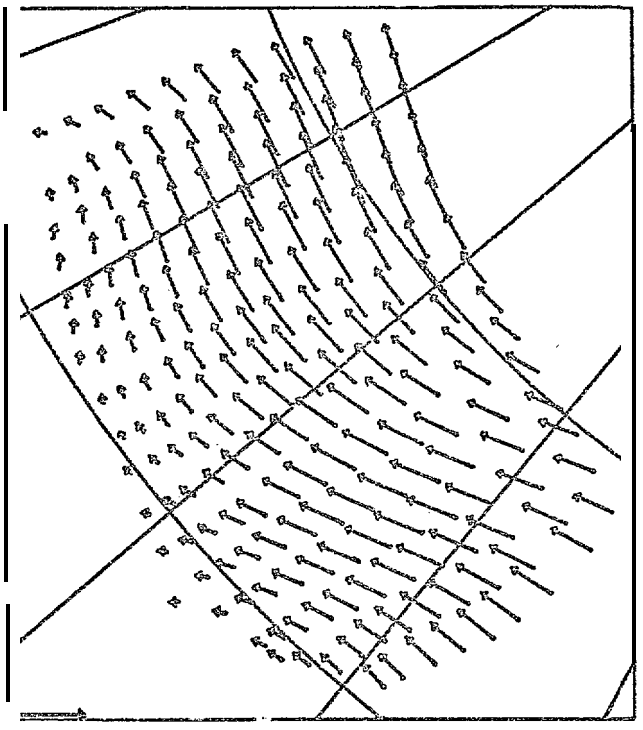

e) 31 January

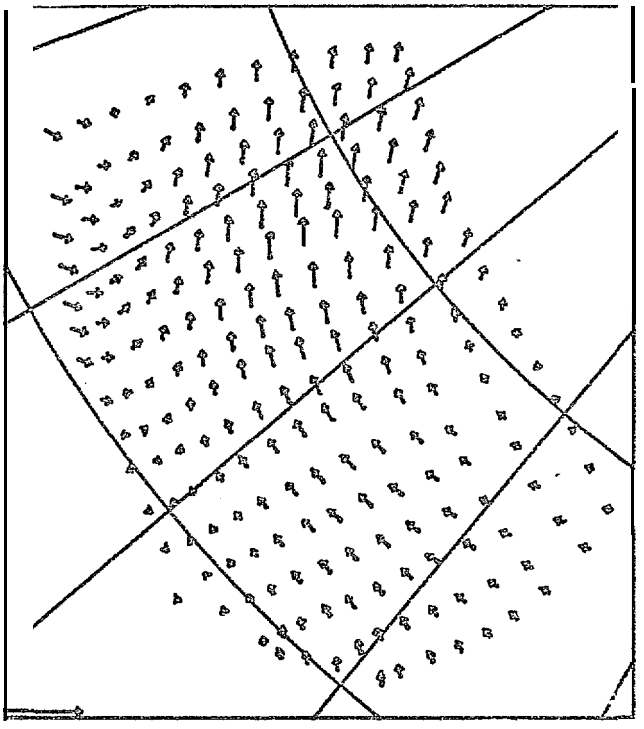

f) 1 February

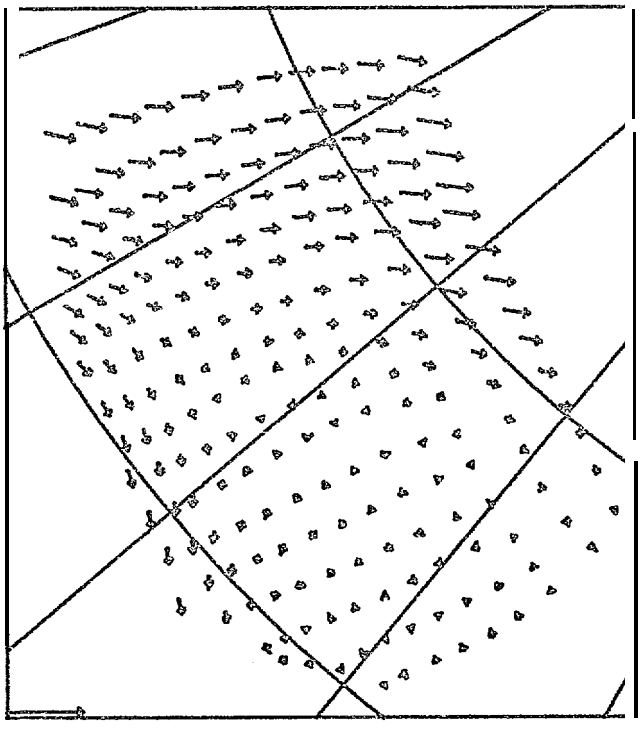

g) 2 February

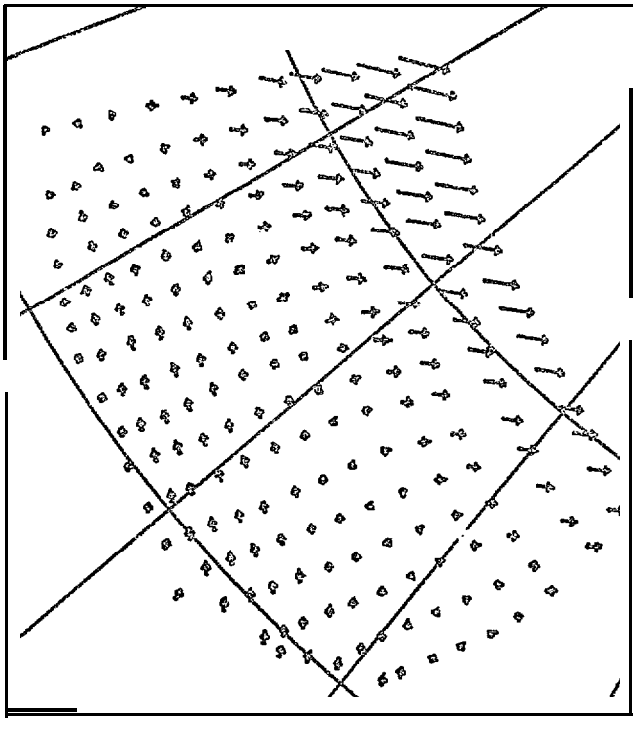

h) *3* February

Figure 20. (cont.) Daily Average of Air Stress Field. Scale vector is 4 dyn cm-1.

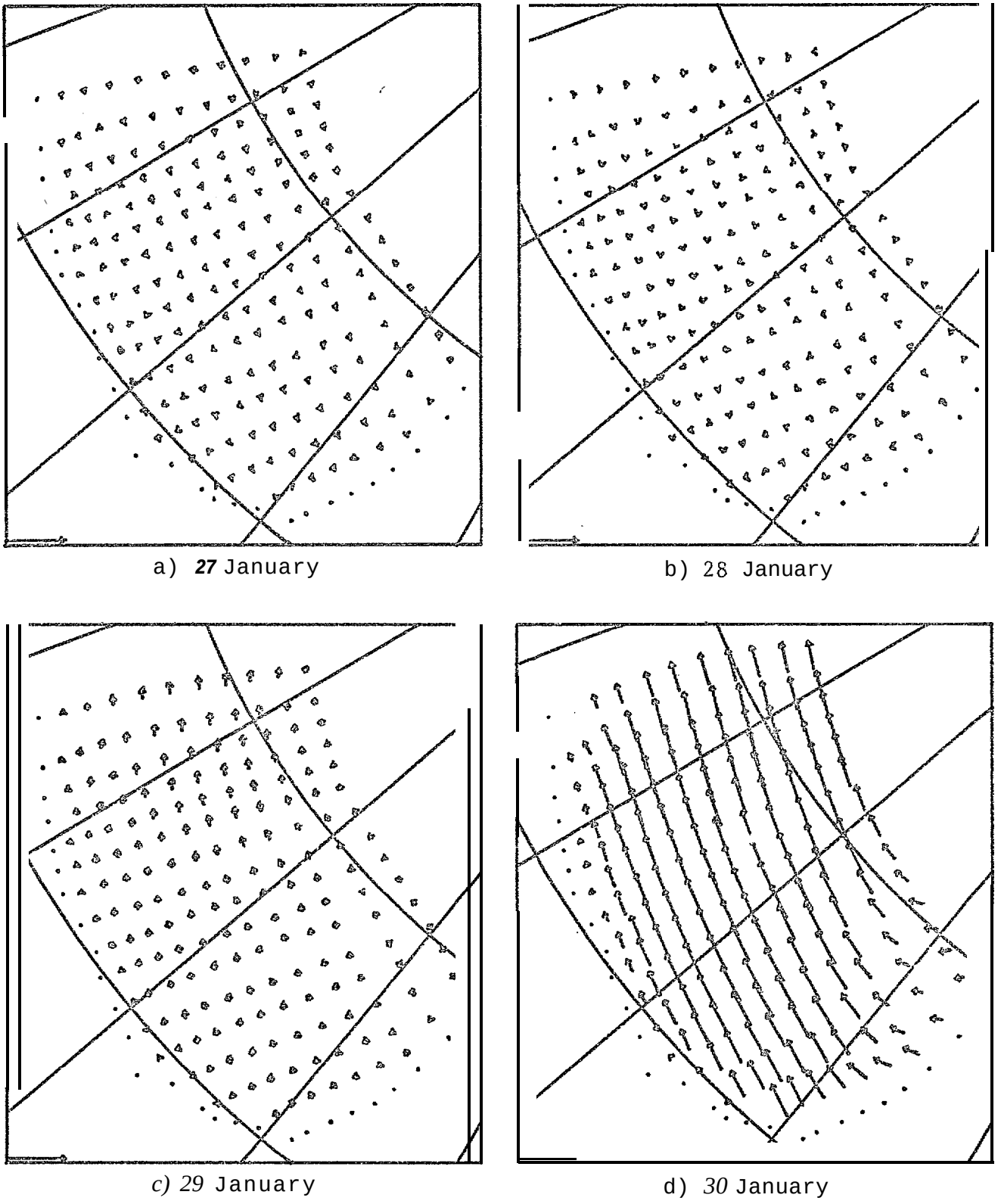

a) 27 January

b) 28 January

c) 29 January

d) 30 January

Figure 21. Modeled Ice Velocity Field with Yield Strength $p^* = 10^8$ dyn cm^{-1}. Scale vector is 25 cm sec^{-1}.

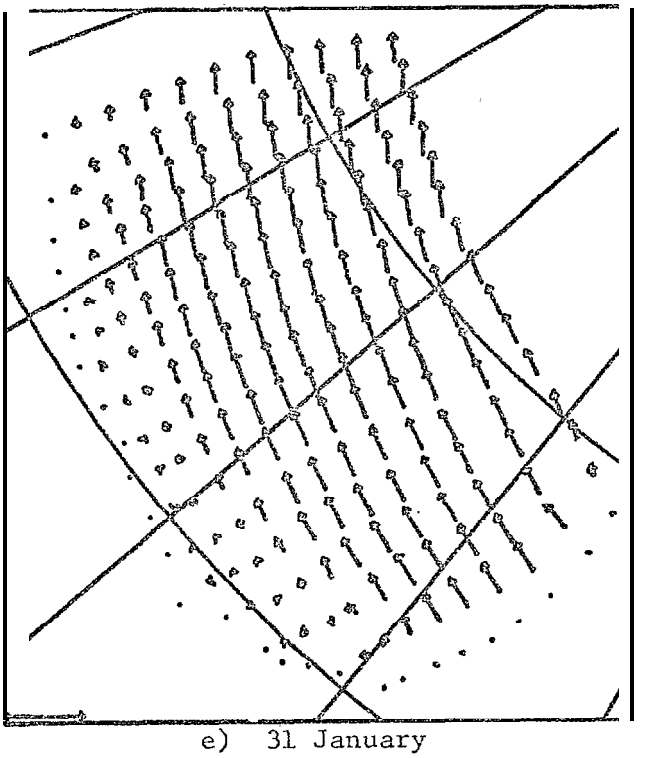

e) 31 January

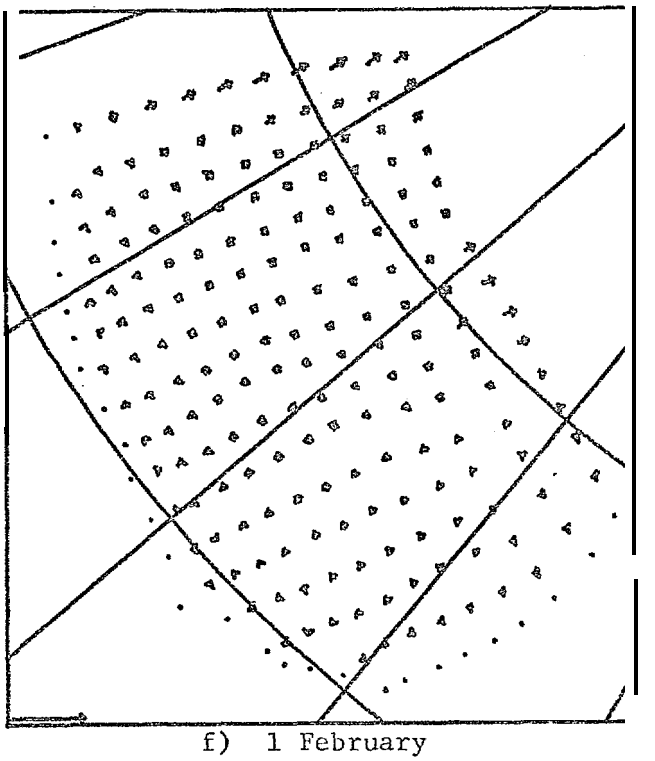

f) 1 February

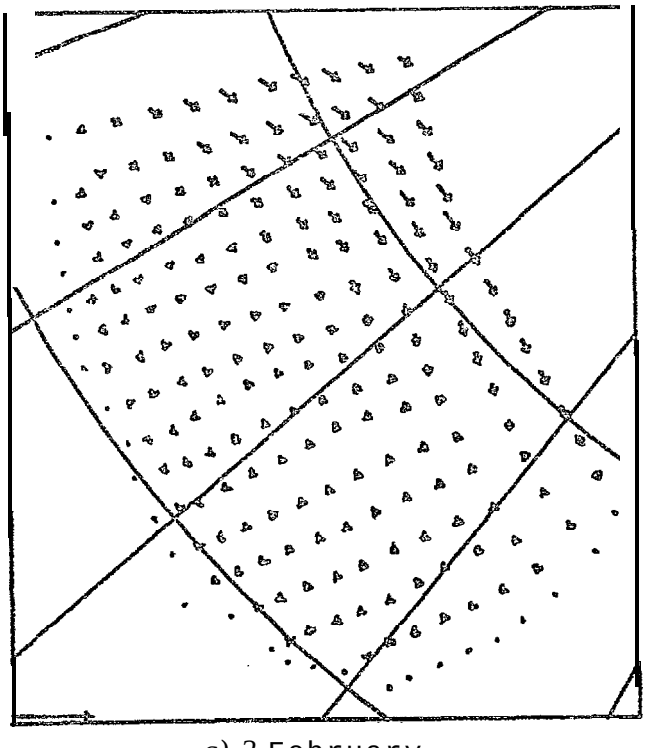

g) 2 February

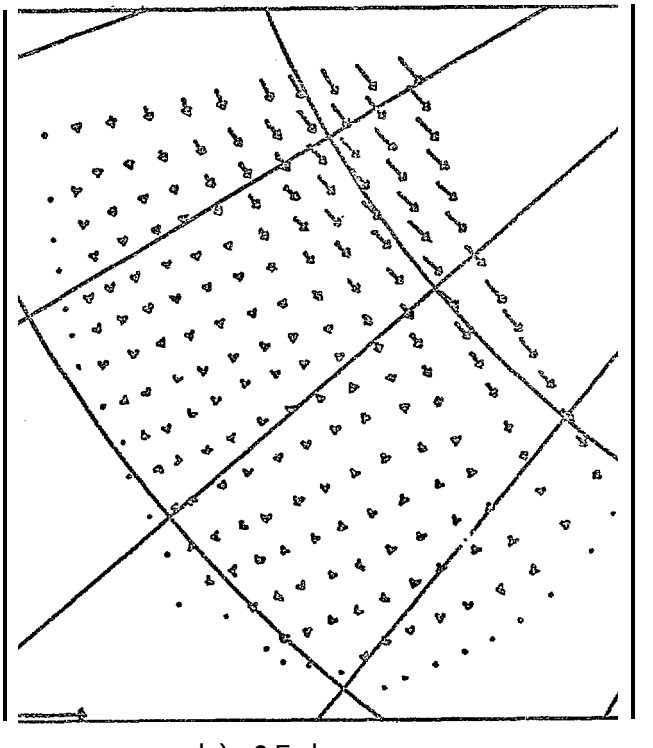

h) *3* February

Figure 21. (cent.) Modeled Ice Velocity Field with Yield Strength $p^* = 10^8$ dyn cm^{-1}. *Scale* vector is *25* cm *see-l.*

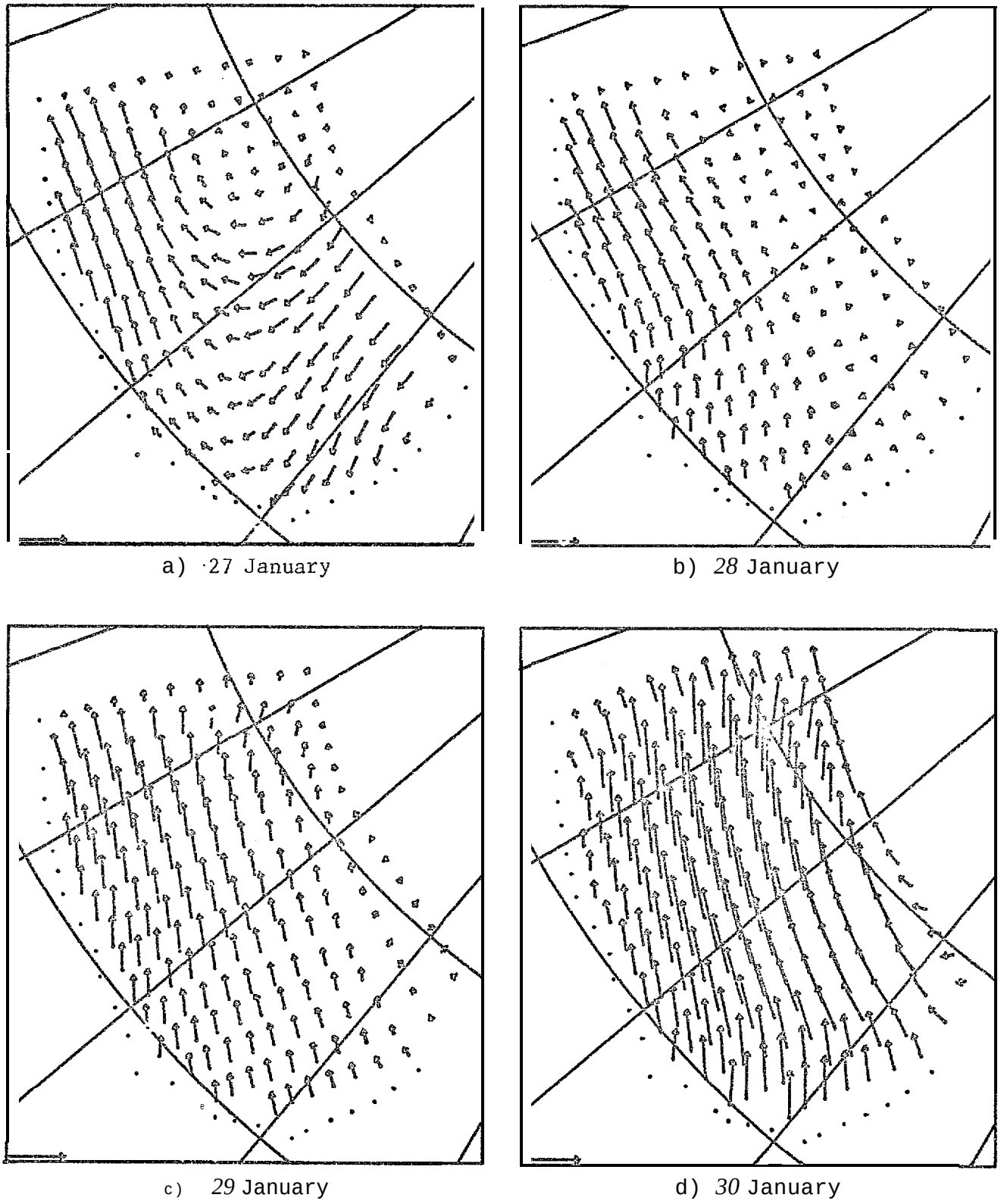

a) 27 January

b) 28 January

c) 29 January

d) 30 January

Figure 22. Modeled Ice Velocity Field with Yield Strength $p^* = 10^7$ dyn cm^{-1}. Scale vector is 25 cm see-l.

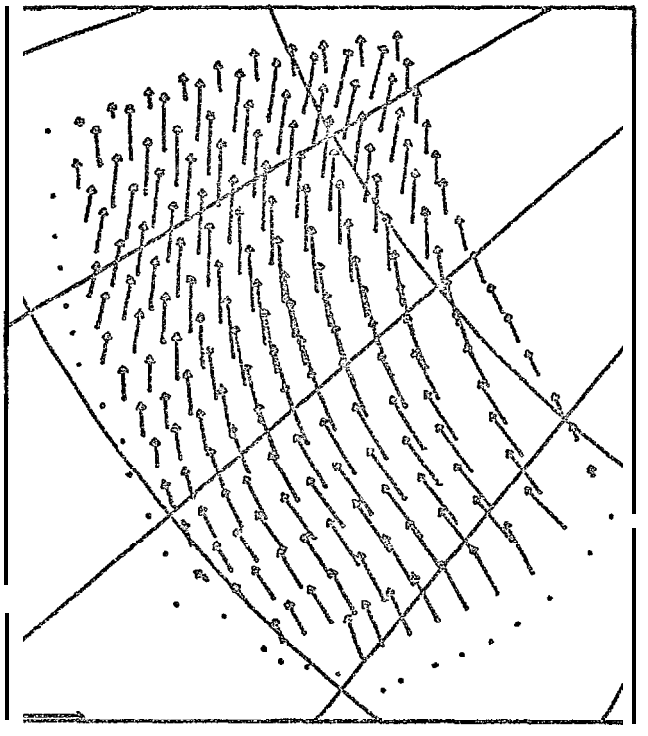

e) 31 January

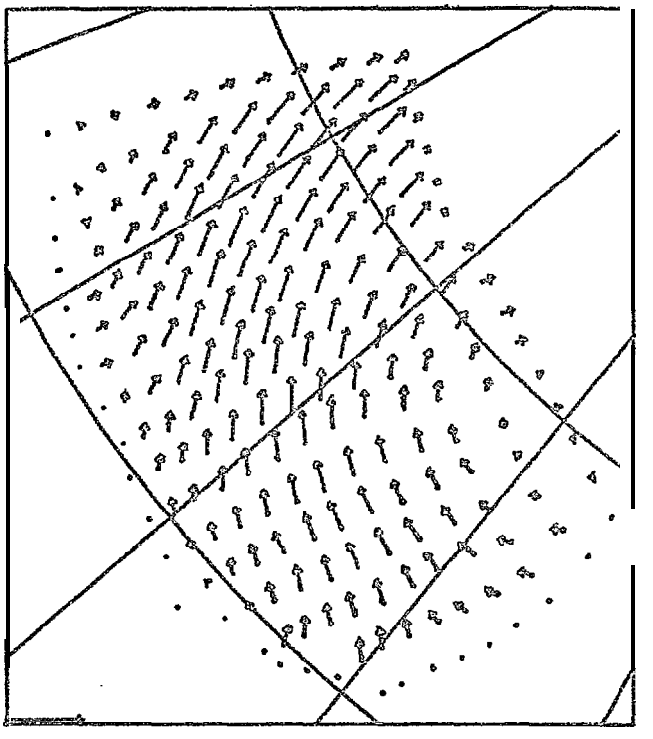

f) 1 February

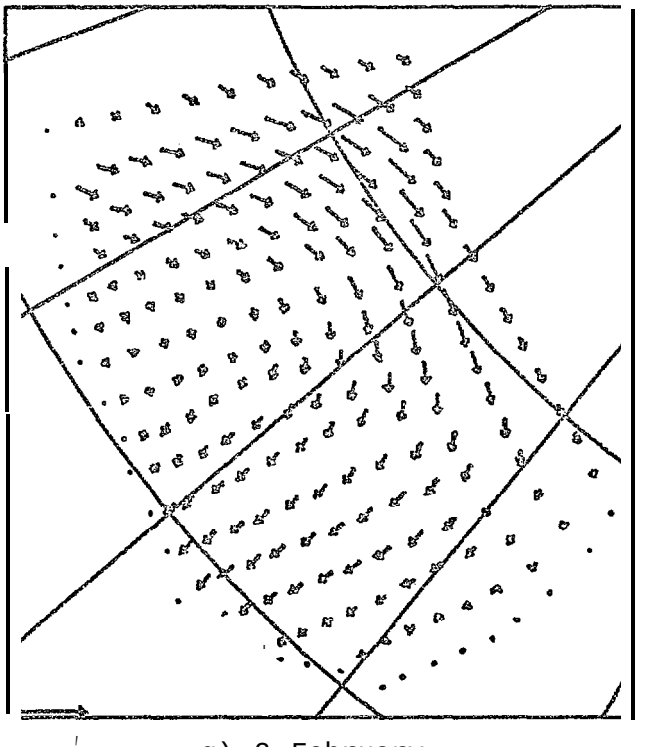

g) 2 February

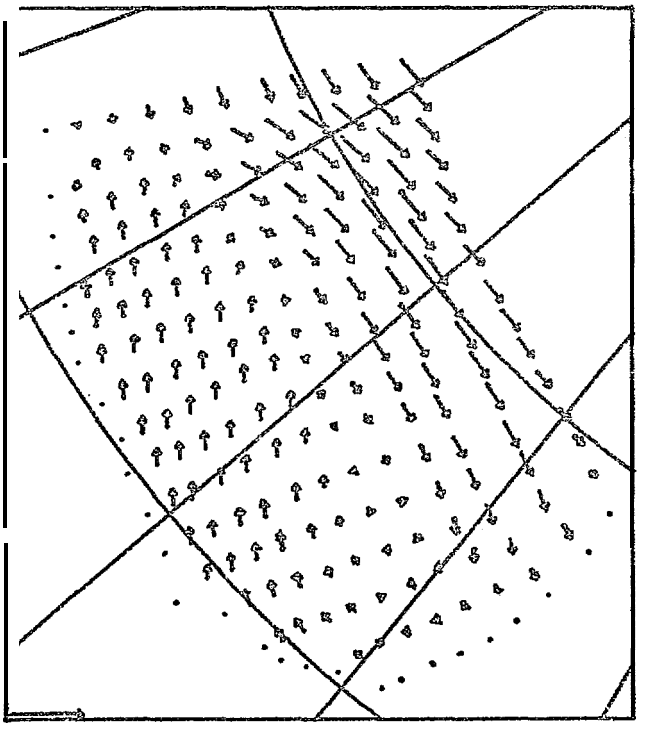

h) *3* February

Figure 22. (cent.) Modeled Ice Velocity Field with Yield Strength $p^* = 10^7$ dyn cm^{-1}. Scale vector is 25 cm see-l.

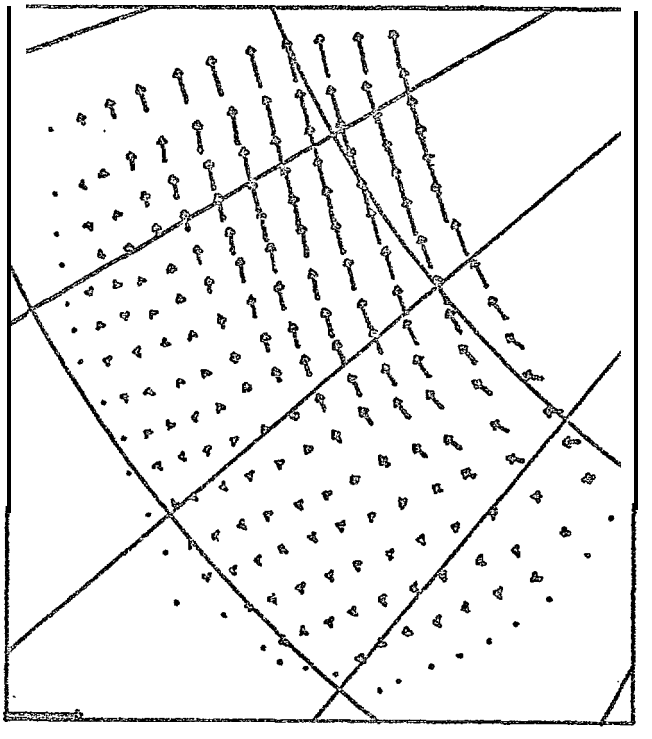

30 January

Figure 23. Modeled Ice Velocity Field with Yield Strength $p^* = 10^9$ dyn cm^{-1}. Scale vector is 25 cm see-l.

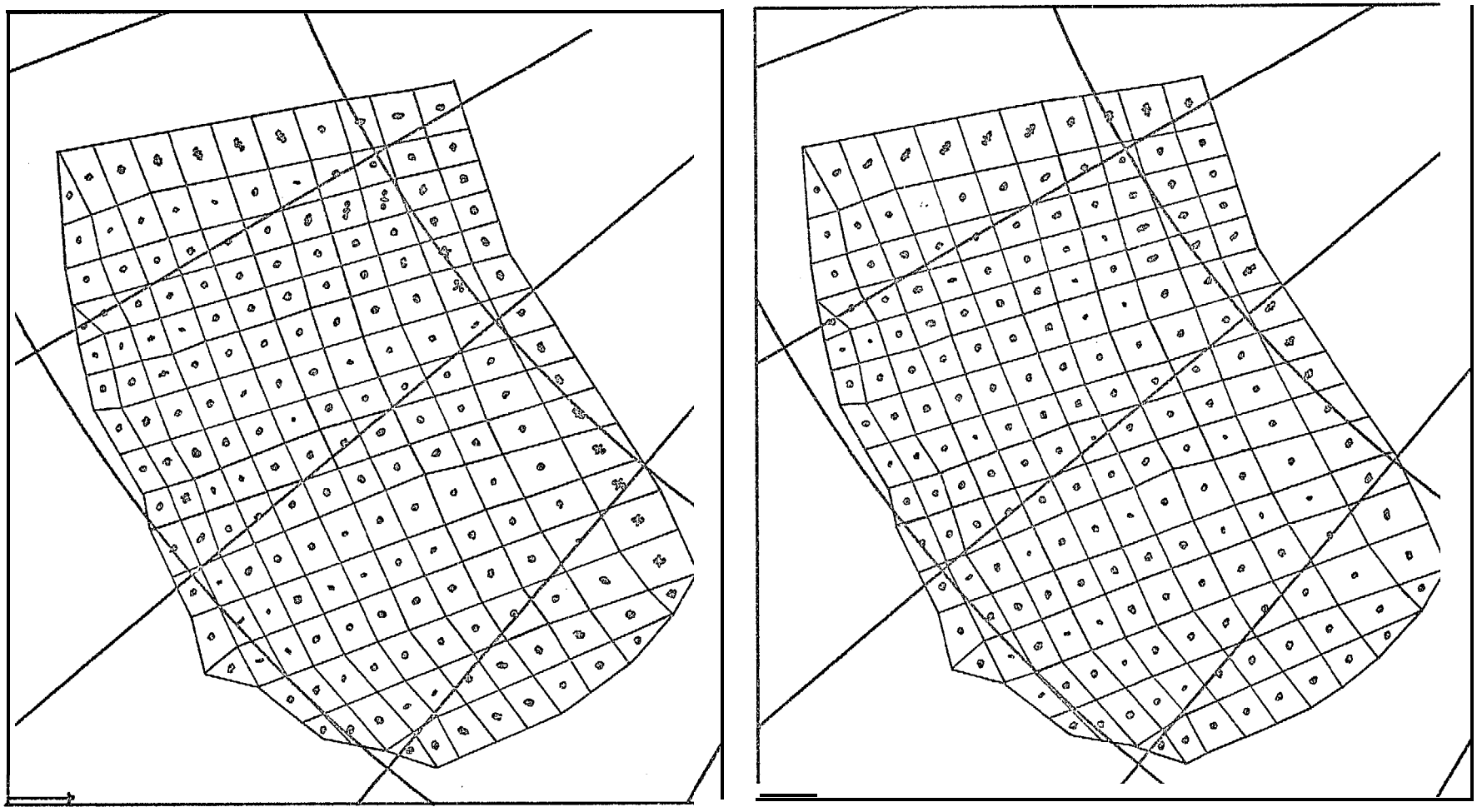

a) 27 January

b) 28 January

Figure 24. Stretching Tensor Field (Daily Strain) with Principal Values Proportional to Line Length in Directions Shown. Dashed lines indicate opening and solid lines closing. Scale vector is 8 x 10^{-1} sec^{-1} (approximately 8% per day).

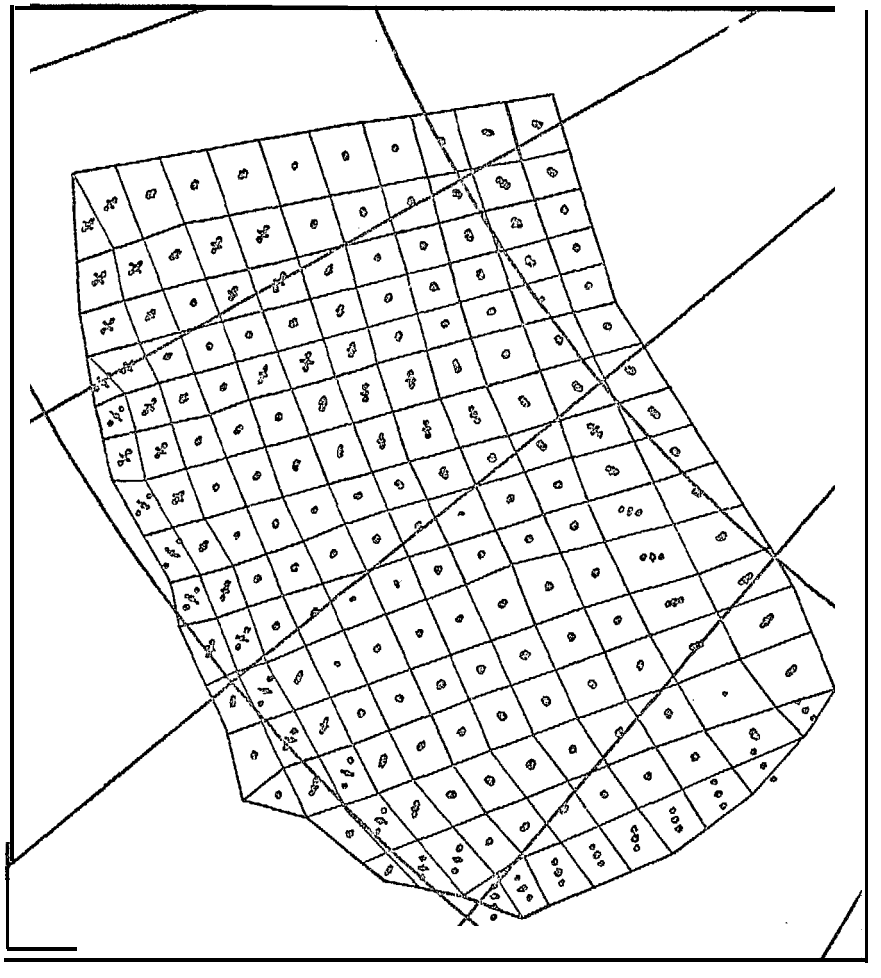

c) 29 January

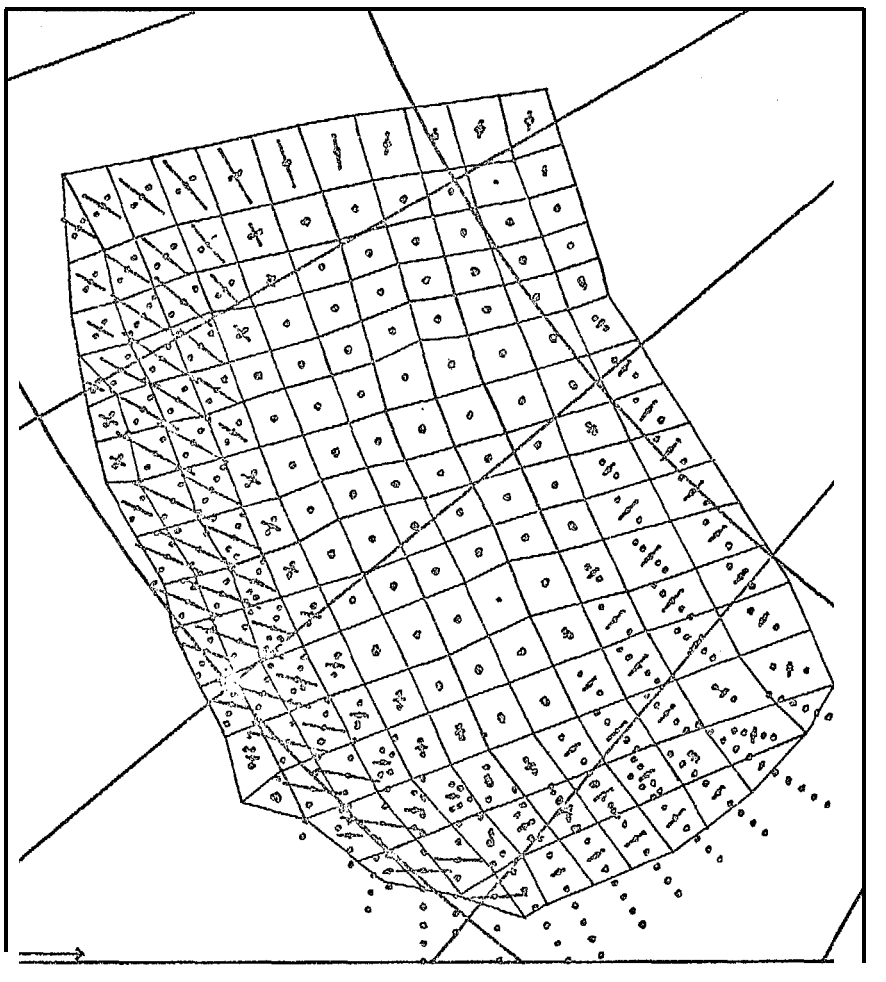

d) 30 January

Figure 24. (cent.) Stretching Tensor Field (Daily Strain) with Principal Values Proportional to Line Length in Directions Shown. Dashed lines indicate opening and solid lines closing. Scale-vector is 8×10^{-7} sec^{-1} (approximately 8% per day).

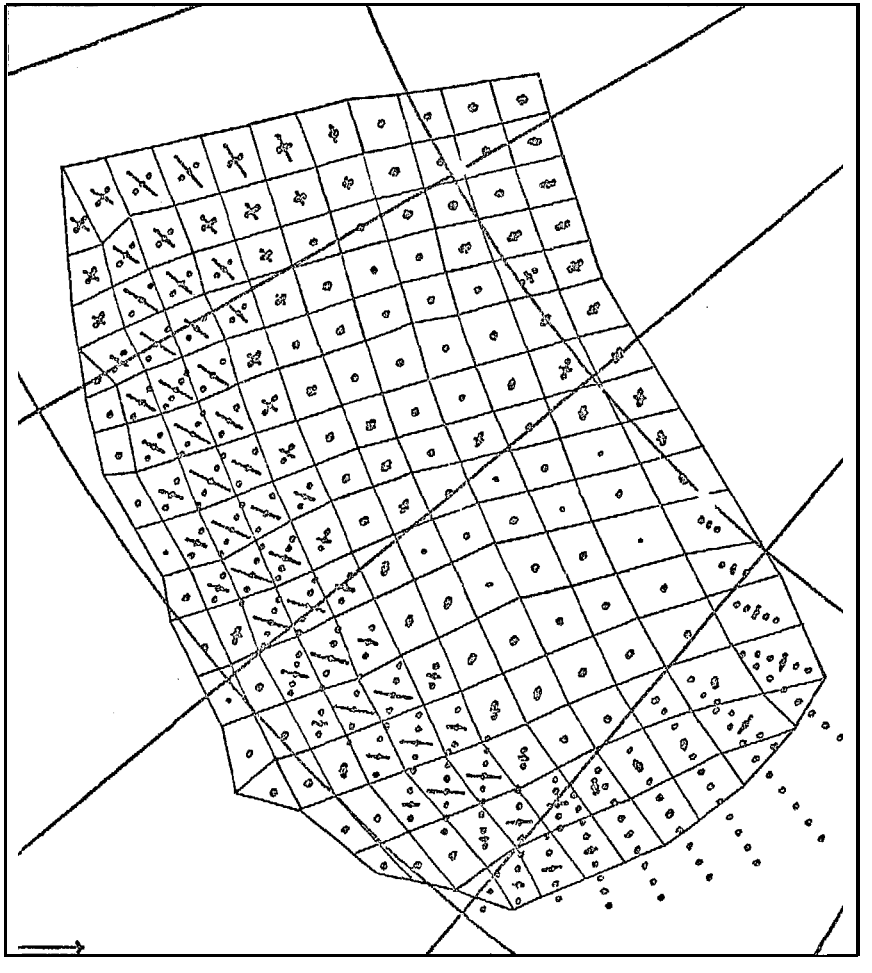

e) 31 January

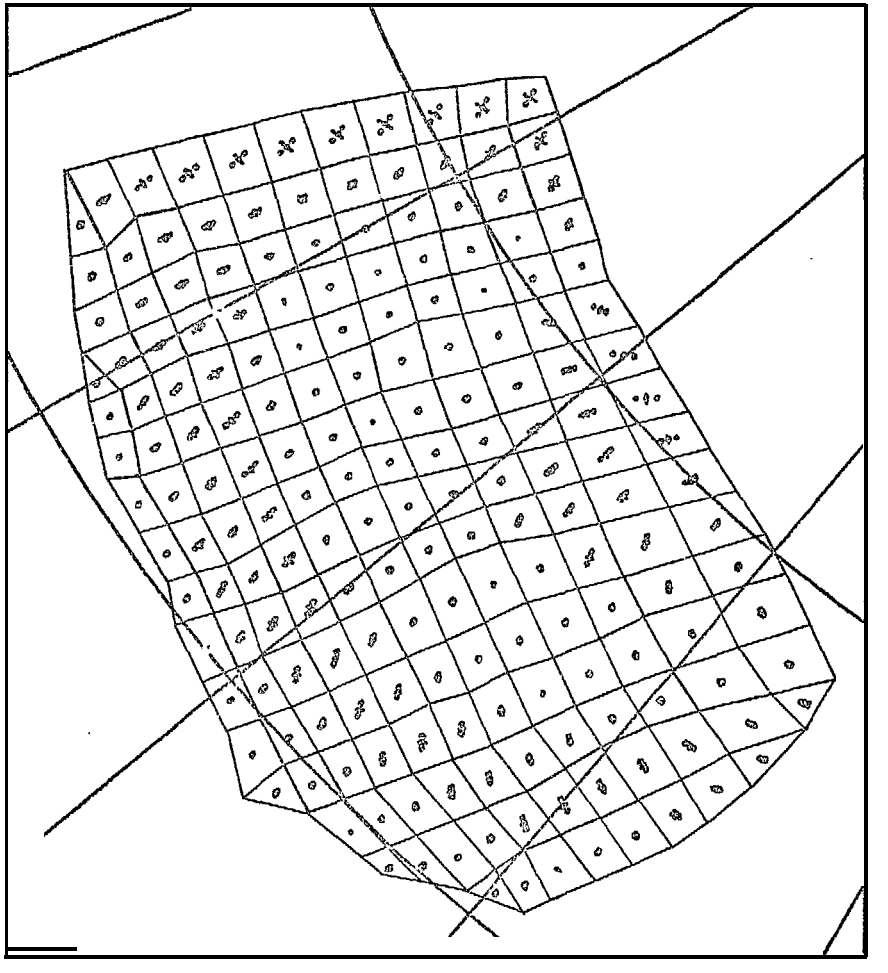

f) 1 February

Figure 24. (cent.) Stretching Tensor Field (Daily Strain) with Principal Values Proportional to Line Length in Directions Shown. Dashed lines indicate opening and solid lines closing. Scale vector is $8 \times 10^{-7} sec^{-1}$ (approximately 8% per day).

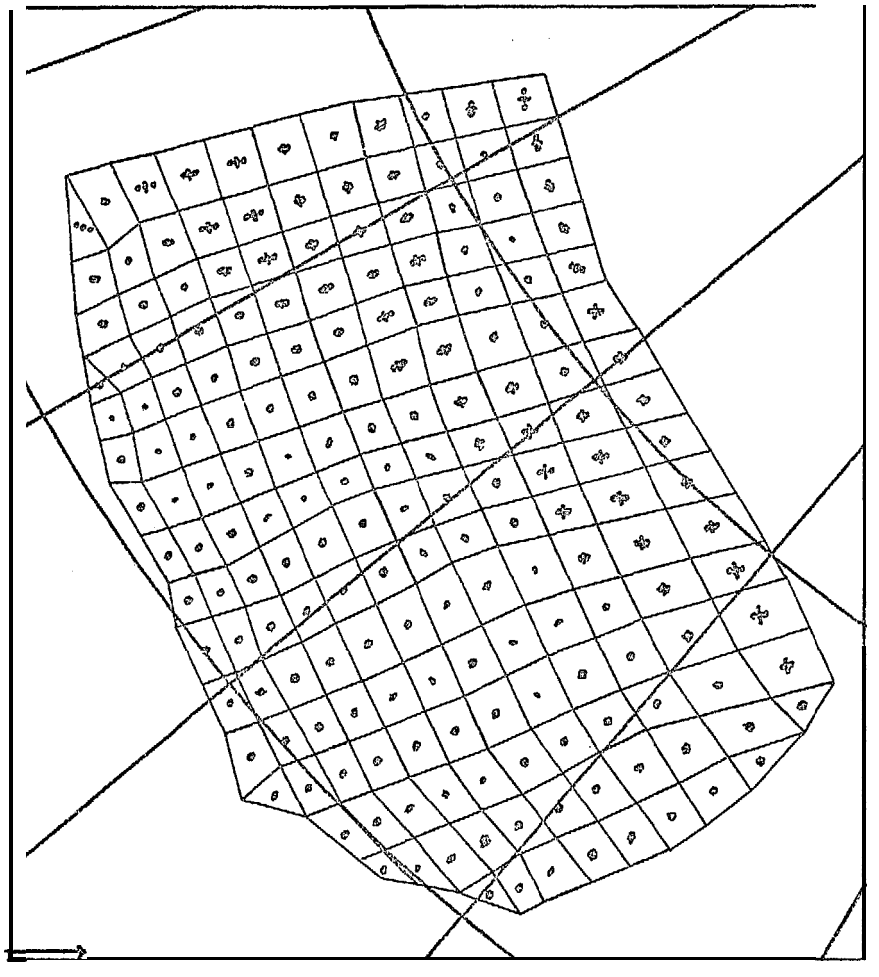

g) 2 February

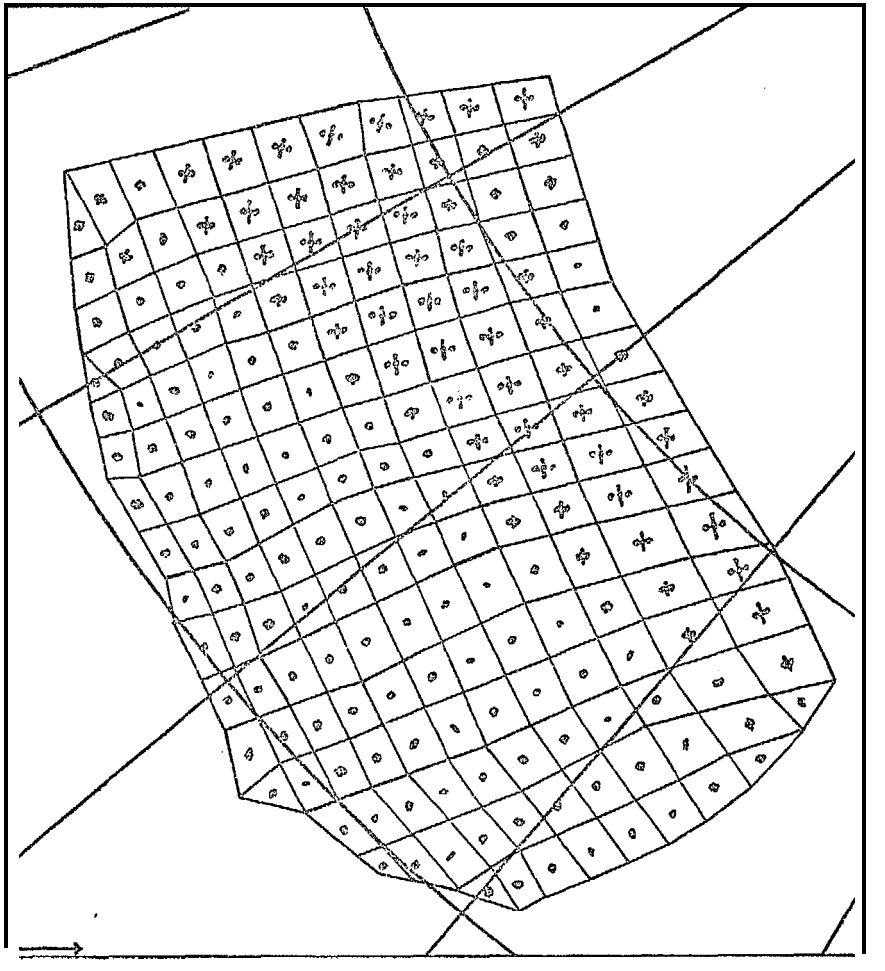

h) 3 February

Figure 24. (cent.) Stretching Tensor Field (Daily Strain) with Principal Values Proportional to Line Length in Directions Shown. Dashed lines indicate opening and solid lines closing. Scale vector is 8x10-7 see-1 (approximately 8% per day).

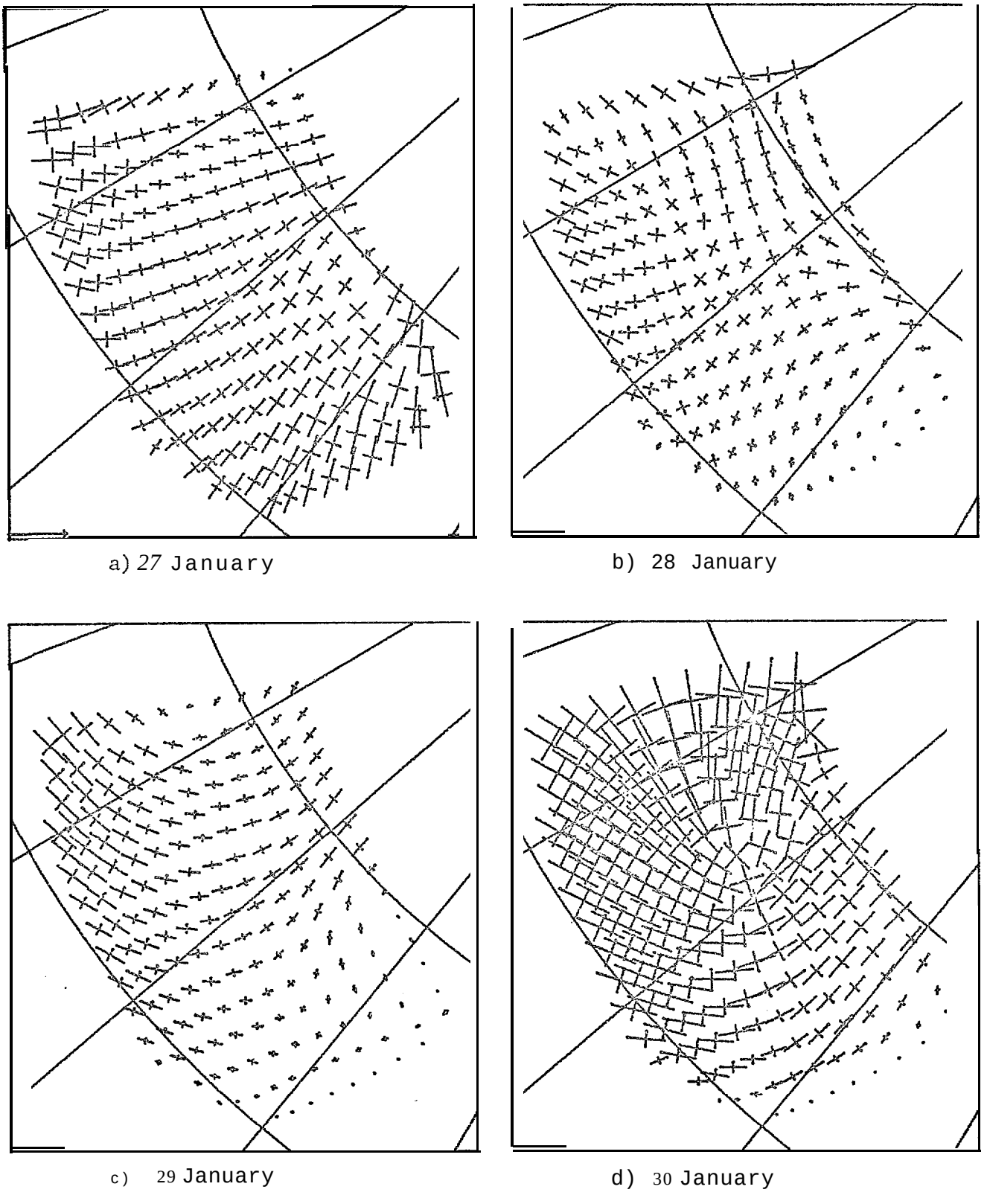

a) 27 January

b) 28 January

c) 29 January

d) 30 January

Figure 25. Stress Tensor Field with Principal Values (all compressive) Proportional to Line Lengths in Directions Shown. Scale vector is 10^8 dyn cm^{-1}.

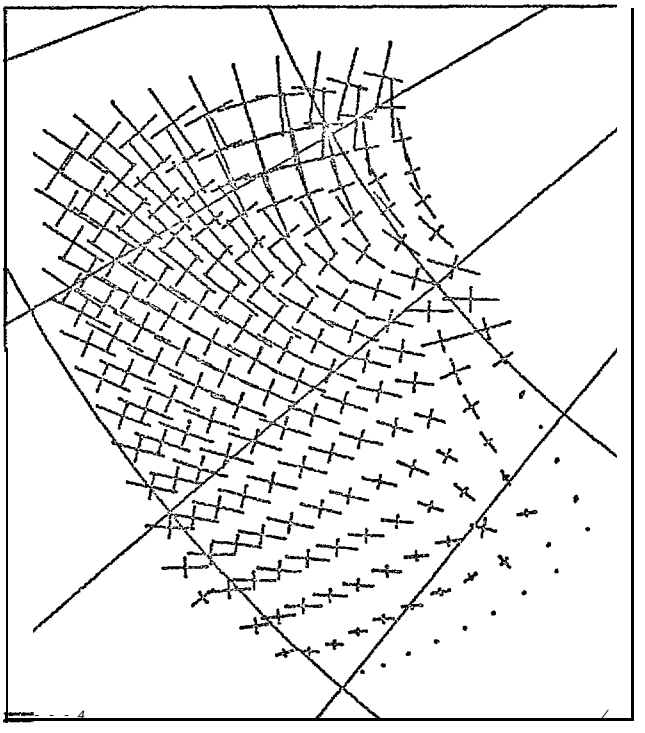

e) 31 January

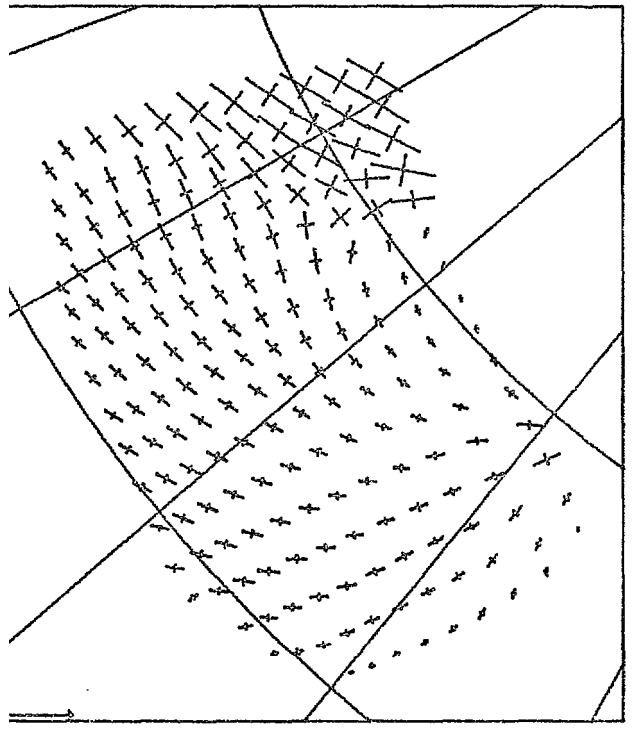

f) 1 February

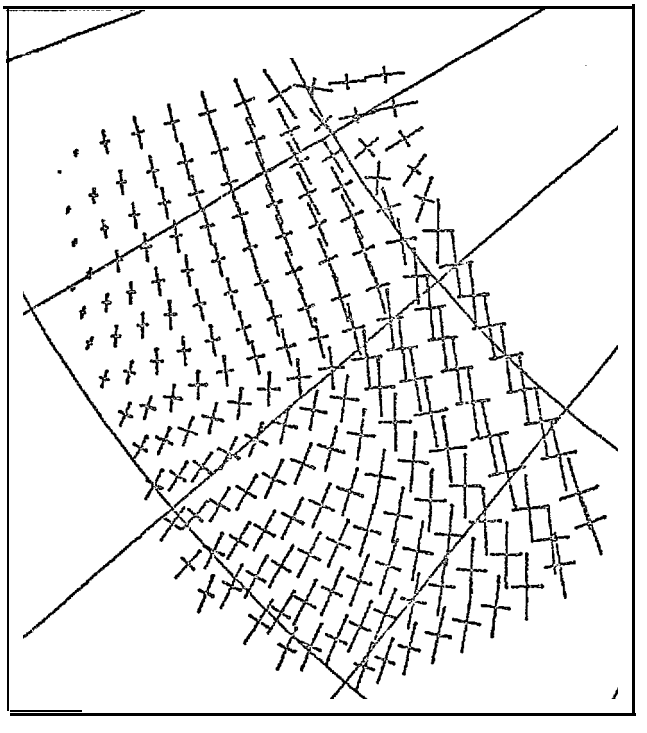

g) 2 February

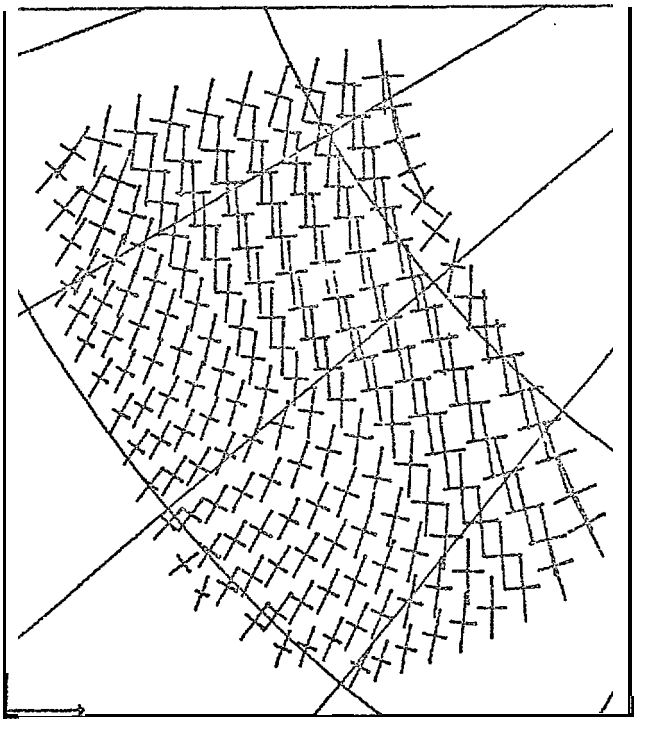

h) 3 February

Figure 25. (cent.) Stress Tensor Field with Principal Values (all compressive> Proportional to Line Lengths in Directions Shown. Scale vector is 10^8 dyn cm^{-1}.

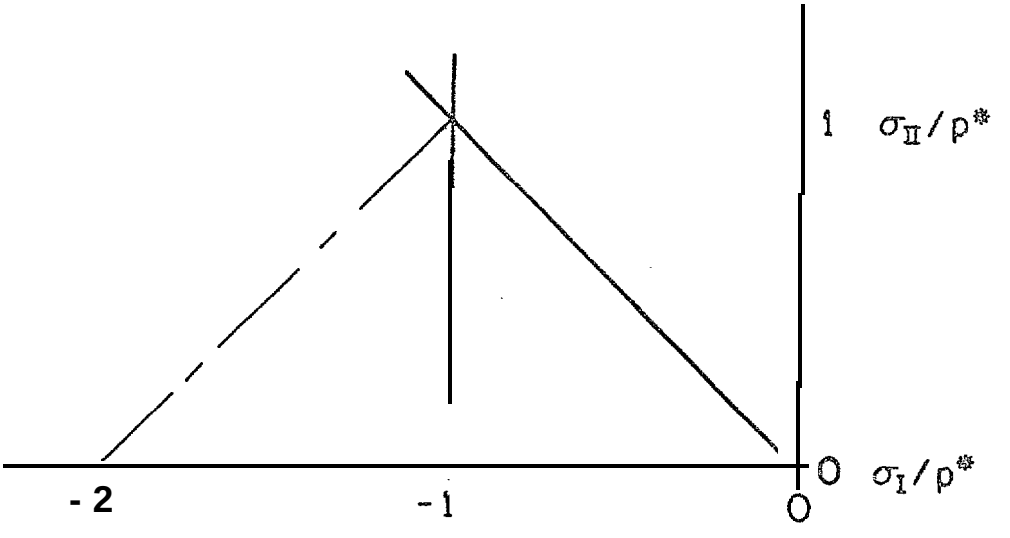

Figure 26. Triangle Yield Curve.

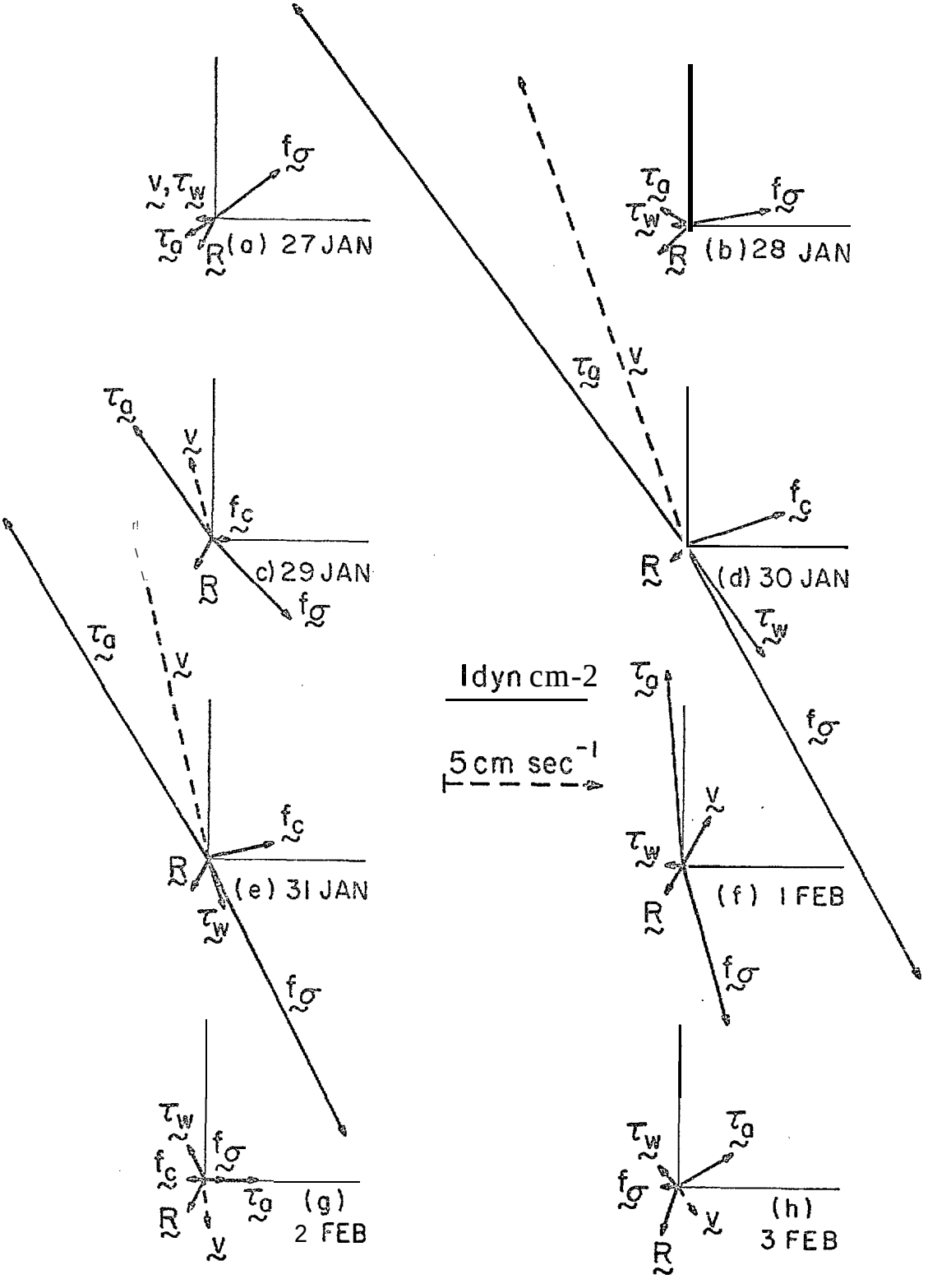

Figure 27. Force Balance at Node Nearest Caribou for Each Day. Scale vectors show magnitude of forces (per unit area) and velocity (dashed). Air stress τ_a, water stress τ_w. ice stress divergence f_σ, Coriolis force f_c and ice velocity $\vec{v}$ are each shown . If any vector is missing, then it is zero on that day. Cartesian axes are aligned with all other axes in this report.

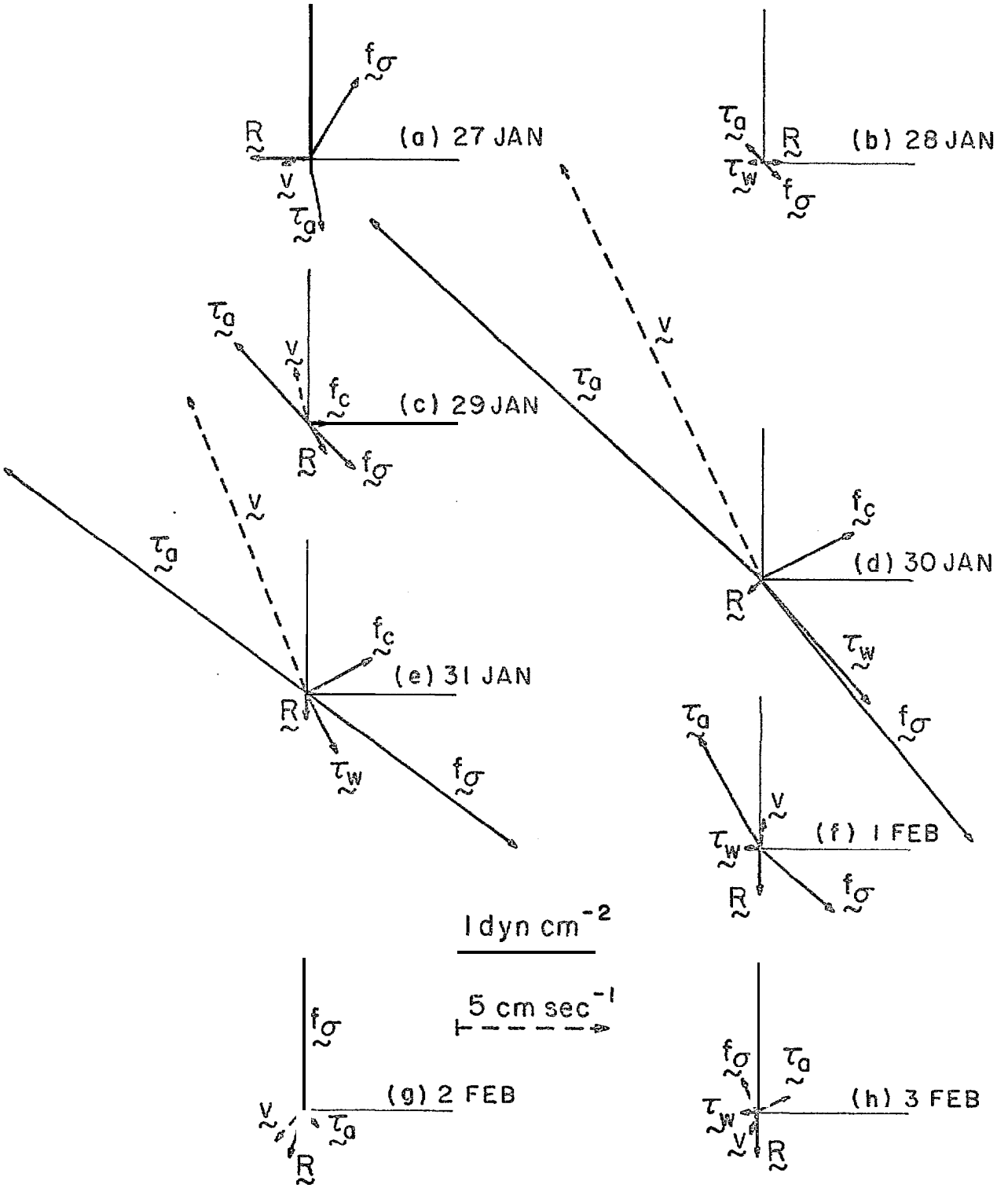

Figure 28. Force Balance at Node Nearest Blue Fox for Each Day. Scale vectors show magnitude of forces (per unit area) and velocity (dashed). Air stress $\underset{\sim}{\tau}_a$, water stress $\underset{\sim}{\tau}_w$, ice stress divergence $\underset{\sim}{f}_\sigma$, Coriolis force $\underset{\sim}{f}_c$ and ice velocity $\underset{\sim}{v}$ are each shown. If any vector is missing, then it is zero on that day. Cartesian axes are aligned with all other axes in this report.